

Chemical Vapor Deposition of Titanium Nitride based Hard Coatings



Dipl.-Ing. Josef Wagner

Leoben, January 2007

Being a thesis in partial fulfillment of the requirements for the degree of a

Doctor of montanistic sciences (Dr. mont.)

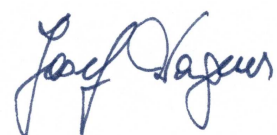
at the University of Leoben

This thesis was supported by the Technologie Impulse GmbH in the frame of the K-plus Competence Centre program at the Materials Center Leoben Forschung GmbH in cooperation with the University of Leoben, CERATIZIT Austria GmbH and CERATIZIT Luxembourg S.à.r.l.

Affidavit

I declare in lieu of oath that I did the PhD thesis by myself using only literature cited in this volume.

Leoben, January 2007

A handwritten signature in blue ink, appearing to read 'Josef Wagner', is located in the bottom right corner of the page.

Acknowledgments

I would like to thank o. Univ.-Prof. DI Dr. Helmut Clemens and em. Univ.-Prof. DI Dr. Dr. h.c. Franz Jeglitsch for giving me the opportunity to conduct this work at the Department of Physical Metallurgy and Materials Testing at the University of Leoben.

I am very indebted to ao. Univ.-Prof. DI Dr. Reinhold Ebner, Managing Director of the Materials Center Leoben (MCL) for giving me the opportunity to work at the MCL.

My sincerest appreciation and gratitude is due to my supervisor ao. Univ.-Prof. DI Dr. Christian Mitterer, leader of the Thin Film Group at the Department of Physical Metallurgy and Materials Testing in Leoben, for his encouragement and kindness, and for having faith and confidence in me. I am grateful for everything I have learned from him.

I am very indebted to the people from CERATIZIT Austria. Especially to DI Dr. Martin Kathrein for his support, for showing me the aspects of industry and for giving me ample scope in this project. It was a pleasure to work with you. I am also grateful to Karl Gigl for performing the depositions, for his effort, patience and assistance throughout all, sometimes uncommon tests. I also thank Wolfgang Wallgram and Josef Thurner for their support and the valuable discussions.

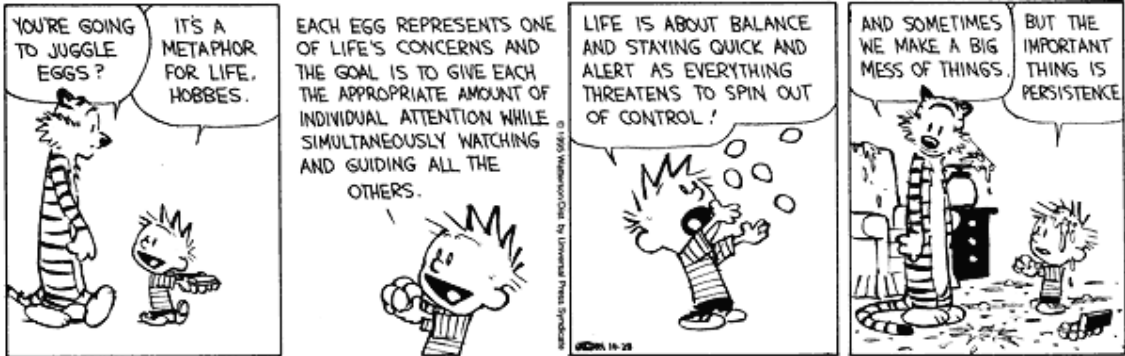
My gratitude goes to the staff of CERATIZIT Luxembourg. In particular, I am much obliged to MSc Marianne Penoy for the innumerable measurements she performed for me and to DI Claude Michotte for his effort and patience throughout the project. Thank you for taking care during my stays in Luxembourg.

I am very grateful to my diploma students DI David Hochauer and DI Viktoria Edlmayr for their assistance and patience during all unexpected and time-consuming difficulties. Furthermore, I would like to thank my student co-worker Jörg Radanitsch for his support.

I am thankful to Dipl.-Phys. Dr. Christina Scheu and DI FH Jörg Thomas for performing the TEM investigations, their kindness and the valuable discussions. Moreover, I would like to extend my thanks to Gerhard Hawranek for the excellent SEM work.

I would like to express my sincerest gratitude to my colleagues and friends at the Department of Physical Metallurgy and Materials Testing. Especially to my "old" friends who accompany me since a long time here in Leoben, particularly, Kerstin Kutschej, Martin Moser, Harald Chladil, Gert Gassner, Michael Bischof, Gerardo Fontalvo, Herbert Willmann, and Paul Mayrhofer. I am also grateful to all the friends I found within the last years, especially Rostia and Jitka Daniels, Martin Pfeiler, Claudia Walter, Marisa Figueiredo, Robert Franz, and Jörg Neidhardt. Their support and care helped me to overcome all setbacks and to change my mind in gloomy days. Thank you for the wonderful time!

My final and special thanks go to my beloved family. Without their everlasting support and faith throughout my entire life, it would have never been possible to do this thesis. I am deeply grateful to them!



Calvin and Hobbes by Bill Watterson

Contents

1 Introduction	1
2 Chemical Vapor Deposition.....	3
2.1 General	3
2.2 CVD Systems	4
2.3 Fundamentals of CVD	5
2.3.1 Gas Transport	6
2.3.2 Thermodynamics.....	7
2.3.3 Growth Kinetics	10
2.4 Coating Structure	13
2.4.1 Structure Evolution.....	14
2.4.2 Process – Microstructure – Properties	16
3 CVD of Hard Coatings.....	20
3.1 General	20
3.2 Design Aspects.....	21
3.2.1 Hardness.....	21
3.2.2 Chemical Stability.....	25
3.2.3 Adhesion	27
3.3 TiN.....	29
3.4 Ti–C–N	31
3.5 Ti–B–N	32
3.6 Ti–Al–N	33
4 Tribology of Coatings	36
4.1 General Aspects of Tribology.....	36
4.2 Friction	37
4.3 Wear.....	40

5 Experimental.....	43
5.1 Coating Deposition.....	43
5.2 Coating Characterization	44
5.2.1 General.....	44
5.2.2 Raman Spectroscopy.....	45
5.2.3 GIR-FTIR Spectroscopy.....	48
6 Summary and Conclusions	49
7 Symbols and Abbreviations	52
7.1 Symbols.....	52
7.2 Abbreviations.....	53
8 Literature.....	55
9 Publications.....	63
9.1 List of Included Publications.....	63
9.2 Supervised Diploma Theses.....	63
9.3 Contribution to the Included Publications.....	63

1 Introduction

The major shaping process in manufacturing of engineering components is cutting of metals and other materials. The employed cutting tools have a remarkable influence on the productivity and manufacturing costs of the components. The rate of material removal determines the machining times and the replacement of worn out tools causes the shut-down of machines. Today the components in use have to face high performance requirements and the application of coatings enables the design of components with properties located at their most need. The bulk material can be created with respect to high strength and toughness, while the coating is responsible for the protection against wear, thermal loads and corrosion. The deposition of hard coatings onto cemented carbide cutting tools has shown to improve the tool lifetime as well as the cutting performance since more than three decades. The commercial application of these coatings started with the process of thermal chemical vapor deposition (CVD). Within the years, various plasma assisted physical vapor deposition (PVD) techniques, such as sputtering or arc evaporation have been introduced [1-4].

Both CVD and PVD techniques have distinct advantages and limitations inherent from their process principles. Thermal CVD enables the deposition of coatings with excellent mechanical properties onto tools of complex geometry. Customary deposition temperatures in thermal CVD processes are between 850 and 1050°C which limits the application to thermally stable substrates; however, these temperatures are applicative to cemented carbide substrates. The high temperatures usually provide excellently adherent coatings with thicknesses up to 20 µm. Moreover, CVD is not limited to conductive coating materials and allows the deposition of non-conductive materials, likes oxides in high quality. PVD processes allow the deposition of practically any coating material without limitations in chemical composition. The coatings usually exhibit a very dense microstructure, but high stresses limit the applicable coating thickness below 10 µm. PVD is a line-of-sight technique and requires complex arrangements such as three-fold planetary substrate rotation. Furthermore, the production of wear resistant oxides is problematic and still the domain of thermal CVD [5,6].

Nowadays, hard coatings are complex composites consisting of diverse materials to fulfill different, often contradicting requirements, such as an excellent adhesion to the substrate but low interaction with the metallic workpiece material. The development of hard coatings started initially with the introduction of single-phase coatings of TiC and TiN. Later, the assortment has been extended by the development of oxidic materials, such as Al₂O₃ [7]. Since the middle of the 1980's, the deposition of metastable coating structures has gained considerable interest [8]. Well-established in cutting tool industry

are metastable coatings in the Ti–Al–N system. The substitution of Ti atoms of the face-centered cubic (*fcc*) TiN lattice by Al results in metastable coatings that are usually referred to as *fcc*-Ti_{1-x}Al_xN ($0 \leq x \leq 1$) coatings. These coatings exhibit high oxidation resistance and hot-hardness. The production of metastable coatings is a conventional process in PVD, but only recently the formation of metastable *fcc*-Ti_{1-x}Al_xN coatings by thermal CVD has been reported [9].

This work focuses on the correlation between process conditions, microstructure and properties of thermal CVD hard coatings on the basis of TiN. Starting with pure TiN, the mechanical and tribological behavior was modified by the incorporation of three different alloying elements. The elements have been selected according to the formation of either single-, dual-, or metastable-phase coatings. First, carbon is completely miscible in the TiN lattice and enables single-phase TiC_xN_{1-x} ($0 \leq x \leq 1$) coatings with gradually adjustable properties ranging from pure TiN to TiC. The second element, boron, is well-known for its grain-refinement effect in metallurgical processes and in hard coatings. Moreover, the solubility of boron in TiN is small and TiN/TiB₂ dual-phase coatings form. The development of metastable *fcc*-Ti_{1-x}Al_xN coatings has been examined by the incorporation of aluminum into TiN.

The first chapters in this thesis outline the fundamental processes in thermal CVD, several design aspects on CVD hard coatings, the tribology of films as well as experimental aspects on the deposition process and coating characterization, particularly with regard to the investigated films. Subsequent to a short summary, the main experimental research is given in four scientific publications, where the obtained results are comprehensively discussed.

2 Chemical Vapor Deposition

2.1 General

Chemical Vapor Deposition (CVD) is defined as a process, which involves the dissociation and/or chemical reactions of gaseous reactants in an activated (heat, light, plasma) environment that results in the formation of a stable solid product [10].

The CVD process is a mature technique and dates back to the end of the 19th century. Over the years, many different CVD variants have been developed and optimized for specific applications. As a consequence, CVD techniques have been classified according to particular process characteristics, for example by the [10,11]:

- *type of reaction activation*: thermally activated CVD (TACVD) also called thermal CVD or conventional CVD, plasma-enhanced CVD (PECVD), photo-assisted CVD (PACVD)
- *applied precursor*: metal-organic CVD (MOCVD) uses compounds containing metal atoms and organic radicals
- *temperature range*: high-temperature CVD (HTCVD) between 850 and 1200°C, medium-temperature CVD (MTCVD) between 700 to 850°C, and low temperature (LTCVD) below 700°C
- *deposition pressure*: atmospheric pressure CVD (APCVD) for 10⁵ Pa, low pressure CVD (LPCVD) between 10 and 1000 Pa, or ultrahigh vacuum CVD (UHVCVD) for pressures below 0.1 Pa

This work focuses on the process of thermal CVD, especially on the deposition of hard wear resistant coatings for the application on cutting tools. Thermal CVD is a powerful technique and offers many advantages, e.g. CVD is not a line-of-sight technique and allows a uniform coating deposition on geometrically complex parts. The modification of process parameters enables the control of the morphology of the deposits ranging from epitaxial to polycrystalline or even amorphous structures. However, thermal CVD has also some drawbacks. Most of the precursors used in CVD are highly reactive, flammable, or toxic. The deposition temperatures can easily reach 1000°C, which limits the application to heat resistant substrates, such as ceramics (e.g. Al₂O₃) or cemented carbides. It can be difficult to obtain multicomponent coatings of defined stoichiometry from multi-source precursors. The utilization of different precursors can cause undesirable premature reactions, such as the formation of solid complexes, or differences in reactivity can result in depletion of one component [10,12,13].

2.2 CVD Systems

CVD systems exist in manifold variations and are individually tailored for specific coating materials or substrate geometries, for instance. Regardless of the process type, all CVD systems consist of three principle elements [10]:

- chemical vapor precursor supply system
- CVD reactor
- exhaust gas treatment

A schematic of a production unit for the deposition of coatings on cutting tools is shown in Fig. 1. The function of the precursor supply system is the generation and delivery of gaseous precursors into the reactor. Gaseous precursors, e.g. Ar, H₂ or N₂ can usually be metered and fed directly from gas bottles, while liquid and solid reactants require special equipments. In most cases, liquid precursors are evaporated in a bubbler system, where an inert carrier gas such as Ar or H₂ passes through the precursor (cf. Fig. 1). The evaporated reactant saturates the gas phase and is delivered into the reactor. The precursor concentration can be controlled by the temperature of the liquid precursor, the carrier gas flow rate, and the total pressure. The temperature regulation of bubblers can be sophisticated. Since the evaporation heat is removed from the system, the precursor temperature of the liquid decreases and the precursor partial pressure changes. This problem can be avoided by the application of flash evaporation, where the liquid is directly evaporated in a gas stream using pumps. Conventional liquid precursors for hard coating deposition are TiCl₄ and CH₃CN (acetonitrile) [14-16].

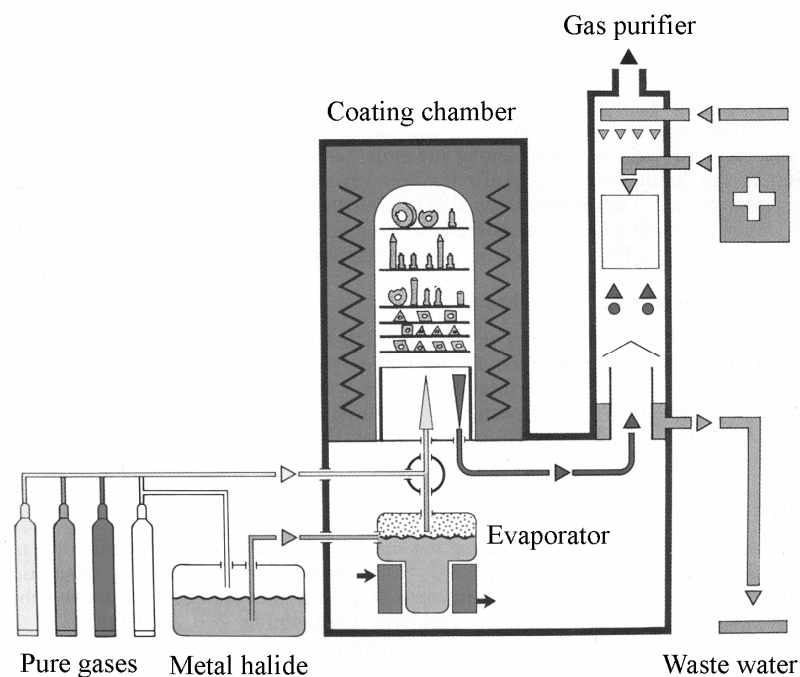


Fig. 1: Schematic of a CVD production unit [3].

The evaporation or sublimation of solids can be problematic since high temperatures are usually required. The Al containing precursor AlCl_3 is generated in-situ from the reaction between Al chips and HCl at temperatures above the sublimation temperature of 183°C . The vapor is conveyed with a carrier gas to the reactor. Heated lines are necessary to prevent premature condensation [14].

The main task of the CVD reactor is to isolate the reaction gases from the environment and to heat the substrates up to the deposition temperature. Reactors can be divided into hot- and cold-wall systems. In hot-wall systems the entire reactor is heated, but only the substrate in cold-wall units. CVD systems in cutting tool industry are principally hot-wall reactors [16,17], thus, only this type will be considered here. Since the entire interior is coated including the reactor wall, precursor depletion effects occur in hot-wall systems.

The exhaust gas treatment is subsequent to the deposition reactor, where precursor residues and by-products are neutralized in gas scrubbers. Water and sodium hydroxide is often used to decompose and neutralize metal chlorides and released HCl.

2.3 Fundamentals of CVD

Thermal CVD is a complex and multi-disciplinary process. Besides an understanding of the thermodynamics and kinetics of chemical reactions, CVD handles with the flow of gases, i.e. the fluid dynamics of gases has to be considered as well. The main steps in CVD are shown schematically in Fig. 2 for a horizontal reactor. The influence of the gas flow is indicated by the boundary layer – the region, where the gas flow velocity changes from zero at the surface to the bulk gas value. Within this boundary layer and in close vicinity to it, the key steps of the deposition process occur [10,18]:

- (1) transport of gaseous reactants into the reaction chamber and formation of intermediate species
- (2) *heterogeneous reaction* at the surface at temperatures below the dissociation temperature of the intermediate species:
 - (2a) transport of the gaseous reactants across the boundary layer and adsorption at the surface of the substrate
 - (2b) chemical reactions between adsorbed reactants and/or between species in the vapor phase
 - (2c) diffusion of the deposits along the surface, formation of nucleation centers, and film growth
 - (2d) desorption of by-products from the surface and diffusion across the boundary layer to the bulk gas
- (3) *homogeneous gas phase reaction* of intermediate species in the gas phase at high temperatures, and powder formation

(4) removal of by-products and unreacted precursors away from the deposition chamber

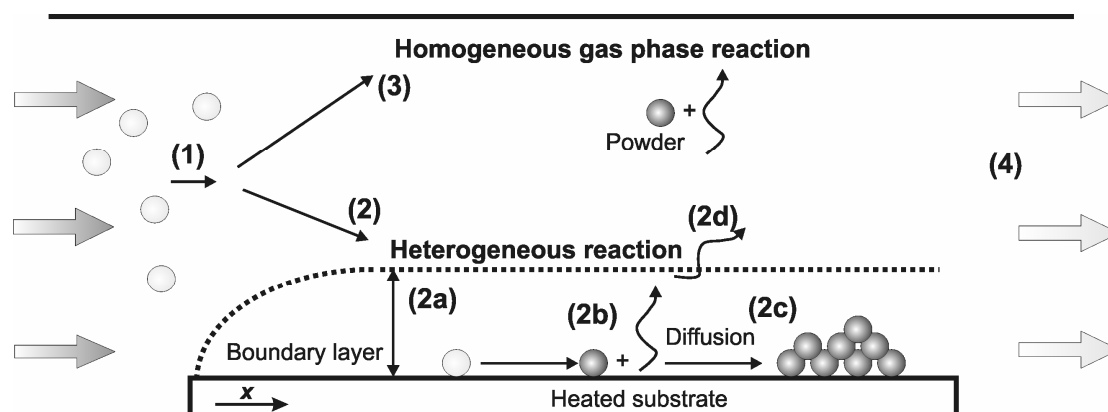


Fig. 2: Schematic illustration of the key steps in a CVD process (according to [10,18]).

Each of these steps influences the deposition of coatings and consequently the coating properties, e.g. the growth rate uniformity, stoichiometry, structure, or density. Undesirable for the deposition of hard coatings is the occurrence of homogeneous gas phase reactions that produces powder and results in porous coatings [10].

The fundamentals governing the CVD processes include the *gas transport*, which determines a homogeneous transport of reactants to all surfaces in the deposition chamber. *Thermodynamics* considers the driving forces of chemical reactions, whereas the *growth kinetics* defines reaction rates and rate controlling mechanisms [19,20]. The following sections will focus on these basic topics. Occasionally, the mechanisms are illustrated by means of TiN deposition, since it is one of the best studied coatings in CVD and [21], moreover, the basis system in this work (cf. Publications I-IV).

2.3.1 Gas Transport

The nature of gas transport phenomena defines the availability and distribution of precursors within the CVD reactor. Consequently, the reactant transport defines the coating thickness uniformity and the deposition efficiency, but also the structure and properties of coatings [18,20].

Forced convections arise in CVD reactors from the pressure difference between gas inlet and outlet. Variations in gas density, e.g. from temperature inhomogeneities, may additionally cause free convection. The resultant gas flow patterns can be very complicated, especially in reactors of complex geometry. Free and forced convection are bulk flow processes, where parts of the gas move in an overall motion. Usually, CVD processes operate at low flow velocities to establish a laminar flow. High velocities would cause the formation of turbulences and inhibit the formation of uniform films. During laminar viscous flow, a boundary layers form at the substrate surface, where the

flow velocity, the gas concentration and the temperature are different to those in the main gas stream. Hence, gradients in the velocity-, concentration-, and temperature-profile exist in the vicinity of the substrate. The different profiles have a crucial influence on the deposited coatings since the chemical reactions occur within this region. The thickness δ of the velocity boundary layer at a position x (cf. Fig. 2) on the substrate is given by [18]:

$$\delta \propto \sqrt{\frac{\eta x}{\rho v}} \quad (2.1)$$

with the gas viscosity η , the gas density ρ , and the flow velocity v . The boundary layer increases with lowered flow velocities and with the distance. From the temperature and pressure dependency of η and ρ it can be deduced that the boundary layer thickness increases with rising temperature and decreasing total pressures, respectively [18].

Different from the bulk flow are diffusion processes, which involve the statistical motion of particles. The diffusion processes play an important role in the mass transport through the stagnant boundary layer. The flux J through the boundary layer is expressed by [20]:

$$J = -D \frac{(p - p_0)}{\delta RT} \quad (2.2)$$

where D is the diffusivity, p the vapor pressure in the bulk gas, p_0 the vapor pressure at the surface, R the universal gas constant, and T the absolute temperature. The dependency of the diffusivity of gases on pressure and temperature can be estimated from the kinetic theory of gases [20]:

$$D \propto \frac{T^{3/2}}{\rho} \quad (2.3)$$

From equation 2.3 follows that the diffusivity can be enhanced by a reduction of the pressure. The mass transport is proportional to D/δ according to equation 2.2. Both D and δ increase with decreasing pressure, but the diffusivity improvement more than compensates the thicker boundary layer δ . Low pressure CVD (LPCVD) systems take advantage of this enhanced mass transport [20].

2.3.2 Thermodynamics

The thermodynamics in CVD concerns the feasibility of reactions as well as the nature and concentration of products. Moreover, thermodynamic calculations can provide a basis for the selection of precursors and the adjustment of appropriate operating conditions. A measure for the feasibility of chemical processes is the change in free energy of reaction ΔG_r of the system. The change in free energy is given by [14]

$$\Delta G_r = \Delta G_r^0 + RT \ln \prod a_i^{v_i} \quad (2.4)$$

where ΔG_r^0 is the standard free energy change, $\Pi a_i^{\nu_i}$ is the product of the activities of the species 'i' in the reaction, and ν_i is the stoichiometric coefficient of species 'i'. ν_i is negative for reactants and positive for products. Spontaneous reaction will occur for $\Delta G_r < 0$. After minimization of the free energy, the system will reach the equilibrium state, i.e. $\Delta G_r = 0$ and no driving force will be left for the reaction. In case of $\Delta G_r > 0$, the process will not occur [14,20].

In case the system has reached the equilibrium state (i.e. $\Delta G_r = 0$), equation 2.5 yields

$$\Delta G_r^0 = -RT \ln K \quad (2.5)$$

with the equilibrium constant K which is equal to the product of the activities $\Pi a_i^{\nu_i}$ in the state of equilibrium. The activity of a reaction partner is 1 for pure solids and for gases equal to the partial pressure. The information on the feasibility of reactions can be obtained from the values of ΔG_r^0 , which can be calculated from tabulated thermodynamic data [14,20].

Thermodynamic calculations can provide useful information on the selection of suitable precursors. Considering the customary deposition of TiN from the precursor system TiCl_4 , N_2 and H_2 , the process proceeds by the following overall reaction [21]:



The co-deposition of AlN within this system by addition of AlCl_3 according to



is not possible [22]. The reason can be seen in Fig. 3a showing the influence of the temperature on ΔG_r^0 for both reactions. The calculations exhibit negative ΔG_r^0 values for TiN formation above approximately 700°C. In practice, the reaction is executed at temperatures between 900 and 1100°C. The $\Delta G_r^0 - T$ curve for AlN formation shows an opposite behavior with a positive slope and negative ΔG_r^0 values only below 100°C [23]. Although thermodynamically possible below this temperature, the deposition process will not occur in practice due to kinetic limitations.

The triple bonded nitrogen molecule N_2 is relatively inert with a bond energy of 946 kJ/mol and high temperatures are required to break up the bonds. The deposition process can be altered by the exchange of the nitrogen source from N_2 to NH_3 . The NH_3 molecule yields a higher reactivity in comparison to N_2 , since a stepwise dissociation is possible. Less than half the energy has to be expended to break the H-NH₂ bond (460 kJ/mol), for instance [24]. The application of NH_3 has shown to enable the deposition of both TiN and AlN simultaneously [22]. The formation of TiN proceeds by the reaction [25]



and AlN according to [22]



ΔG_r^0 is negative for both reactions above temperatures of about 200 – 300°C as can be seen in Fig. 3b, i.e. the formation of both nitrides is feasible within a comparable temperature range. The slope for the formation of TiN is more negative, hence, the formation of TiN becomes more feasible with rising temperature. Publication IV reports details on the deposition of coatings within the Ti–Al–N system, especially the effect of operating conditions on the chemical and mechanical properties.

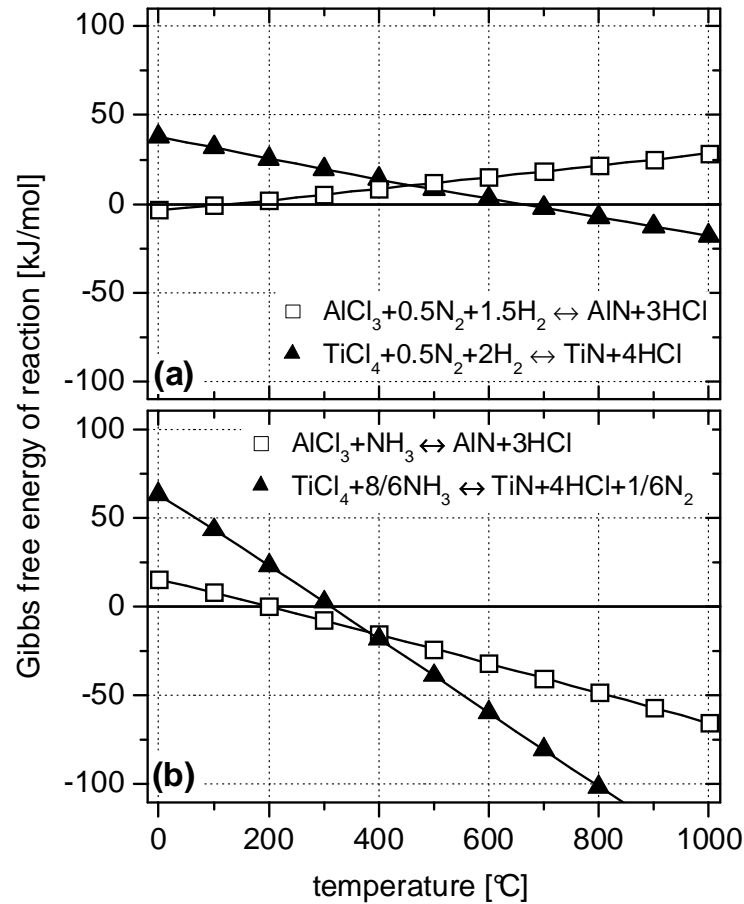


Fig. 3: Influence of temperature on Gibbs free energy of reaction for the formation of TiN and AlN from TiCl_4 and AlCl_3 , respectively, using (a) N_2 and H_2 and (b) NH_3 (adapted from [23]).

The knowledge of ΔG_r^0 in dependence on the temperature also provides insights about applicable deposition temperatures. Large negative ΔG_r^0 values at high temperatures imply a large driving force of the reaction and the reaction may not proceed at the surface as heterogeneous reaction anymore, but within the gas phase by homogeneous nucleation. For the growth of homogeneous coatings it is essential to avoid gas phase nucleation. Furthermore, depletion effects can be estimated in case of two or more simultaneous reactions. The reaction with the larger driving force may occur faster and causes the reduction of a gaseous reactant [20].

The reaction equations given above only show the overall reaction, but do not consider the presence of intermediate compounds. Modern thermodynamic calculations also

enable the consideration of all these substances and the determination of the equilibrium concentrations of complex chemical systems. The computer programs are based on the minimization of the free energy of the system considering all the different substances provided that thermochemical data are available [10,26].

Thermodynamics provides information about the driving forces of chemical reactions, but does not consider the speed of reactions. In practice, thermodynamically possible chemical reactions may appear as unfeasible because of too low reaction rates. The factors associated with the rate of chemical reactions will be discussed in following section.

2.3.3 Growth Kinetics

Growth kinetics concerns the speed of chemical reactions and focuses on fundamental information about the involved elementary reactions. The kinetics of CVD film growth is a complex issue and involves different processes at the gas/substrate interface (see Fig. 2) [20,27]. An overall reaction equation, such as $\text{TiCl}_4 + 0.5\text{N}_2 + 2\text{H}_2 \rightarrow \text{TiN} + 4\text{HCl}$ (cf. equation 2.6) for the formation of TiN does not consider the role of the surface and deficiently represents the effectively occurring processes. The different steps, especially with respect to the deposition of TiN from the $\text{TiCl}_4\text{-N}_2\text{-H}_2$ system will be discussed in the following paragraph.

Precursor transport – Delivery of precursors occurs via diffusion and convection (cf. section 2.3.1). In the gas phase, the reactants already undergo chemical reactions and form intermediate species. For example, TiCl_3 forms from the reduction of TiCl_4 by H_2 and becomes the predominantly existing Ti species for TiN deposition [28].

Adsorption – The interaction of gas molecules with surfaces can result in different adsorption processes. Physisorption arises from weak van der Waals forces between the surface and the adsorbate. The interaction between gas and surface can also form strong chemical bonds. This process is known as chemisorption and can be followed by the dissociation of the molecule (dissociative chemisorption) [27,29]. During TiN deposition, the adsorption of H_2 and N_2 involves the dissociative chemisorption on the relatively positive charged Ti sites of TiN by a catalytic reaction. Both TiCl_4 and TiCl_3 will be adsorbed on the N sites of TiN due to its relatively negative charge. The TiCl_4 dissociates into TiCl_3 , where the released Cl reacts with H to HCl [28].

Surface reaction – The adsorbed particles can diffuse on the surface, undergo the chemical reaction and are incorporated into the lattice. The surface reaction to form TiN is split into two elementary reactions. An NH ammonia radical is formed between an adsorbed hydrogen and nitrogen atom. TiN is formed by the consecutive reaction between the adsorbed NH species and the adsorbed TiCl_3 molecule [28].

Usually, the reaction mechanisms have a complex dependency on the reactant concentration. The Langmuir-Hinshelwood [29,30] adsorption behavior is frequently applied to describe surface reaction rates in CVD. The mechanism is based on the concept of the reaction between two constituents that compete for the adsorption sites on the surface. The reaction rate is maximized for a certain concentration of reactants. A surplus of either reactant will saturate the surface sites and consequently a decrease of the reaction rate. Competitive adsorption according to Langmuir-Hinshelwood can be observed in Fig. 4. The growth rate of TiN coatings increases with the TiCl_4 partial pressure $p(\text{TiCl}_4)$, but reaches a maximum and decreases for higher values. A surplus of adsorbed TiCl_4 on the surface impairs the adsorption of the required reactants H_2 and N_2 , and thus reduces the reaction speed.

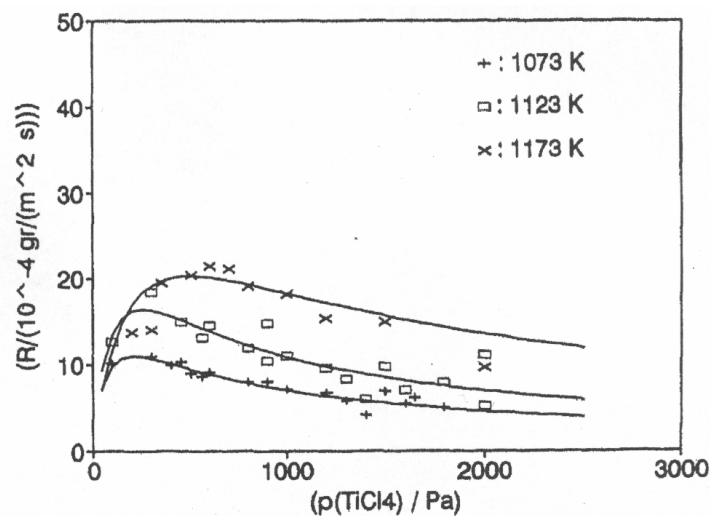


Fig. 4: Growth rate of TiN as a function of the TiCl_4 partial pressure for three different temperatures [28].

The adsorption of TiCl_4 is stronger than N_2 or H_2 and no maximum in the growth rate has been observed on the influence of the N_2 and H_2 partial pressure, which rises with increasing N_2 and H_2 content in the gas phase [28,31,32].

By-product transport – The gaseous by-products, such as HCl from the reduction of TiCl_4 by H_2 are removed across the boundary by diffusion and convection [20].

In the absence of thermodynamic limitation, each of these elementary steps can limit the overall rate of CVD reactions. Generally, the rate controlling mechanisms in CVD can be separated into [10,18]

- surface kinetics control: the growth rate is lower than the mass transport to, or from the surface and depends on the processes at the surface (e.g., chemical reaction, lattice incorporation, or desorption of by-products).
- mass transport control: the processes at the surface are faster than the mass transport to the surface.

The rate limiting mechanism can be deduced from the temperature behavior of the growth rate. The growth rate R_d in CVD reaction follows the Arrhenius law [10]

$$R_d = A e^{-E_a/RT} \quad (2.10)$$

where A is the pre-exponential factor and E_a the apparent activation energy. Schematic Arrhenius plots ($\ln R_d - 1/T$) are shown in Fig. 5 for different total pressures p_1 , p_2 , and p_3 . The surface kinetics controlled region appears in the low temperature regime and exhibits a strong dependency on the temperature, i.e. the slope of the Arrhenius plot has a high negative value typically in the range of 100 – 300 kJ/mol. At higher temperatures the surface processes are fast and the overall reaction is limited by the diffusion of reactants through the boundary layer. This mass transport limitation is characterized by a significantly smaller activation energy and slope in the Arrhenius plot, respectively [10,18].

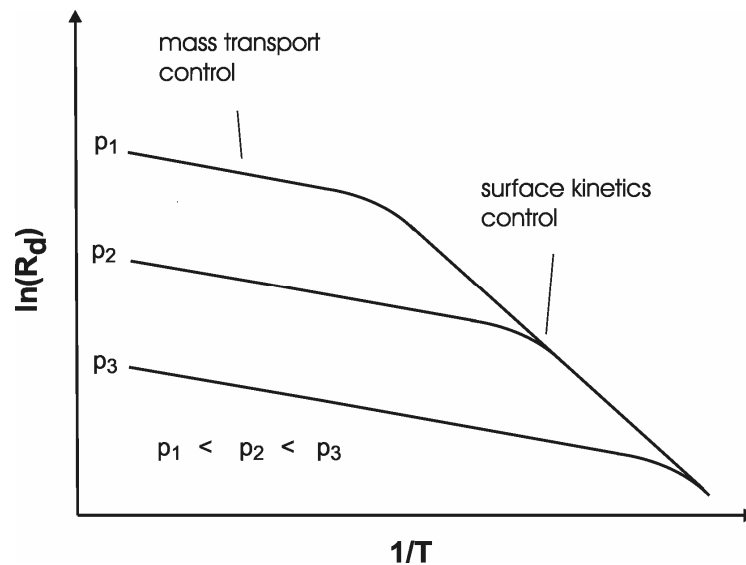


Fig. 5: Schematic Arrhenius plots for different total pressures p_1 , p_2 , and p_3 (according to [18]).

The diffusivity of the reactants (i.e., the mass transport) can be increased by a reduction of the total pressure (cf. equation 2.3). Hence, a decrease of the pressure results in an expansion of the surface kinetics control to higher temperatures as shown in Fig. 5. Most CVD processes are performed within the region of surface kinetics control. The abundant availability of precursors and a slow chemical reaction enables the deposition of homogeneous coatings independent on the reactor or substrate geometry [10,14,18].

The slope of the Arrhenius plot represents the apparent activation energy which is not equal to the activation energy of the reaction. The apparent activation energy also embraces the heat of adsorption of the reactants, hence, the determined activation energy depends on the surface coverage and ultimately on the precursor concentration. Depletion effects from the consumption of reactants by the hot reactor wall will induce changes in the reactant concentration, the growth rate (cf. Fig. 4) and consequently in

the apparent activation energy. Nevertheless, the large differences in the values for the apparent activation energy for the surface kinetics- and mass transport-controlled region enable an estimate of the rate-limiting step [28,33].

Publication I shows the Arrhenius plot for the deposition of TiN in the industrial CVD unit employed within this work. From the measured apparent activation energy of 110 kJ/mol, the deposition within the surface kinetics controlled regime has been deduced.

2.4 Coating Structure

It has been shown in the previous sections that CVD is an intricate process involving the mass transport of gases as well as the thermodynamics and kinetics of chemical reactions. Knowledge about the relationship between these processes and the deposition conditions is essential to adjust the desired coating properties. Fig. 6 illustrates the correlation between the process parameters, the CVD phenomena and the coating properties as well as their mutual interactions.

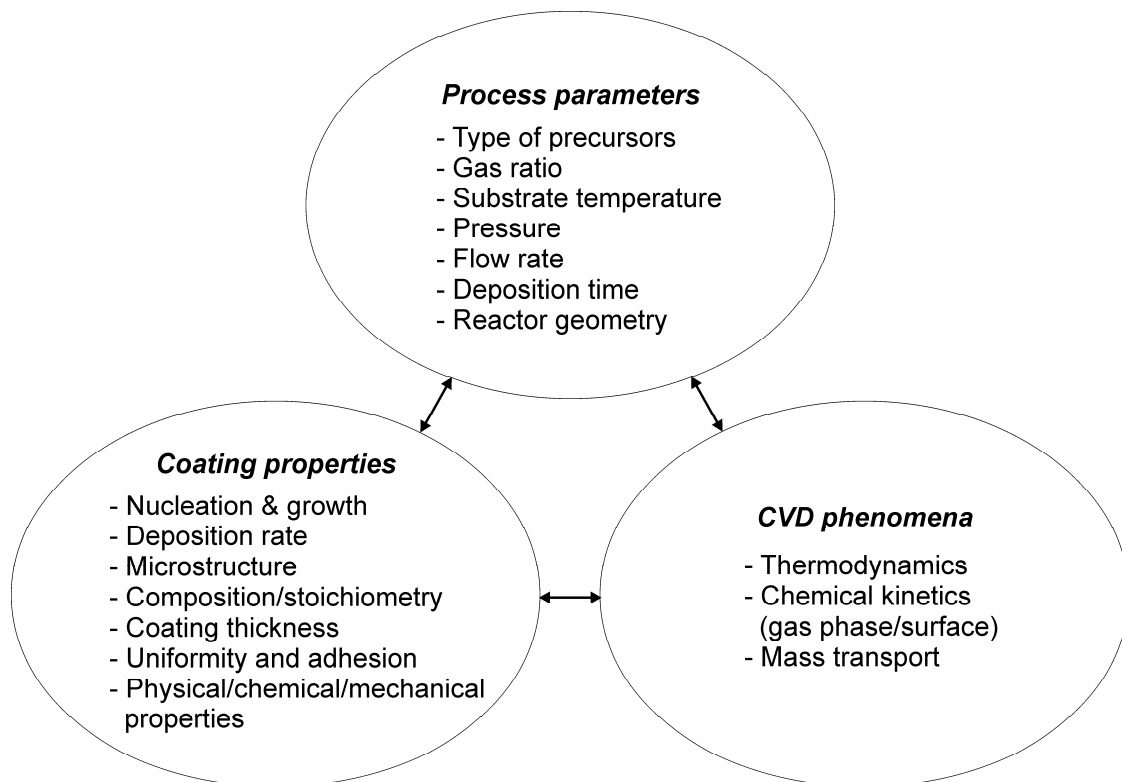


Fig. 6: Relationship between process parameters, CVD phenomena and coating properties (according to [10]).

Different mechanisms occur during the evolution of the structure, which are all influenced by the process parameter. The following sections consider the fundamental phenomena involved in the evolution of coating structures and how to control the properties by deliberate adjustment of the operating conditions.

2.4.1 Structure Evolution

The growth of thin films proceeds through several consecutive steps and each is determined by the structural conditions of the previously developed step. Fig. 7 illustrates the characteristic growth stages, where the coating forming material is marked by dark circles and bright circles represent impurities or additives. Primary nucleation of clusters on the bare substrates starts the condensation and the film growth (*stage 1*). The nucleation stage is highly influenced by the structural precondition and chemical composition of the substrate [34,35]. Especially, the chemical reactions involved in CVD can be substantially influenced by the substrate nature, e.g. the substrate can act as a catalyst and activate reactions. Organic compounds, such as CH_4 are sensitive to catalytic substrate effects. For example, the Fe-group metals Co and Ni are known to have a high catalytic activity and influence the growth, structure and properties of TiC coatings. High temperatures and chemically aggressive precursors can also result in an attack of the substrate and changes in the composition of both substrate and coating [36-38]. After the nucleation stage, the growth of dispersed discrete crystals takes place (*stage 2*).

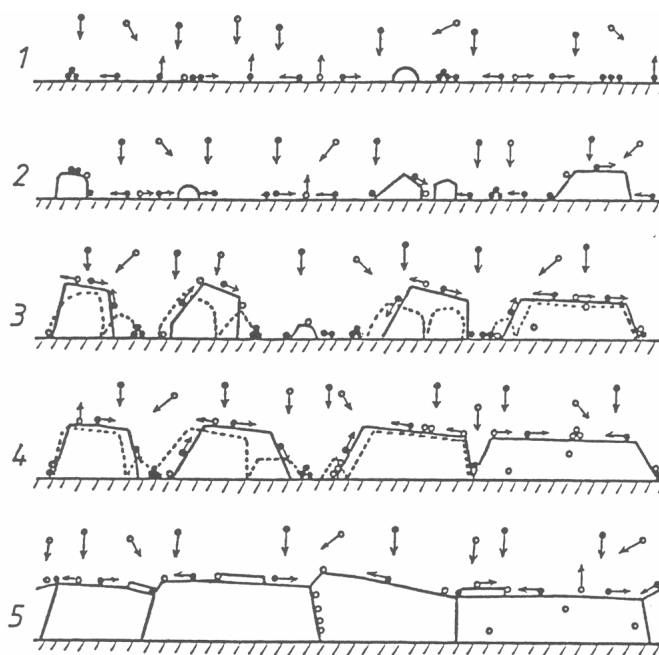


Fig. 7: Stages of structure evolution in polycrystalline thin films: 1: nucleation; 2: crystal (grain) growth; 3: coalescence; 4: filling of channels; 5: continuous film growth. Dark circles mark the coating material and bright circles impurity species [35].

The orientation and defect structure of these crystals will determine the subsequent growth processes. The growth proceeds by the direct capture of particles from the vapor phase as well as from the migration of adsorbed coating species, so-called adatoms. When the crystal size increases, adjacent crystals come into contact and the coalescence stage starts (*stage 3*). The dashed lines in Fig. 7 indicate the crystals

before the coalescence. The coalescence of crystals can be complete or incomplete. Complete coalescence causes the formation of new discrete crystals and the growth results in the change of the crystal orientation and the development of a restructuration texture related to the lowest interface energy. Incomplete coalescence produces defect containing intergranular areas. Low temperatures, contaminations at the grain boundaries, and large initial crystals hinder the migration of intergranular areas and favor the incomplete coalescence. The coalescence stage is accompanied by a contraction of the coalescing crystals leaving bare substrate areas. Condensation in these areas causes secondary nucleation and new grains. Again the secondary crystals will coalesce and the process of nucleation and grain growth will repeat. In the course of time, the channels between the crystals are filled up (*stage 4*). The coalescence stage is followed by the continuous film growth (*stage 5*) that is characterized by crystals of various orientations and the different types of grain boundaries [34,35]. Defects, such as screw dislocations, stacking faults, or reentrant corners can control the growth rate and result in highly textured coatings. The defects may already originate from the nucleation stage. Low deposition temperatures in CVD of TiN favor the nucleation of twinned crystals, for instance. For laminated twins (Fig. 8a), the fastest growth proceeds along the $[211]$ direction, which is along the (111) twin plane reentrant corners. The resultant coating morphology exhibits pyramidal or lenticular-like TiN structures.

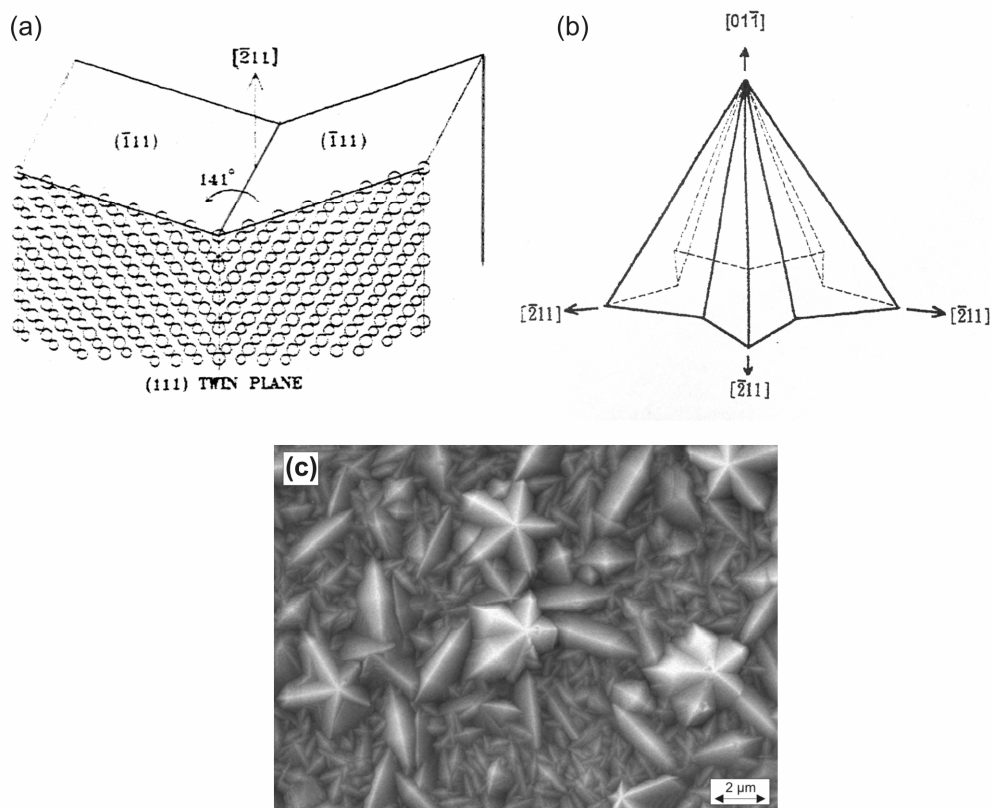


Fig. 8: Schematic illustration of an (a) laminated twinned crystal, (b) multiply twinned star-shaped crystal [39], and (c) SEM image of a TiN surface (Paper I).

In case of multiply twinned crystals, the preferred growth along five (111) twin planes with [110] co-axis creates star-shaped crystals as illustrated in Fig. 8b [39]. A mix of both star-shaped and lenticular-like structures can be observed in Fig. 8c. The scanning electron microscopy (SEM) image shows the surface of a TiN coating deposited at 850°C. High deposition temperatures cause twin-free nuclei and coating growth along the thermodynamically most favorable crystal faces. The resultant coating morphology is characterized by polyhedral structures [39]. The effect of temperature on the surface morphology is illustrated in Publication I for TiN coatings deposited between 850 and 1050°C.

The presence of impurities or additives can block the crystal growth and consequences further coating growth by repeated nucleation. The resultant film will be composed of equiaxed, globular crystals separated by the impurity phase [34,35]. Frequently observed in CVD is the incorporation of chlorine impurities from an incomplete dissociation of metal chlorides. The chlorine causes a refinement of the coating structure, but deteriorates the mechanical properties [40].

2.4.2 Process – Microstructure – Properties

Various attempts have been performed to correlate the parameters of the deposition process with the coating structure and, consequently, with the resultant properties. The influence of miscellaneous process parameters has been illustrated in so-called structure zone models (SZMs). The first SZM was introduced by Movchan and Demchishin [41] who related the structure of thick vacuum condensed metallic and oxidic coatings with the homologous temperature T_s/T_m , where T_s is the substrate temperature and T_m the melting point of the coating material. The parameter T_s/T_m is an indicator for the diffusivity (i.e., surface and bulk diffusion) and desorption of the coating material. The model has been extended by different other deposition parameters, especially for PVD methods to account on the influence of ion bombardment [42,43]. A different aspect has been considered by Barna and Adamik [44]. Based on the model of Movchan and Demichishin, the SZM proposed by Barna and Adamik considers the effect of T_s/T_m , but also includes the concentration of ‘impurities’ and different characteristic zones have been detected (Fig. 9). The term ‘impurity’ does not necessarily mean the presence of coating contaminations, but also an intended application of additives [44]:

- *Zone I* is determined by low substrate temperature and correspondingly low mobility of the adatoms. An extremely high nucleation density can be observed due to the high undercooling. The low temperatures prevent coalescence or grain boundary migration and the growth proceeds uninterruptedly in vertical direction. Therefore, the structure is characterized by fibrous grains, a high density of imperfections and

porous grain boundaries. Impurities will be incorporated in the fibrous at their impinging sites.

- *Zone T* (transition zone) consists of small grain sizes at the substrate reflecting the nucleation density followed by cone-shaped columnar crystals. The enhanced adatom mobility favors the growth of crystals of lowest surface energy and yields textured films (competitive texture). Impurities can reduce the grain boundary migration and shift zone T to higher temperatures.
- *Zone II* structures appear at temperatures, where significant grain boundary migrations sets in. Columnar grains can be observed from the substrate to the film surface. Initially formed smaller grains dissolve during the coalescence stage and a restructuration texture forms (cf. section 2.4.1). The inhibition of grain boundary migration by impurities shifts the lower temperature boundary of zone II to higher temperatures, whereas at high temperatures zone III appears.
- *Zone III* only appears in impurity contaminated films. Coverage of the growing crystals by process-induced segregation of impurities results in different grain sizes depending on the impurity level. At low contents, equiaxed micrometer sized grains form that decrease in size with rising impurity content, and finally globular nanocrystalline grains establish. At high impurity levels, zone III will extend to lower temperatures and gradually change into a zone I structure.

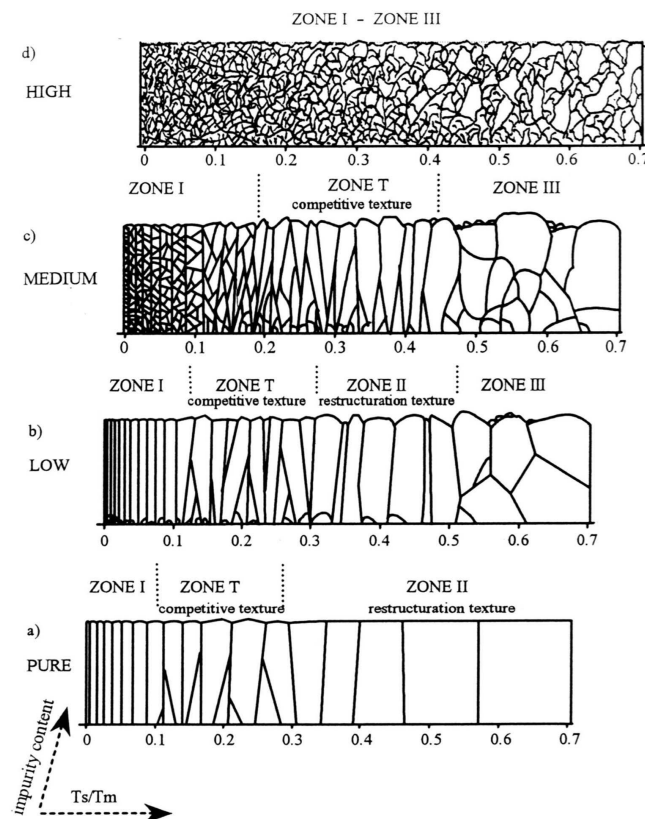


Fig. 9: Ideal (a) and real structure zone models for low (b), medium (c) and high (d) impurity concentrations [44].

The structure zone model has shown the importance of the temperature as well as the impurity level in the coating. However, a crucial parameter for the morphology of vapor deposited films is also the 'supersaturation'. The supersaturation is the concentration of reactive species in the gas phase and relates to the concentration of adsorbed species on the surface. Both nucleation and film growth are highly influenced by the concentration of adsorbed species on the surface. The level of supersaturation can be controlled by the total pressure and the partial pressures of the precursors. Fig. 10 exhibits a schematic diagram about the influence of both temperature and supersaturation on the structure of deposits for the simplest case of condensation from the vapor phase without chemical reaction. Since the reactions in CVD are thermally activated, the supersaturation in CVD process also depends on the temperature. The supersaturation generally increases with temperature, because most reactions are endothermic. Despite the fact that in some cases the opposite trend can be observed, the concept of supersaturation and temperature is still useful for many CVD coatings [45].

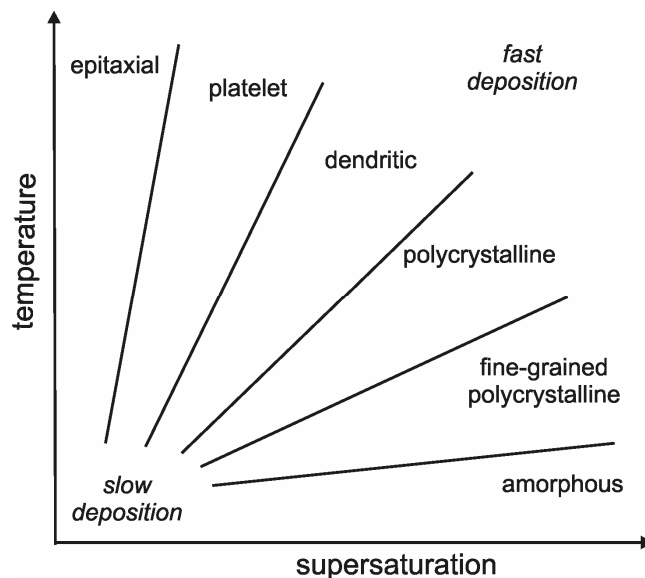


Fig. 10: Effects of supersaturation and temperature on the coating morphology (according to [12]).

At low temperatures and very high supersaturation, the mobility of the adsorbed species is low and the deposition reaction occurs basically at the sites of initial adsorption. At these conditions, the structure tends to be amorphous. An increase of temperature and decrease of supersaturation enhances the crystallinity of the deposits and produces fine equiaxed polycrystalline structures. As the temperature rises further, the mobility of the adsorbed species increases and the structure coarsens. Due to the enhanced mobility, the nucleation and growth at preferred sites, such as kinks or ledges becomes increasingly important and the coatings change to dendritic structures. At low supersaturation and high temperatures, the growth changes from platelets to ultimately epitaxial structures [10,12].

Besides SZMs that consider only general deposition parameters, e.g. temperature and supersaturation, models for certain coating materials have been developed. For example, the influence of deposition temperature and composition on the morphology of CVD deposited $\text{TiC}_x\text{N}_{1-x}$ coatings ($0 \leq x \leq 1$) has been investigated by Cheng et al. [46].

Since the microstructure of coatings and the surface morphology define the mechanical and tribological properties to a great extent, all coatings examined within this work have been characterized with respect to their structure. The results are represented in for the single-phase coatings TiN (Publication I) and $\text{TiC}_x\text{N}_{1-x}$ ($0 \leq x \leq 1$) (Publication II). The properties of multi-phase coatings Ti–N–B and Ti–Al–N are shown in Publication III and IV, respectively.

3 CVD of Hard Coatings

3.1 General

The deposition of hard coatings is a versatile method to protect materials and prolong the life time of tools. Over the years, different coating materials have been developed according to miscellaneous demands. The properties of these materials, such as hardness, chemical stability, or ductility originate from the bonding structure of the atoms. The hard materials can be classified into three groups depending on the dominating chemical bonding character: metallic, covalent, and ionic. Usually, the bonding character in hard materials is generally a complex interaction of all three types. Based on the bonding structure, each material group offers distinctive advantages, e.g. metallic hard materials show a good adhesion to metallic substrates and a high toughness, but a lower hardness compared to covalent hard materials (Fig. 11). From this follows that a single coating may not fulfill all the requirements for certain applications. In practice, combinations of diverse coatings are applied to achieve an optimum performance [1,47,48].

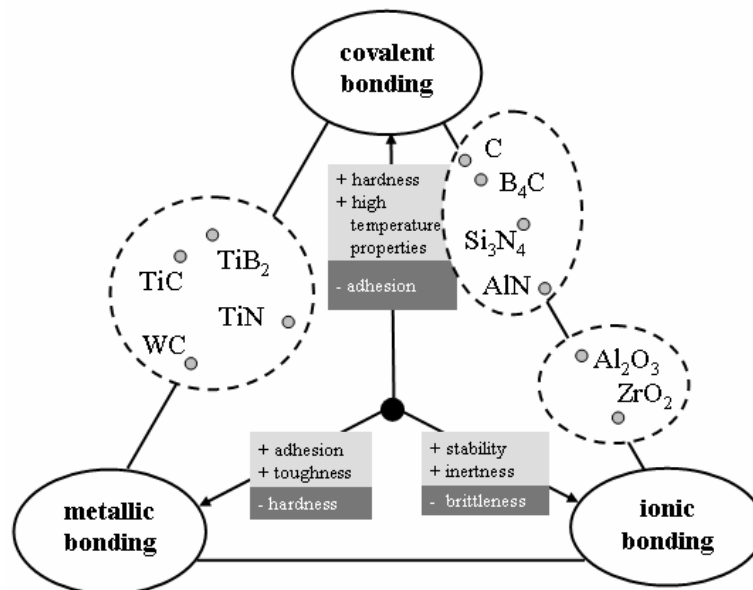


Fig. 11: Classification of hard materials according to the bonding character [47].

Here, the attention is given to metallic hard materials, particularly, the borides, nitrides, and carbides of titanium. Important aspects for the deposition of wear resistant coatings are their hardness, brittleness, stability, interaction tendency with other materials (e.g., the workpiece during cutting), or the adherence to metallic substrates. The next sections outline important properties of hard coatings – especially focused on the coating systems investigated within this work (see Publication I–IV) – and show aspects on the design of CVD hard coatings.

3.2 Design Aspects

3.2.1 Hardness

The hardness of coatings is a complex issue and embraces not only the strength of interatomic forces (i.e., the intrinsic hardness), but also the dislocation structure and its interaction with the microstructural features. Significant parameters for the hardness are the phase composition, impurities, grain size, crystal structure, or texture. In the following, the aspects of intrinsic hardness, the grain size and its manipulation, the texture, and the influence of metastable structures will be discussed [49,50].

Intrinsic Hardness

Hard materials are characterized by a high cohesive energy, short bond length, and a high degree of covalent bonds. The intrinsic hardness of a material lowers as the covalent bonds decrease and metallic or ionic components rise. This means that the hardness of a material can be modified by changing the non-metallic element, for instance. Within the quasi-binary system TiN–TiC, nitrogen atoms can be arbitrarily replaced by carbon atoms. Due to the replacement of nitrogen atoms, the degree of covalent bonds increases, and thus, the hardness increases from TiN to TiC [49]. The influence of the carbon content on the hardness of $\text{TiC}_x\text{N}_{1-x}$ coatings is also shown in Publication I. The borides of transition metals, such as TiB_2 are harder than the corresponding carbides or nitrides. While nitrides and carbides form covalent bonding components between the transition metal and the non-metal, a network of covalent bonds arises between the boron atoms. The direct linkage between the boron atoms is responsible for the high hardness [49,51].

Grain Size

The hardness can be further enhanced by controlling the grain size of the material according to the Hall-Petch relation [20,52]:

$$H = H_0 + kd^{-1/2} \quad (3.1)$$

where H is the hardness, H_0 the intrinsic hardness of a single crystal, k a material constant, and d the grain size. The grain size in coatings can reach down to several nanometers depending on the deposition technique and the coating material [53]. However, CVD coatings frequently suffer from coarse structures. High deposition temperatures preferentially result in coarse columnar growth structures with column diameters in the micron range [16,54,55]. The grain size can be modified by adjustment of the deposition parameter, i.e. deposition temperature and supersaturation (see section 2.4). Fine-grained structures require low deposition temperatures and a high supersaturation of reactive gases (cf. Fig. 10). However, lowering the deposition temperature and increasing the partial pressure of the precursor, e.g. TiCl_4 may result

on one hand in fine structures, but on the other hand in unacceptable low deposition rates and the incorporation of high concentrations of impurities. Most common in application of metal chloride precursors is the presence of chlorine. Since the chemical reactions are thermally activated, low temperatures cause an incomplete dissociation of the metal chlorides. Chlorine impurities are known to reduce the grain size, but also to deteriorate the coating hardness [9,25,40]. Furthermore, low deposition temperatures favor the formation of weak or voided grain boundaries (see chapter 2.4.2). The presence of voids is detrimental for the material strength and the hardness may decrease even below the bulk value [49,56].

Grain refinement can be induced by the addition of “doping” elements, e.g. oxygen and boron are well-known to control the grain size of coatings [57-60]. The grain size of CVD coatings can be also manipulated by co-deposition of an immiscible second phase. The minor component segregates to the growing crystal faces and develops its own phase. The second phase prevents the coalescence of the coating crystals and, furthermore, induces repeated nucleation [61]. Fig. 12 exhibits the influence of boron addition to TiN on the coating hardness and fracture morphology. The interrupted columnar growth at 0.3 at.% B can be ascribed to the grain refinement effect of dissolved boron. The correspondingly smaller grain size significantly enhances the coating hardness from 20 to 27 GPa.

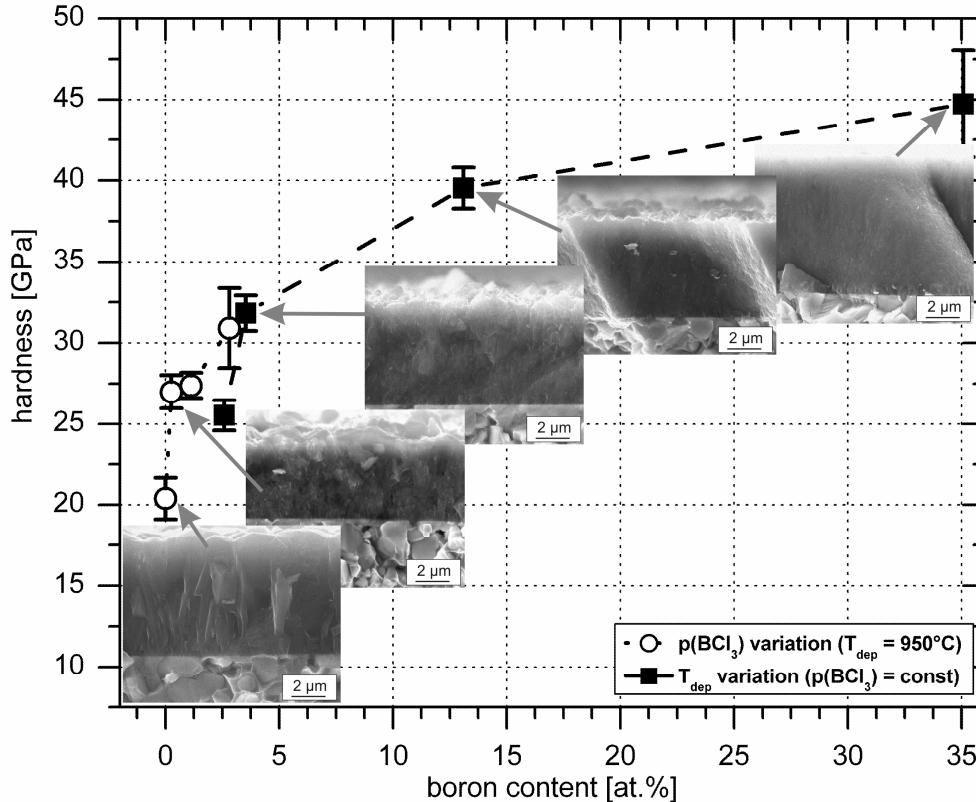


Fig. 12: Influence of boron content on coating hardness and fracture cross-section of Ti-N-B coatings (according to [62] and Paper III).

The solubility limit of B in TiN is very low (< 1 at.% B) and exceeding the solubility consequences the formation of TiB₂ as second phase. The occurrence of TiB₂ has a high impact on the hardness, since TiB₂ (3000 HV) is harder than TiN (2100 HV) [48]. As shown in Fig. 12, the hardness increases further from 27 GPa at 0.3 at.% B up to 45 GPa as the boron concentration rises to 35 at.%, and with it the TiB₂ content. Further information about CVD Ti–N–B coatings can be found in Paper III.

Texture

Coatings deposited by CVD commonly exhibit a strong preferred orientation. The orientation that will form depends on the deposition parameters, especially the temperature and precursor supersaturation (cf. section 2.4). Changes in texture can result in differences in hardness depending on the hardness anisotropy of the material. Transition metal nitrides, such as TiN are well-known for their anisotropic hardness behavior and the influence of texture on the hardness of single-crystalline TiN has been clearly shown [63-65]. Nevertheless, the results on polycrystalline films are inconsistent in literature. Depending on the deposition technique or the considered orientations, different result can be observed. Either the (111) or (110) textured films are usually referred to show the highest hardness [66-69].

Frequently, the texture of coatings is described using the texture coefficient according to Harris [70]. The texture coefficient $TC_{(hkl)}$ for the planes (hkl) is defined as

$$TC_{(hkl)} = \frac{I_{(hkl)} / I_{0,(hkl)}}{1/n \sum I_{(hkl)} / I_{0,(hkl)}} \quad (3.2)$$

where $I_{(hkl)}$ is the measured peak intensity and $I_{0,(hkl)}$ is the standard intensity of powder material both measured in $\theta/2\theta$ configuration, and n the number of considered reflections. The standard intensities can be obtained from databases, e.g. the Joint Committee of Powder Diffraction Standards (JCPDS) – the so-called powder diffraction files. Calculating the texture coefficient is a fast and simple approach to obtain information about the degree of texture for coatings showing a fiber texture with coinciding fiber axis and substrate normal. The maximum value of $TC_{(hkl)}$ is n for a perfectly oriented material and 1 for a random orientation [71].

The change in texture of TiN coatings with the deposition temperature is exhibited in Fig. 13a. At the lowest temperatures, a strong (211) orientation can be observed (cf. Fig. 8), which diminishes at higher temperatures. Between 950 and 1050°C, only a slight preferred (100) orientation can be observed at 1000°C, while the other coatings show no clear texture. The texture affects the coating hardness as presented in Fig. 13b. The (211) textured films clearly yield a lower hardness compared to the random oriented coatings.

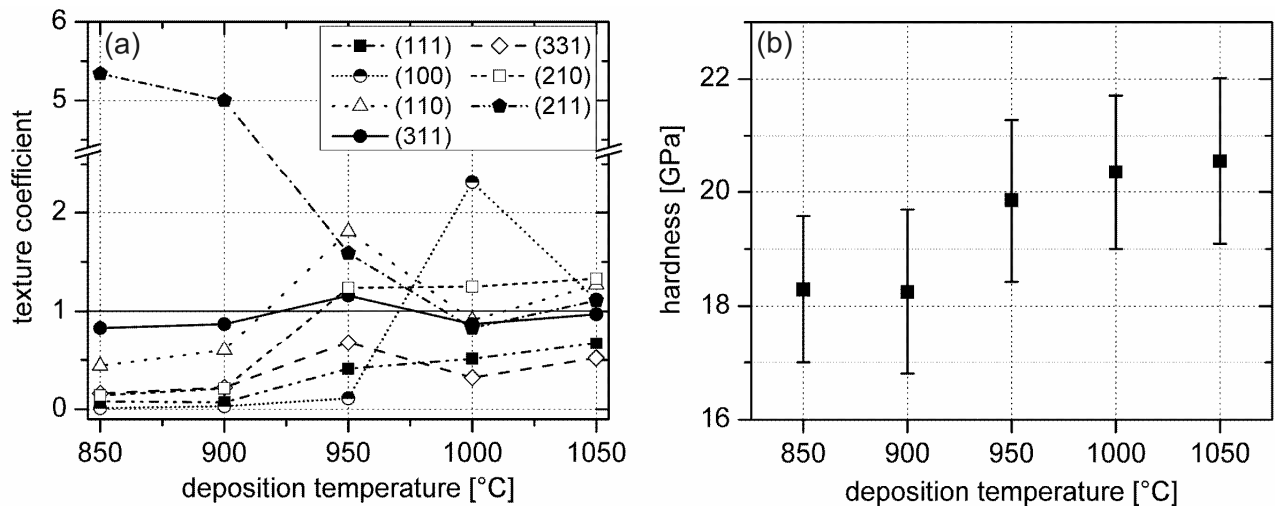


Fig. 13: Texture coefficient (a) and hardness (b) of TiN coatings deposited between 850 and 1050°C (Publication I).

Metastable Coatings

An important issue in coating technology is the deposition of metastable coating structures. In principle, the condensation of a multi-component coating from the vapor phase causes an intermixed state of atoms. To form ordered structures and reach the equilibrium state, the atoms have to diffuse certain distances before they are imbedded by further atoms arriving from the gas phase. The required distance depends on the composition of this stable configuration, where two phase or multiphase coatings require longer diffusion paths to find a stable arrangement and, thus, are favored to form metastable phases. The metastable assembly can be obtained in case the diffusion length of the deposited atoms is lower than the distance to form the stable phase. For this, bulk diffusion has to be negligible small and surface diffusion only occurs in the nanometer range, i.e. the temperature has to be small ($\sim 0.3 T_s/T_m$) [47,72]. A common representative for metastable hard coatings is the quasi-binary system TiN–AlN. In thermodynamic equilibrium, the face-centered cubic (*fcc*) TiN and hexagonal close packed (*hcp*) AlN are practically immiscible at room temperature. The coatings for wear protection show a *fcc* structured supersaturated solid solution *fcc*–Ti_{1-x}Al_xN ($0 \leq x \leq 1$) [73-75]. The replacement of Ti atoms in the TiN lattice by Al is responsible for an enhanced coating hardness due to solid solution hardening. Moreover, the coatings are characterized by an enhanced hot hardness. At elevated temperatures, the metastable structure decomposes into the stable components via spinodal decomposition and intermediately formed cubic TiN and AlN domains provide a hardness increase at high temperatures [52,76]. Although metastable structures are favored by the non-equilibrium character of PVD techniques, such as sputtering or cathodic arc techniques, metastable structures have been also observed in thermal CVD coatings as described in Paper IV and [77-79].

3.2.2 Chemical Stability

Hard coatings may show a good resistance against detrimental mechanical loads, but completely fail at high temperatures and aggressive environmental media. In this case, the chemical inertness is the decisive factor and not the hardness. The chemical attack may result from exposure in ambient air at elevated temperatures, but also occurs at the tool/workpiece contact during cutting applications in the form of chemical wear, for instance. Ionic hard materials, like Al_2O_3 or ZrO_2 show highest chemical stability and lowest interaction tendency, but also a lower hardness and a high brittleness (cf. Fig. 11) [1,2]. However, attention is given to metallic hard materials within this work, and their interactions with the environment.

The replacement of nitrogen atoms by carbon in TiN increases the hardness as mentioned previously, however, at the same time the resistance against oxidation decreases [80-82]. The oxidation of $\text{TiC}_x\text{N}_{1-x}$ ($0 \leq x \leq 1$) results in the formation of TiO_2 and the release of CO_2 and N_2 . Two processes have been suggested to occur during the oxidation of $\text{TiC}_x\text{N}_{1-x}$ ($0 \leq x \leq 1$): the dissolution of oxygen into the interstitial sites and the substitution of carbon and nitrogen by oxygen [83]. However, fundamental investigations on the reactions with oxygen have mainly focused on the oxidation of the binary compounds TiN [84-86] and TiC [87-89]. Since the oxidation behavior is dependent on various factors, such as the composition, the temperature, the heating rate, or the oxygen partial pressure, for instance, different oxidation mechanisms have been proposed. Most investigations have separated the establishment of oxynitrides TiN_xO_y and oxycarbides TiC_xO_y , respectively, as intermediate step prior to the formation of rutile, which is the stable modification of TiO_2 . Only few have observed additional oxidation stages, e.g. TiO formation [85] or the influence of the metastable polymorphs of TiO_2 , such as anatase, on the oxidation kinetics [90]. Many investigations focus on temperatures above 600°C and/or long oxidation times. Both favor the formation of the stable TiO_2 phase. The importance of the intermediate oxides on the oxidation behavior of $\text{TiC}_x\text{N}_{1-x}$ coatings is illustrated in Fig. 14. $\text{TiC}_{0.71}\text{N}_{0.29}$ coatings deposited on cemented carbide with an $0.5 \mu\text{m}$ thick TiN interlayer have been tested by dry-sliding experiments (ball-on-disc arrangement against Al_2O_3 balls) at 500°C and 600°C (see Fig. 14a and b, respectively). After heating-up (approx. 30 min), the samples were kept at the temperature for 2 h prior to the test. At 500°C the coating yields an extensively oxidized zone visible as a dark layer in the backscattered electron SEM image. Glow discharge optical emission spectroscopy (GDOES) depth profiles confirm this result and exhibit an oxygen penetration deep into the coating. At this temperature, the oxide layer predominantly consists of anatase as measured by Raman spectroscopy, whereas rutile turns out to be the main component at 600°C . The change of the oxide layer is accompanied by an enormous decrease of oxidation.

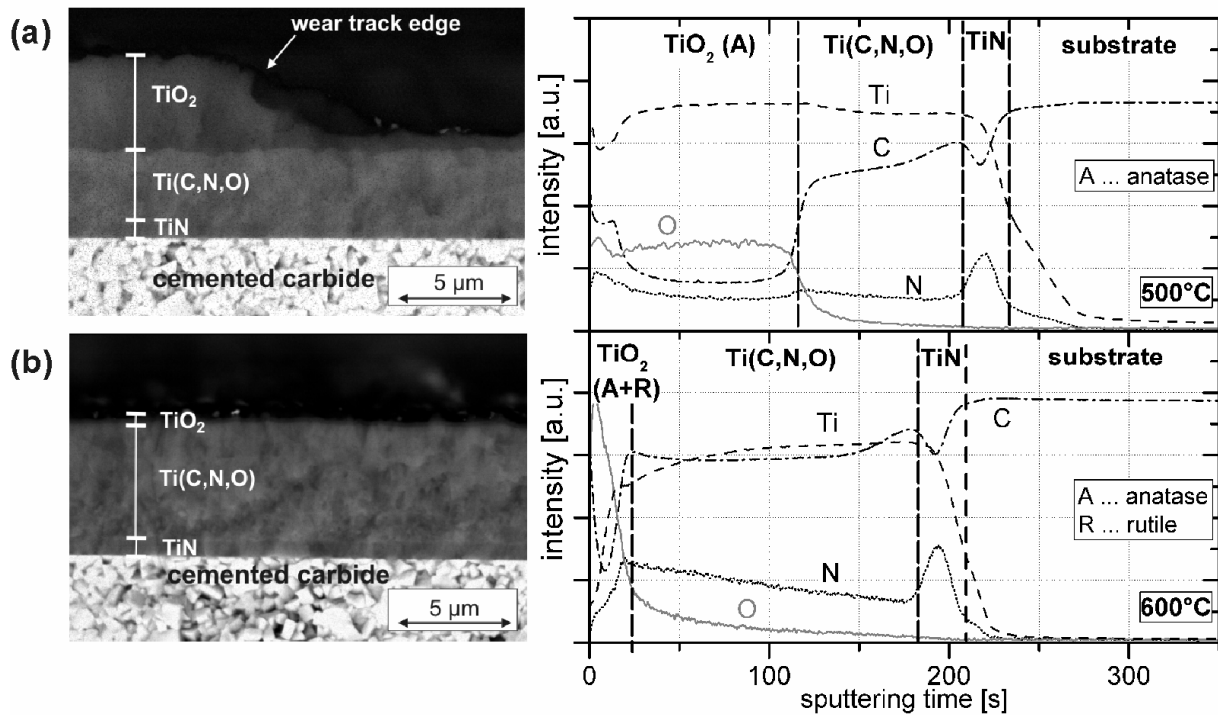


Fig. 14: Backscatter SEM images of fracture cross-sections and GDOES depth profiles of $\text{TiC}_{0.71}\text{N}_{0.29}$ coated ball-on-disc samples oxidized at (a) 500°C and (b) 600°C for 2 h. The coatings have been deposited on cemented carbide with an interlayer of $0.5\ \mu\text{m}$ TiN. The different coating regions and the wear track edge are indicated in image (a) and (b) (Paper II).

The oxygen content at the surface is high, but limited to a narrow region at the surface (Fig. 14b). It has been suggested that the rutile layer is denser and more efficiently retards the oxidation process than anatase. Moreover, the tendency of anatase formation is promoted by carbon, i.e. the oxide scale increases with the carbon content, especially at 500°C . More details about the oxidation behavior of $\text{TiC}_x\text{N}_{1-x}$ coatings and its impact on the tribological properties can be found in Publication II.

The chemical stability of TiN coatings can be enhanced by the boron incorporation into the TiN lattice and formation of a $\text{Ti}(\text{N},\text{B})$ solid solution as well as co-deposition of TiB_2 besides TiN [81,91]. The improved oxidation resistance is provided by the formation of vitreous B_2O_3 besides TiO_2 starting at 600°C at the interfacial boundaries. The B_2O_3 causes a densification of the oxide scale and diminishes the oxygen diffusion. Pores and macro-defects, like cracks, can be healed due to the molten state of B_2O_3 and the large difference in specific volume between B_2O_3 and TiO_2 . The high vaporization rate of B_2O_3 reduces the efficiency of the protective scale above 1000°C [91-93]. Although it is generally accepted that the oxidation resistance improves by boron addition, the opposite behavior has been observed for TiN/ TiB_2 containing CVD coatings at 500 and 600°C (see Publication III). The lowest oxidation resistance has been found at the highest boron content at 500°C , but considerably improved at 600°C . Comparable to $\text{TiC}_x\text{N}_{1-x}$ coatings, preferred anatase formation occurred at 500°C with rising boron

concentration accompanied by extensive coating oxidation. The formation of rutile and possibly B_2O_3 has been suggested to reduce the oxygen diffusion into the coating.

So far, the effect of some interstitial elements on the oxidation resistance of TiN has been discussed. The oxidation properties can be also enhanced by incorporation of metal atoms, such as Al into the TiN lattice. The onset of oxidation raises from around 550°C for TiN to 750°C or even higher for $fcc-Ti_{1-x}Al_xN$ coatings. The exact oxidation start depends on the Al content and the coating structure [8,73,94]. The enhanced oxidation resistance results from the formation of a stable passive double-layer oxide: an Al-rich oxide layer at the top and adjacent a Ti-rich oxide layer. During the oxidation process, the Al atoms diffuse through the Ti-rich oxide layer towards the oxide/gas interface, while oxygen counterdiffusion provides O to the nitride/oxide interface. The rate-limiting step for oxidation is the diffusion of oxygen atoms through the Al-rich oxide layer, which results in a 3 – 4 orders of magnitude smaller oxidation rate constant for $Ti_{0.5}Al_{0.5}N$ compared to TiN [95].

Another alloying elements which can be found to improve the oxidation stability of TiN coatings is Si. Oxidation experiments on TiN/ Si_3N_4 nanocomposite PVD coatings showed an improvement of the oxidation resistance [96,97]. Layers of amorphous Si_3N_4 protect the encapsulated TiN crystallites from oxidation. The oxidation rate is low up to a certain temperature above which rapid oxidation occurs. This transition temperature is a function of the Si content and the Si_3N_4 layer thickness, respectively. Nevertheless, the preparation of Si-alloyed TiN films by thermal CVD is challenging. Millimeter thick Si_3N_4 /TiN composites have been deposited at temperatures above 1050°C from the $TiCl_4 - SiCl_4 - NH_3$ system [98]. Increasing the reactivity of the Si precursor by using $SiCl_2H_2$ and lower temperatures (850 – 1100°C) causes the formation of titanium silicides beside TiN [99].

Disadvantageous in the application of metal chloride precursors is the incorporation of chlorine in the coatings. The chlorine is well-known to reduce the oxidation stability of coatings [100]. The contamination with chlorine becomes problematic, especially at low deposition temperatures, where the coatings suffer from an incomplete dissociation of the reactant molecules [9,25].

3.2.3 Adhesion

An excellent adhesion to the substrate is a necessary precondition for the performance of tools. The adhesion of coatings depends on the substrate surface morphology, chemical interactions, impurities, and the nucleation behavior of the depositing atoms. Generally, metallic hard coatings exhibit a good adhesion to metal substrates. The ductile character of the interface offers a good resistance against interfacial failure. Since plastic deformation is feasible, a high amount of energy is necessary to propagate

interfacial cracks, whereas interfaces dominated by ionic or covalent bonds frequently suffer from brittle fracture. Both tensile and compressive stresses may generate coating failure and the mechanism depends on the coating/substrate properties [1,101]. Ceramic hard coatings deposited by thermal CVD on cemented carbide commonly show tensile stresses and frequently contain micro-cracks. The stresses mainly arise during the cooling period from the differences in thermal expansion, where the low thermal expansion coefficient of cemented carbide ($\alpha = 5 - 6 \cdot 10^{-5} \text{ K}^{-1}$) compared to ceramic coatings ($\alpha = 7.5 - 9 \cdot 10^{-5} \text{ K}^{-1}$) is responsible for the tensile stresses. The stresses in coating and substrate also determine the interfacial shear stresses the interface has to withstand. The extent of thermal mismatch stresses can be minimized by combining reasonable material combinations and coating thicknesses [102,103].

Clean substrates without contamination from hydrocarbons or oxides are generally desirable for well-adherent coatings. The substrates are cleaned and degreased prior to the deposition process. Residual contaminations as well as oxide layers are removed by chemical reduction with H_2 at elevated temperatures [19,104]. However, the impurities may appear from the coating itself. For example, high chlorine concentrations in coatings reduce the adhesion. The chlorine atoms diffuse to the coating/substrate boundary and corrode and weaken the interface in the course of time [25].

The adhesion can be enhanced by roughening of the surface. The mechanical interlocking between surface and coating increases the effective contact area and contributes to an improved adhesion [101].

Thermal CVD coatings deposited at high temperatures typically provide an excellent coating adhesion. The high temperatures ensure interdiffusion between coating and substrate and lead to the formation of gradual changes in composition and stress distribution. Extensive diffusion, however, may deteriorate the adhesion by formation of Kirkendal porosity or brittle phases at the interface [101,105]. Well-known in CVD of TiC is the problem of η -phase formation, where the carbides $\text{W}_6\text{Co}_6\text{C}$ and $\text{W}_3\text{Co}_3\text{C}$ develop. Under decarburizing conditions, i.e. an insufficient supply of carbon from the gas phase, carbon from the substrate diffuses to the surface and reacts with TiCl_4 and forms TiC. The reduced carbon content in the substrate causes the formation of the η -carbides. Especially, the development of $\text{W}_6\text{Co}_6\text{C}$ is detrimental to the adhesion and, finally, the performance of coated cemented carbide tools [106,107].

Interfacial reactions may also occur from the diffusion of coating elements into the substrate. Especially, high temperatures and/or high contents of these elements favor massive reactions. Silicon containing precursors may lead to the formation of silicides with the substrate, e.g. cobalt silicides in case of cemented carbide substrates [108]. Also boron is known to react with cemented carbide substrates. During the deposition of

boron containing layers, the boron diffuses into the substrate and forms borides, such as CoB, WCoB, or W_2CoB_2 [109]. The deposition of interlayers, e.g. TiN or TiC, can reduce the diffusion of boron or silicon to some extent [109,110]. Thick coatings may be required to completely prevent diffusion of these elements. The effect of a 0.5 μm thin TiN interlayer on the diffusion of boron during Ti–N–B coating deposition can be seen in Fig. 15 on GDOES concentration depth profiles. The coatings were deposited at 900°C on cemented carbide. The interlayer is marked and can be identified by an enhanced Ti and N concentration. A constant B content can be observed in the Ti–N–B coating, but decreases within the TiN coating. Behind the intermediate layer, a boron enrichment in the substrate can be observed. Changes in the substrate could be also detected on etched cross-sections by light optical microscopy, while XRD measurements confirmed the formation of W_2CoB_2 (see Publication III). Thus, the TiN layer was not thick enough to act as a diffusion barrier at this temperature and high boron contents in the coating.

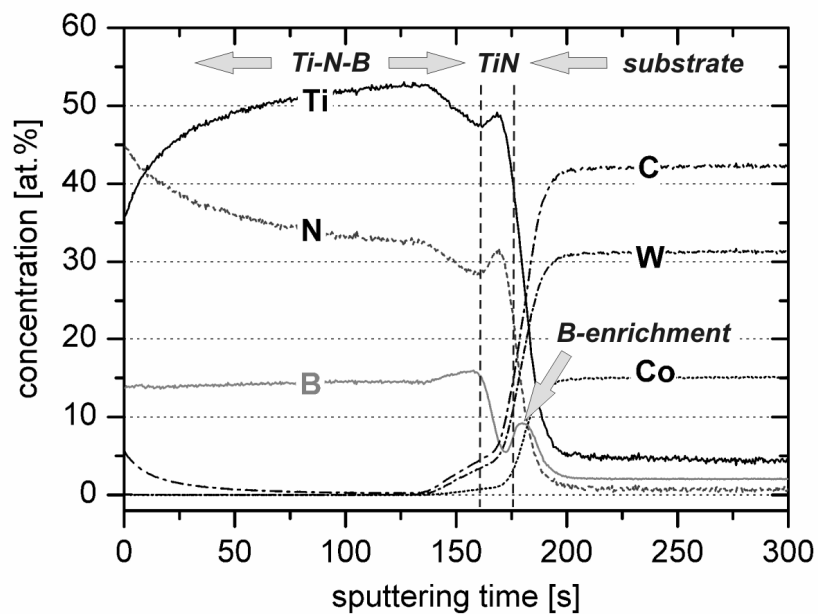


Fig. 15: GDOES depth profile of a Ti–N–B coating deposited at 900°C on cemented carbide with a 0.5 μm thick TiN interlayer. From the substrate, only the concentration profiles of W, C, and Co are presented, but not Ta and Nb for the sake of clarity.

3.3 TiN

The application of TiN as hard and wear resistant coating is well-established in cutting industry, because of the excellent combination of hardness, toughness, thermal stability as well as its pleasant golden color. TiN belongs to the group of interstitial compounds and crystallizes in *fcc* B1-NaCl structure. The binary phase diagram Ti–N is shown in Fig. 16 and exhibits that TiN is stable over a wide composition range. Nitrogen-to-titanium ratios between 0.6 to 1.16 have been reported for bulk materials [111]. For under-stoichiometric films ($N/Ti < 1.0$), vacancies reside on the N-sublattice, whereas the vacancies are on the Ti-sublattice in case of over-stoichiometric compositions

($N/Ti > 1.0$). Details about the bonding mechanisms, the microstructure and properties of TiN coatings are given in [64,111,112,].

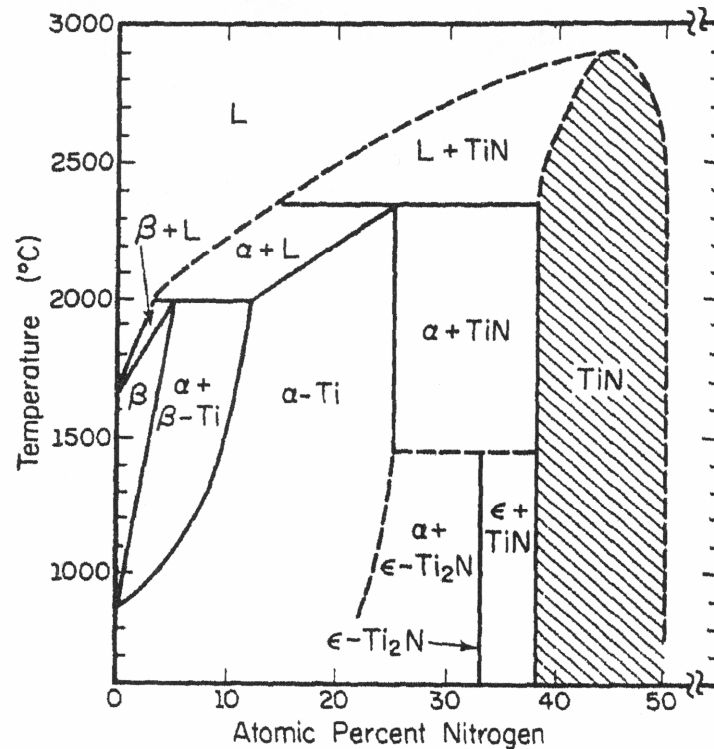


Fig. 16: Binary phase diagram Ti-N [111].

The deposition of TiN for cemented carbide cutting tools by thermal CVD is typically carried out from gas mixtures of $TiCl_4$, N_2 , H_2 , and Ar according to reaction 2.6 (section 2.3.2). $TiCl_4$ and N_2 provide the elements that constitute the coating, while H_2 acts as reducing agent. The inert gas component Ar is used as a carrier gas and to provide a total flow rate large enough to achieve reasonable mass fluxes and ensure tolerable deposition rates. The composition of these films is usually stoichiometric with negligible chlorine incorporations. The coatings are characterized by an excellent adhesion to cemented carbide and a columnar microstructure [21]. The influence of the process parameters on the structure and properties of TiN coatings is examined in Publication I.

The process temperatures for TiN formation can be lowered by means of replacing the nitrogen source N_2 by NH_3 (see reaction equation 2.8). The deposition temperatures are in a range of 550 to 750°C. This low temperature process has been investigated especially with respect to the application of TiN as a diffusion barrier in microelectronics [113,114], but less investigations have focused on wear protective properties [115]. The coatings exhibit an advantageous fine-grained structure; however, possible drawbacks of this process are a lower film density and the incorporation of high amounts of Cl. $TiCl_4$ and NH_3 also form solid complexes of the type $TiCl_4 \cdot nNH_3$ in the gas phase up to approximately 250°C; hence, the gases have to be pre-heated prior to mixing. Excess

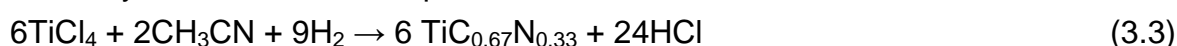
NH_3 may also react with HCl and forms NH_4Cl which plugs the exhaust gas system [13]. The low temperatures favor non-stoichiometric TiN films, where both under- and over-stoichiometric films have been reported [9,13,116]. TiN deposited within this precursor system was investigated in the course of Ti-Al-N coating development (see Publication IV).

Although not yet applied to cutting tools, TiN films can be deposited using organometallic precursors, such as tetrakis dimethylamido titanium $\text{Ti}(\text{N}(\text{CH}_3)_2)_4$. However, these precursors are expensive, hazardous to handle, and the films suffer from poor adhesion and high impurity contents [117,118].

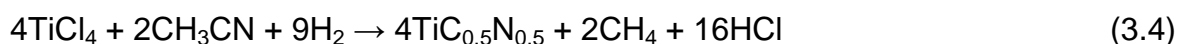
3.4 Ti–C–N

The interesting region within the ternary system Ti-C-N for the deposition of hard coatings is the TiN-TiC quasibinary system. TiC has the same crystal structure as TiN (B1-NaCl), but yields a higher hardness due to a more pronounced covalent bonding. Complete miscibility occurs between TiN and TiC , where nitrogen can be arbitrarily substituted by carbon in the *fcc* structure and a $\text{TiC}_x\text{N}_{1-x}$ ($0 \leq x \leq 1$) solid solution forms. The gradual variation in composition enables also a continuous adjustment of the coating properties [49].

Nowadays, two processes are in use to deposit $\text{TiC}_x\text{N}_{1-x}$ coatings onto cutting tools [7]. Starting from the precursors for TiN deposition (i.e., TiCl_4 , N_2 , H_2 , and Ar), the carbon is supplied by the addition of CH_4 . The process is usually carried out between 850 and 1050°C. The carbon content x in $\text{TiC}_x\text{N}_{1-x}$ coatings can be adjusted between 0 and 1 by changing the partial pressures of CH_4 and N_2 as well as the deposition temperature (see Publication II, [46]). Varying deposition temperature and coating composition change the structure and morphology of $\text{TiC}_x\text{N}_{1-x}$ coatings. A model for the structure of $\text{TiC}_x\text{N}_{1-x}$ coatings has been proposed by Cheng et al. (Fig. 17). The morphology changes from rounded hillocks to a plate-like structure, and finally pyramidal crystals as the deposition temperature increases. With rising carbon content, the structures coarsen, such as from thin to thick plates [46]. The second process to deposit $\text{TiC}_x\text{N}_{1-x}$ films employs CH_3CN instead of CH_4 . The deposition temperatures are lower and typically between 800 and 900°C. Hence, this process is often called MTCVD process to emphasize the lower temperatures. Depending on the temperature, two competing reaction paths for $\text{TiC}_x\text{N}_{1-x}$ formation have been formulated by Bonetti et al. [119]. At approximately 850°C, the reaction proceeds via



while at lower temperatures higher N contents can be found due to the following reaction:



Compared to the application of CH_4 , the compositional range is limited to a narrow range. MTCVD coatings show distinct columnar structure of preferred (211) orientation, whereas HTCVD coatings consist of equiaxed grains. Most cited advantages of MTCVD coatings are the lower tensile stresses due to the reduced temperatures and the reduced tendency for decarburization and η -phase formation [7,16,119].

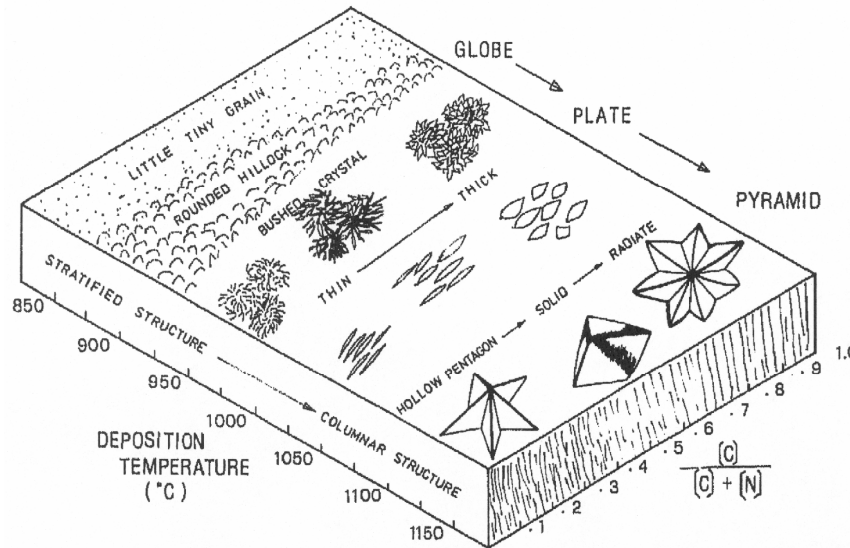


Fig. 17: Influence of deposition temperature and composition on the coating morphology of $\text{TiC}_x\text{N}_{1-x}$ deposited from the $\text{TiCl}_4\text{-H}_2\text{-N}_2\text{-CH}_4$ system [46].

3.5 Ti-B-N

The ternary phase diagram of the Ti-B-N system is schematically shown in Fig. 18. It is subdivided into five different zones labeled 1 to 5 according to the combination of coexisting phases. Furthermore, the hardness distribution is indicated by different grey scales. The phases of highest hardness are TiB_2 (3000 HV) followed by TiN (2100 HV); hence, the dual-phase field number 4 offers the potential to synthesize hard and tough coatings. All other zones in the phase diagram contain at least one soft phase (hexagonal-BN or Ti). TiB_2 crystallizes in *hcp* AlB_2 -structure and exhibits a high hardness from the direct B-B bonds (see section 3.2.1) [120,121]. It has to be mentioned that the schematic phase diagram does not consider the influence of TiB on the phase diagram, like the TiB-Ti(N,B)_{1-x} dual phase field which has been reported by Nowotny et al. [122]. No ternary compounds appear within the Ti-B-N system. TiN and TiB_2 form a quasibinary eutectic system with small solubility of TiB_2 in TiN and negligible solubility of the nitride in TiB_2 [123].

Although the deposition of Ti-B-N coatings by thermal CVD is well-established for cutting tools [124,125], only little results have been published. The coatings are synthesized using gas mixtures of TiCl_4 , H_2 , N_2 , and BCl_3 . Petavy et al. [126,127] describe the formation of Ti-B-N coatings within a temperature range of 1050 to

1500°C. At low BCl_3 concentrations, a *fcc* ternary compound forms with a lattice parameter significantly higher than TiN. Additional phases form at higher BCl_3 additions: above 1250°C TiB_2 develops and below a hexagonal phase appears with lattice parameters slightly distinct from TiB_2 which has been entitled as $\text{TiB}_{2\pm x}\text{N}_y$.

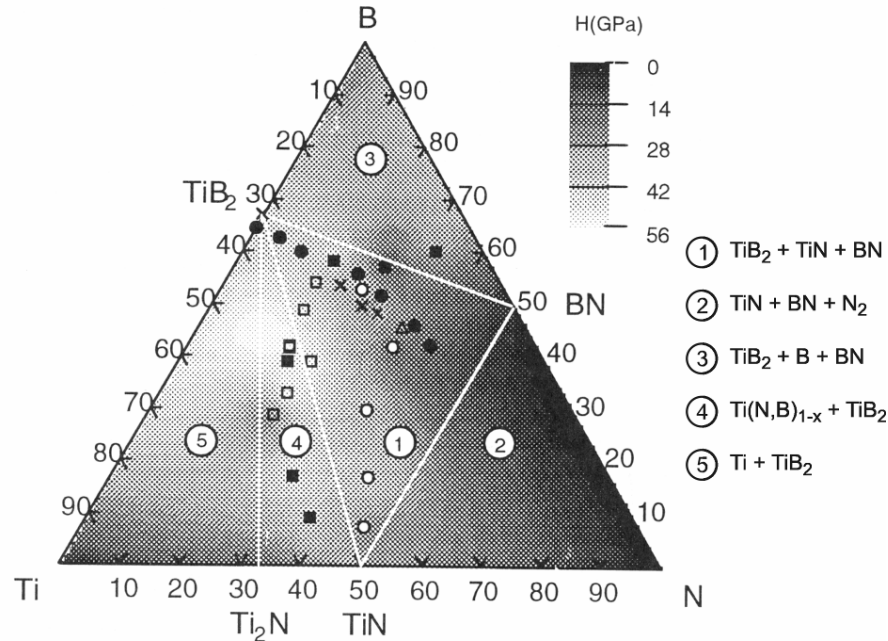


Fig. 18: Hardness distribution within the Ti–B–N system [120].

However, temperatures above 1050°C are not applicable to cemented carbide tools because degeneration of the WC/Co substrate, especially boron diffusion causes the formation of brittle borides in the substrate (see also section 3.2.3). Investigations by Holzschuh [60,128] at lower temperatures (850 – 1000°C) exhibit the formation of TiN/TiB₂ dual-phase structures. The coatings are characterized by a fine morphology and high hardness.

The influence of deposition temperature and gas composition on the structural evolution and, consequently the mechanical and tribological properties of Ti–B–N coating is shown in Publication III.

3.6 Ti–Al–N

The important region within the ternary system Ti–Al–N for the deposition of wear resistant coatings is the quasi-binary system TiN–AlN. AlN crystallizes in *hcp* wurtzite-type structure. While *fcc*–TiN belongs to the metallic hard materials, *hcp*–AlN can be assigned to the covalent hard materials (see Fig. 11). The hardness of AlN (1230 HV) is significantly lower compared to TiN (2100 HV) [48]. The calculated concentration section TiN–AlN is shown in Fig. 19a. In thermodynamic equilibrium, the maximum solubility of AlN in TiN is about 5 mol.% at 2750°C, whereas the solubility of TiN in AlN

is negligibly small. As described in the section 'Metastable Coatings' in chapter 3.2.1, metastable coating structures can be obtained by different deposition techniques. Due to the direct condensation from the vapor phase and limited diffusion, the atoms can remain in an intermixed supersaturated state. The schematic phase field for PVD deposits is schematically illustrated in Fig. 19b for the systems TiN–AlN as well as ZrN–AlN and HfN–AlN. The diagram shows a wide range of *fcc* structure formation, while at high AlN concentrations a *hcp* structure appears. Amorphous deposits can be observed at low temperatures, while the stable *fcc*- and *hcp*-configurations form at high temperatures [47,72,75].

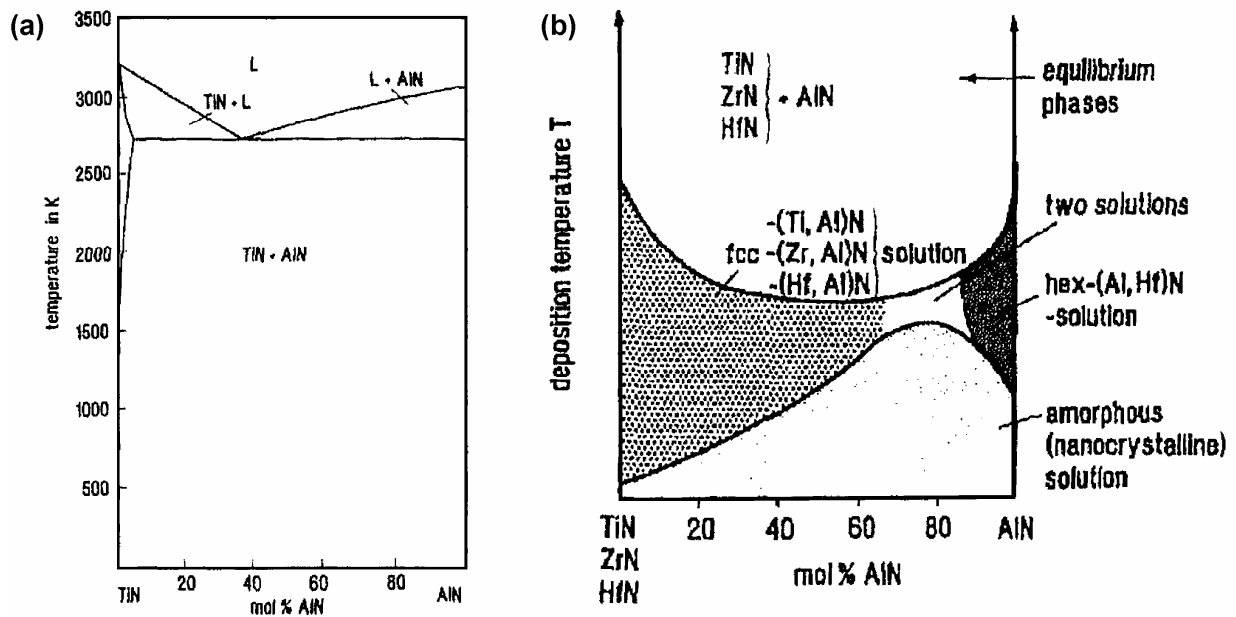


Fig. 19: (a) calculated quasibinary section TiN–AlN, (b) schematic PVD phase fields for TiN–AlN (ZrN–AlN; HfN–AlN) [72].

The crystal structures of TiN and metastable *fcc*-Ti_{1-x}Al_xN are shown in Fig. 20a and b, respectively. Ti atoms of the TiN lattice are partially replaced by smaller Al atoms. The incorporation of Al can be also noticed by a reduced lattice parameter of the cubic structure. The stability of the *fcc* structure depends on the Al content in the lattice as well as the distribution of the Al atoms in the lattice. The transition between the NaCl- and wurtzite-structure occurs at an AlN mole fraction of ~0.70 [129,130].

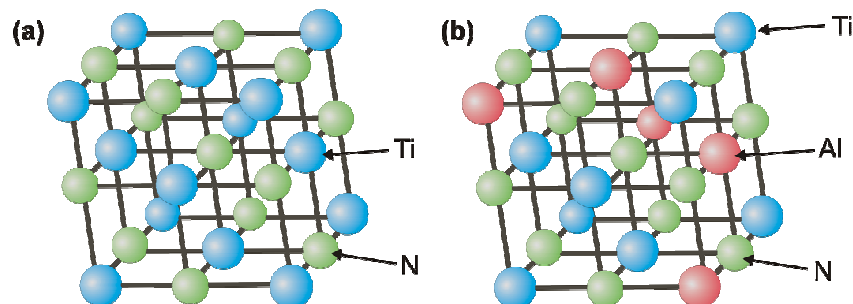


Fig. 20: *fcc* crystal structure of (a) TiN and (b) *fcc*-Ti_{1-x}Al_xN (according to [129]).

The incorporated Al in TiN provides an enhanced hardness and hot-hardness (section 3.2.1) as well as an improved oxidation stability (section 3.2.2).

The deposition of metastable $fcc\text{-Ti}_{1-x}\text{Al}_x\text{N}$ is favored by plasma-assisted techniques and well-established in deposition industry; nevertheless, thermal CVD has proven to enable metastable coatings as well [9,131]. The incorporation of Al into the TiN lattice using TiCl_4 , AlCl_3 , N_2 , and H_2 is thermodynamically not feasible. The replacement of the nitrogen source N_2 by NH_3 enables the deposition of metastable coatings. Using these precursors, single-phase $fcc\text{-Ti}_{1-x}\text{Al}_x\text{N}$ coatings with x up to 0.90 have been synthesized at 700 – 900°C in a laboratory scale unit. The high temperatures reduce the chlorine contents below 1 at.% [131]. A different study uses metal halides from in-situ chlorination of a $\text{Ti}_{0.5}\text{Al}_{0.5}$ alloy with Cl_2 together with NH_3 and H_2 at deposition temperatures of 700°C. Single-phase $fcc\text{-Ti}_{1-x}\text{Al}_x\text{N}$ films have been obtained up to $x \sim 0.40$. The incorporation of Cl impurities varies between 1 at.% for Ti-rich films to 12 at.% for Al-rich coatings [9,78]. The deposition of metastable coatings is not only limited to metal chloride precursors. Utilization of the organometallic precursors tetrakis dimethylamido titanium $\text{Ti}(\text{N}(\text{CH}_3)_2)_4$, hexakis dimethylamido dialuminum $\text{Al}_2(\text{N}(\text{CH}_3)_2)_6$ and NH_3 enable the deposition of cubic films between 300 and 450°C with Al contents up to $x = 0.40$. The coatings exhibit a nanocrystalline structure with crystal sizes of approximately 5 nm. The application of organometallic precursors avoids the incorporation of Cl, but at the expense of C-contamination up to 8 at.% [77,132].

Publication IV focuses on the feasibility to deposit $fcc\text{-Ti}_{1-x}\text{Al}_x\text{N}$ films using customary metal chloride precursors, i.e. TiCl_4 and AlCl_3 , in an industrial thermal CVD unit.

4 Tribology of Coatings

4.1 General Aspects of Tribology

Tribology considers the phenomena that occur between interacting surfaces in relative motion, and embraces the science of friction, wear, and lubrication. In many cases, low friction values are favorable and a reduction of the friction force reduces the energy dissipation in mechanical parts of machines, and therefore increases the efficiency of these devices. Wear is the progressive loss of material during the relative motion of two surfaces. The resultant damage of one or both surfaces necessitates the premature replacement of components and causes vast expenses. The purpose of research in tribology is the minimization of losses from friction and wear at all technological levels. The application of surface layers enables the equipment of components with specific tribological properties, such as reduced friction, high wear resistance, or even both. While the surface layer carries the tribological functions, the bulk material can be selected according to different criteria, like stiffness, strength, or costs. Hence, the application of coatings on tools and machine elements is a very efficient approach to improve the lifetime and productivity of components [133-135].

The tribological processes during the contact of surfaces in relative motion are very complex and can be described with certain input and output parameters. The geometry of the contact on macro and micro scale, the chemical composition and microstructure of the materials as well as the environment conditions are crucial input data. The tribological contact causes physical and chemical changes and results in energy related output data, such as friction, wear or temperature. Certain mechanisms act at the same time at different scale levels and have to be considered to describe the tribological contact. The processes can be differentiated into five types as shown in Fig. 21 [136,137]:

- *macromechanical changes* consider the stresses and strains in the contact zone, the elastic and plastic deformations and the formation and dynamics of wear particles
- *micromechanical changes* embrace the formation of stresses and strains at asperity level, the crack formation and propagation, material liberation and particle formation
- *tribochemical changes* by chemical reactions are favored by the high local pressures and temperatures, which alter the chemical composition and mechanical properties of the outermost surface layer
- *material transfer* occurs from liberated wear particles that are re-attached to the surface
- *nanophysical changes* are examined to explain friction and wear related phenomena on the molecular scale

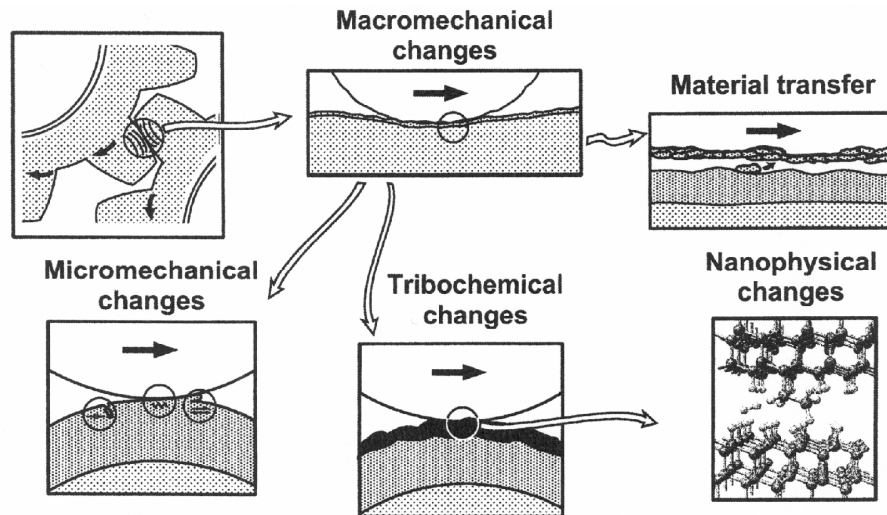


Fig. 21: Schematic representation of the tribological contact mechanisms [136].

4.2 Friction

Friction is defined as the tangential force required to move a body over a stationary counterface. The friction coefficient μ is the ratio between the tangential force F_t and the normal load F_n [133]:

$$\mu = \frac{F_t}{F_n} \quad (4.1)$$

The friction coefficient is not an inherent material property, but is dependent on various parameters, e.g. the sliding distance, sliding velocity, normal load, or the environment. Three different components contribute to the friction coefficient (see Fig. 22). The adhesion of flat portions during sliding as well as the formation and breaking of microwelded junctions cause a resistance against motion and contribute by a value μ_a . A second component μ_p results from the ploughing of hard asperities or particles in a softer material. Furthermore, the plastic deformation of asperities increases the tangential resistance and the friction coefficient by μ_d . The measured friction coefficient μ in sliding experiments is the sum of μ_a , μ_p and μ_d . The contribution of the individual components is not constant and changes with time. At the beginning of the sliding contact, adhesion may play a minor role, since surface contaminations, e.g. oxide layers, separate the two friction partner. Within this stage, the friction coefficient is largely independent of the material combination, but determined by ploughing effects and the deformation of asperities. The wear process by ploughing removes the oxide layer and adhesion may become important and causes an enhanced friction coefficient. Several different stages may pass through until a stable friction value has been reached. The contribution of each basic mechanism will depend on the interface, the material pairing, preparation of the surface, the environment, and the operating conditions [137-139].

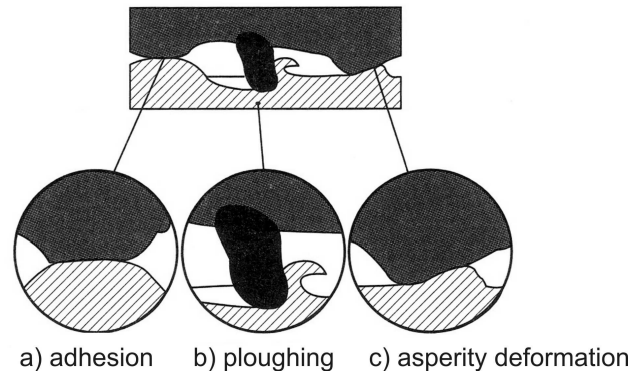


Fig. 22: The components of sliding friction: (a) adhesion, (b) ploughing and (c) asperity deformation [137].

The application of coatings on components can change the frictional behavior drastically. One of the most important parameters influencing the behavior of coated parts is the relationship between coating and substrate hardness. In the following, two different cases will be considered: the application of *soft* and *hard* coatings. The friction force is ideally the product between the shear strength and the contact area. Thus, favorable for low friction coefficients are films of low shear strength and small contact areas. Soft films provide a low shear strength, but the contact area and the ploughing component μ_p can be large because of the low load-carrying capacity (Fig. 23a). The friction coefficient changes with the film thickness and increases above an optimum value. Hard coatings can reduce the contact area by decreasing the ploughing component (Fig. 23b), but hard materials also show a higher shear strength. Thus, the influence on the friction value is small. The combination of both a hard coating and a thin soft film at the top is advantageous for many tribological applications. The hard coating provides the load support, reduces ploughing and shear occurs in the soft film (Fig. 23c) [137].

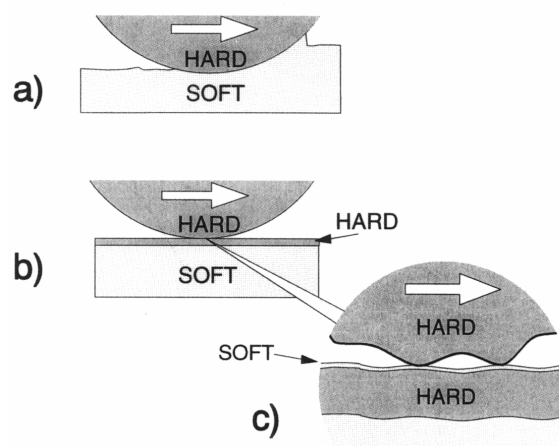


Fig. 23: Schematic illustration of a hard slider moving over an (a) soft counterface, (b) hard coating on a soft substrate, and (c) a hard coating with a soft microfilm at the top [137].

Hard coatings, like TiN, CrN, Al₂O₃, or *fcc*-Ti_{1-x}Al_xN reduce the ploughing component and improve the wear resistance of components, but exhibit high friction values, typically between 0.4 and 0.9 in dry sliding [134,140]. The friction coefficient can be reduced by the application of solid lubricants, like MoS₂, graphite, hexagonal (*h*)-BN, or soft metals (e.g., Ag or Pb) below 0.2. The low friction properties of MoS₂, graphite and *h*-BN result from their lamellar crystal structure, whereas lubricating metals have multiple slip planes and do not strain harden appreciable. The formation of lubricating films may also occur in-situ from tribochemical reactions. Usually, these ‘microfilms’ arise from reactions of the coating with oxygen or humidity of the surrounding environment [136,141]. Chlorine induced oxidation of TiN forms easy-shearable titanium oxides and reduces the friction coefficient from about 0.8 to 0.2 at room temperature, for instance [142]. Lubricious films are not limited to oxides, also transfer films of carbon are known to reduce friction, such as in diamond-like carbon (DLC) coatings [143]. The formation of a lubricious layer of carbon has also shown to reduce the friction coefficient of TiC_xN_{1-x} coatings (see Publication II). Fig. 24 exhibits the friction curves of two TiC_xN_{1-x} coatings tested against Al₂O₃ at 500°C together with Raman spectra recorded in the wear track. The friction coefficient of coating TiC_{0.71}N_{0.29} ($\mu = 0.26$) is significantly lower compared to TiC_{0.39}N_{0.61} ($\mu = 0.66$). Intense oxidation of TiC_{0.71}N_{0.29} releases a high amount of amorphous carbon as can be seen from the D- and G-bands in the Raman spectra. The carbon film in the wear track acts as a lubricant and lowers the friction coefficient.

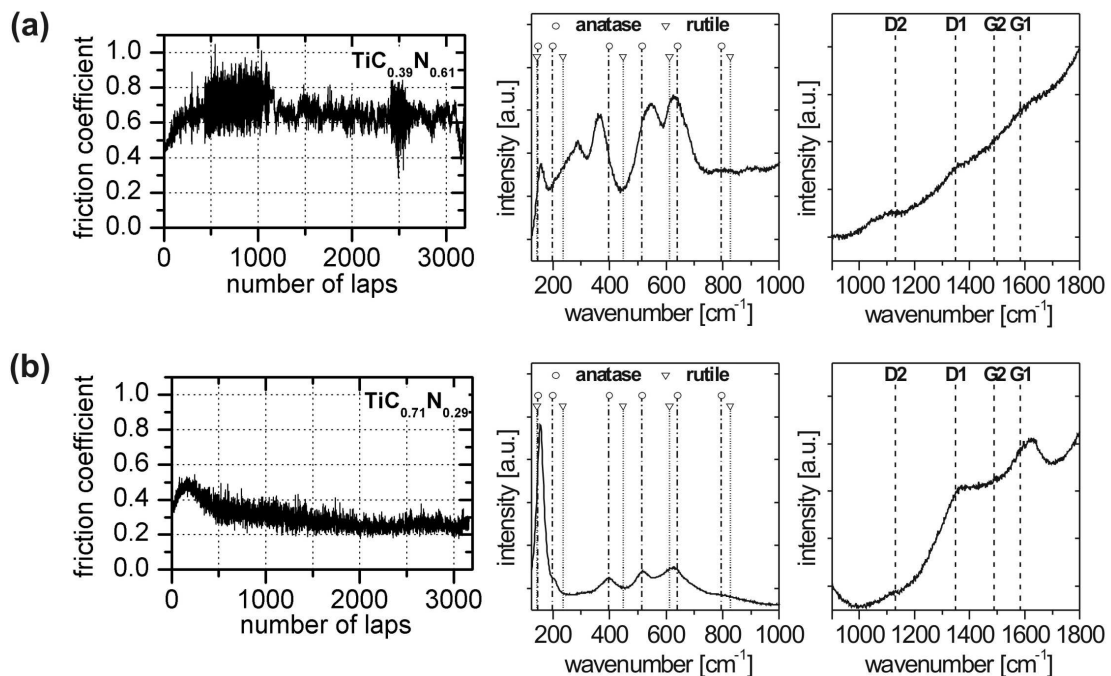


Fig. 24: Friction curves and Raman spectra of the wear track of (a) TiC_{0.39}N_{0.61} and (b) TiC_{0.71}N_{0.29} coatings tested against Al₂O₃ at 500°C (according to Paper II).

4.3 Wear

Wear is the removal of material from solid surfaces as a result of two interacting bodies in relative motion. Both friction and wear originate from the same tribological processes and a correlation can be often observed, where low friction corresponds to low wear and high friction to high wear. Nevertheless, there is no general relationship between friction and wear. For design and material development purposes, it is necessary to describe the severity of wear. The wear rate k_w , also referred to as dimensional wear coefficient, provides a valuable means to quantify wear processes and is defined as [133,137]:

$$k_w = \frac{V}{F_n s} \quad (4.2)$$

where V is the worn volume, F_n the normal load, and s the sliding distance. The wear rate represents the worn volume per unit distance and normal load.

The wear of materials can be classified into four basic mechanisms: adhesive wear, abrasive wear, fatigue wear, and chemical wear as shown in Fig. 25 [137,140].

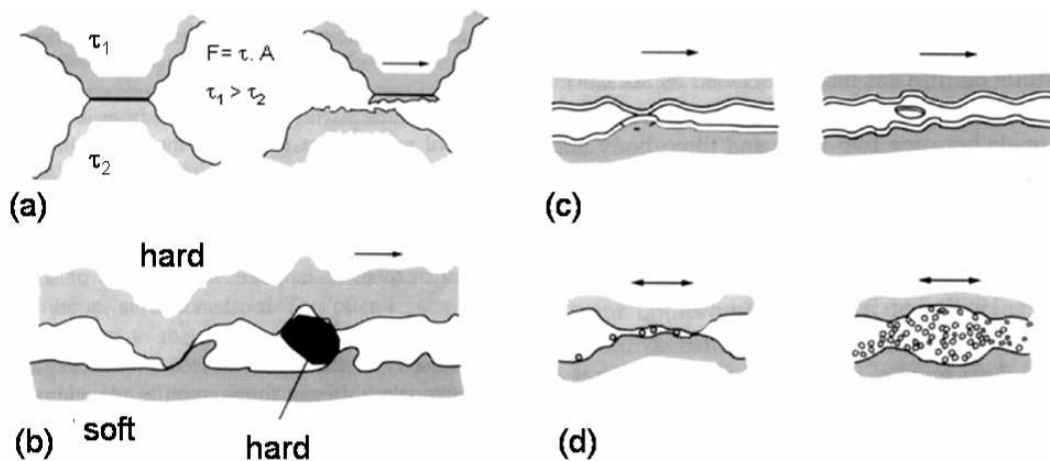


Fig. 25: The basic wear mechanisms (a) adhesive, (b) abrasive, (c) fatigue, and (d) chemical wear [137].

Adhesive wear occurs during sliding, when high local pressures between contacting asperities cause plastic deformation, adhesion, and the formation of local junctions. Further movement of the bodies results in the breaking of the junctions at the former interface or results in the transfer of material. The site of the fracture depends on the strength of the junctions and the materials in contact (see Fig. 25a) [139,144].

Abrasive wear takes place when asperities of a hard surface or hard particles between the surfaces cause plastic deformation or fracture (Fig. 25b). Abrasive wear can be divided into two-body abrasion and three-body abrasion. In two-body wear, the asperities of a hard surface plough the softer counterbody and cause material removal. Three-body wear occurs when hard particles are trapped between the sliding surfaces causing abrasion of either one or both of the surfaces in contact. For ductile materials,

the hard asperities cause plastic flow of the softer material and scratches in sliding direction can be observed. Wear by plastic flow can occur by several deformation modes: ploughing, wedge formation and cutting as shown schematically in Fig. 26. During ploughing, material is displaced from a groove to the sides without material removal (Fig. 26a). Nevertheless, wear can occur by fatigue after the surface has been ploughed several times. In the wedge formation type of wear, only some of the material is displaced to the sides, while the remaining material piles up in front of the scratching particle (Fig. 26b). The cutting type of wear causes significant removal of material in the form of discontinuous or ribbon-shaped debris particles (Fig. 26c). Only a minor part of material is removed to the sides. Although hard ceramic materials show only limited plastic flow, abrasive wear by plastic deformation can be also observed [137,139,144].

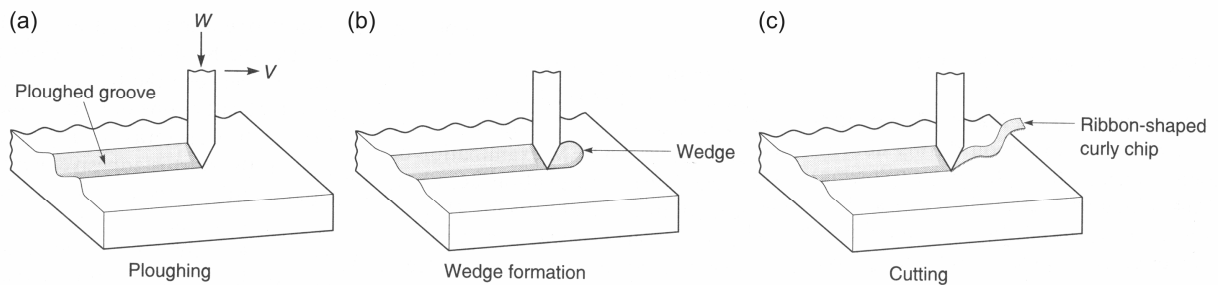


Fig. 26: Abrasive wear processes due to plastic deformation [139]

As the feasibility for plastic flow decreases, brittle fracture and wear by lateral cracking becomes the dominating wear mechanism. The hardness H (resistance to deformation) and the fracture toughness K_c (resistance to fracture) are the decisive material values. The wear volume v_w per unit sliding distance is given by

$$v_w \propto \frac{(E/H)F_n^{9/8}}{K_c^{1/2} H^{5/8}} \quad (4.3)$$

with the elastic modulus E and the applied load F_n . The ratio (E/H) does not vary to a great extent between different hard brittle solids. From equation 3.2 follows that the wear resistance of ceramics can be improved by enhancing both the fracture toughness and the hardness. Furthermore, the wear volume increases with $F_n^{9/8}$, i.e. wear due to fracture increases more than linear with the applied load [133,139]. The influence of the hardness can be seen in Fig. 27 on backscatter SEM images of wear tracks after dry sliding tests of Ti–N–B coatings. An increasing boron concentration enhances the coating hardness from 20 GPa for TiN (Fig. 27a) to 27 GPa at 0.3 at.% boron (Fig. 27b), and 45 GPa for 35.1 at.% boron (Fig. 27c). While the wear appearance of TiN exhibits deep grooves by plastic deformation, the higher hardness at 0.3 at.% B reduces the penetration depth of abrasive particles. Thus, the scratches diminish in Fig. 27b, but a crack network arises and the coating suffers from brittle fracture. Plastic deformation is

negligible for the hardest coating and only wear by brittle fracture can be observed (Fig. 27c).

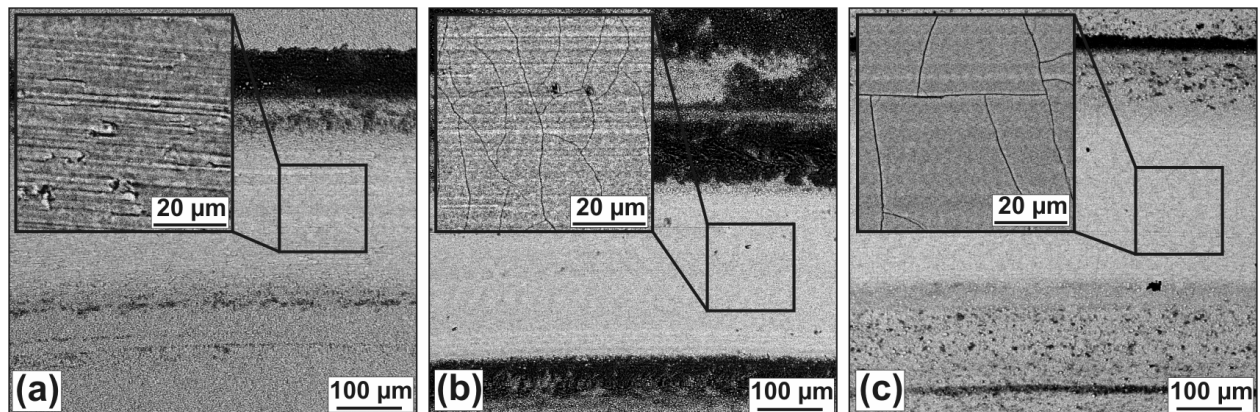


Fig. 27: Backscatter SEM micrographs of the wear tracks of Ti–N–B coatings after ball-on-disc tests at 25°C containing (a) 0 at.%, (b) 0.3 at.% B, and (c) 35.1 at.% B (Paper III).

Fatigue wear occurs from surface and subsurface cracks induced by repeated loading and unloading cycles. The fatigue cracks cause the breakup of the surface and formation of large pits in the surface. In contrast to adhesive or abrasive wear, negligible wear takes place up to this point. However, the liberated surface material between the sliding materials can be the onset of abrasive wear (cf. Fig. 25c) [139,144].

Chemical wear embraces the chemical reaction of the rubbing surfaces with the liquid or gaseous environment (Fig. 25d). The wear process originates from the continuous formation and removal of the resultant reaction layer. From this follows that chemical wear depends ultimately on the kinetics of the layer formation and the properties of the reaction layer, e.g. strength, ductility and adhesion to the substrate. The kinetics of chemical reactions is highly modified by the contact processes between sliding bodies and reactions, which usually occur at high temperatures, take place at lower temperatures. Especially, the frictional heat produced at contacting asperities contributes to an increased reaction rate, since the interface temperature in the contact zone can reach several hundred degrees. The most common chemical wear process at ambient air is oxidational wear from the reaction with oxygen and/or humidity. Non-oxide ceramics, such as TiN are well-known to form oxide films in an oxidizing environment. For example, the dark regions beside the wear tracks in the backscatter SEM images of Fig. 27 are oxidized coating material. It is important to mention that the formation of a reaction layer can also act as protection against wear [145,146].

5 Experimental

5.1 Coating Deposition

The coatings investigated within this work were deposited in an industrial thermal CVD unit at CERATIZIT. A picture of a thermal CVD equipment is exhibited in Fig. 28. The picture shows the CVD plant at the end of the deposition process with the glowing reactor and the lifted heating chamber. Inside this chamber, circular trays are stacked one upon the other, where each tray is batched with specimens or cutting inserts. Although only a small fraction of the batch capacity was used for samples for detailed investigations, each tray was loaded with dummy material of cutting inserts to provide gas flow conditions comparable to production conditions and avoid unbalanced flow patterns along the reactor height.

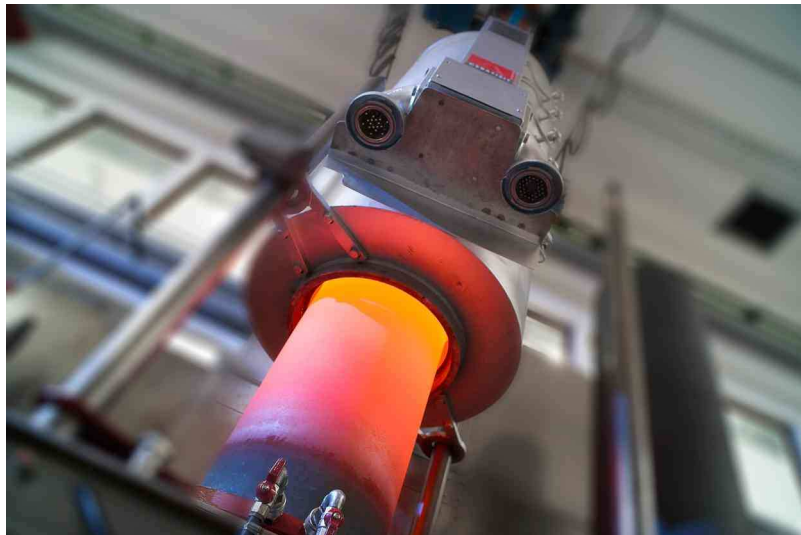


Fig. 28: Picture of the employed CVD equipment (from CERATIZIT Austria GmbH).

Two different types and numbers of deposition trays were used depending on the coating system. TiN, $\text{TiC}_x\text{N}_{1-x}$, and Ti–N–B were deposited with trays used in production. Experiments with NH_3 to deposit Ti–Al–N coatings were performed with smaller and less deposition trays. However, the sample position within each testing series was constant for the sake of comparison.

Deposition experiments comprise the following steps:

- *cleaning* of the specimens in a set of aqueous cleaning and rinsing solutions followed by drying in hot air.
- *loading* of the deposition trays with specimens at a constant position throughout every deposition series.

- *heating* of the entire reactor up to the set temperature in a gas stream of H₂ to remove residual organic contaminations and reduce oxide layers on the sample surface.
- *coating deposition* of the intended coating material. An interlayer of 0.5 μm TiN was deposited prior TiC_xN_{1-x} and Ti–N–B films to avoid influences from the substrate on the coating and vice versa. To obtain comparable growth conditions for the subsequent coating, the TiN layer was deposited at constant reaction conditions, i.e. constant gas flows and a temperature of 900°C. The deposition temperature of the subsequent coating was achieved by an intermediate heating/cooling step in H₂ atmosphere to avoid coating oxidation.
- *rinsing* of the reactor with Ar to remove residual deposition gases.
- *cooling down* of the reactor in Ar atmosphere.

5.2 Coating Characterization

5.2.1 General

The coatings were investigated and characterized with respect to their chemical composition and microstructure as well as mechanical and tribological properties. Different experimental techniques were used to assess these coating properties:

- *light optical microscopy (LOM)*: measurement of the coating thickness and wear track investigation after ball-on-disc tests [147].
- *scanning electron microscopy (SEM)*: investigation of the surface- and coating morphology, microstructural changes after oxidation, and wear track examinations [148].
- *glow discharge optical emission spectroscopy (GDOES)*: determination of the chemical composition of as-deposited coatings and subsequent to high-temperature ball-on-disc tests to assess the degree of oxidation [149].
- *X-ray diffraction (XRD) analysis*: evaluation of the crystalline structure and phase composition in Bragg-Brentano geometry and glancing-angle XRD (GAXRD) configuration; stress measurements were performed using the $\sin^2\psi$ -method [150-152].
- *ball-on-disc tests*: investigation of the tribological behavior (friction & wear) by dry sliding experiments between 25 and 600°C [153].
- *optical white light profilometry*: measurement of the surface roughness and the worn volume after ball-on-disc tests [154].
- *microhardness tests*: evaluation of the coating hardness from the load – penetration curves [155,156].

- *Raman spectroscopy*: investigation of changes in phase composition in the wear track after dry-sliding tests [157].
- *grazing incidence reflection-Fourier transform infrared (GIR-FTIR) spectroscopy*: chemical analysis of the wear track complementary to Raman investigations [158].

Most techniques used within this work are common techniques and are well-documented. In the following, Raman spectroscopy and GIR-FTIR spectroscopy are explained in detail. Both techniques measure the vibrational spectra of materials, but the physical processes are different. Raman- and IR-spectroscopy can be considered to be complementary.

5.2.2 Raman Spectroscopy

The Raman effect was discovered in 1928 by Krishna and Raman [159] and arises from an interaction of light with the optical and vibrational oscillations of molecules. Besides the absorption of light, a small fraction of the incident photons will be scattered either with the same frequency (Rayleigh scattering) or a different, but materials specific frequency (Raman scattering). The frequency can be higher or lower depending onto whether the molecule is in an excited vibrational state or not. The processes that excite or annihilate molecular and crystal vibrations are called Stokes- and anti-Stokes-scattering, respectively. Both are symmetrically positioned about the Rayleigh scattering, but of different intensities. Anti-Stokes scattering depends on the existence of thermally excited vibrations and, thus, yields a very weak intensity. It is common in Raman spectroscopy to illustrate the difference between the frequency of the Rayleigh- and the Stokes-scattering, the so-called Raman shift as a function of the wavenumber in reciprocal centimeters [157,160].

Raman spectroscopy is an excellent technique to determine the structure of materials, since it is sensitive to the details of atomic arrangements, the length, strength, and arrangement of bonds. The spectra are characteristic like fingerprints and can be used for the identification of materials. The Raman shift depends on the crystallinity, the defects and structural disorder, but also on the stresses in materials. The information depth depends on the transparency of the material to the laser radiation and can range from a few microns to several tenths of millimeter. Raman microscopy – the combination of Raman spectroscopy with optical microscope enables structural investigations with a lateral resolution of a few microns [157,160].

All these facts give rise to the utilization of Raman spectroscopy to characterize hard coatings, especially to determine localized changes in structure, e.g. small wear particles. Within this work, Raman microscopy was applied to identify the wear debris and reaction products after dry-sliding experiments, but also the oxides at the surface after tests at elevated temperatures in air (see Publication II and III). The relevance of

oxides on the oxidation kinetics of coatings has been outlined in section 3.2.2. The oxidation of Ti-based hard coatings, e.g. $\text{TiC}_x\text{N}_{1-x}$ causes the formation of different titanium oxides. The Ti–O system consists of several metastable and stable phases with a variety of crystal structures (see for example Ref. [161]). TiO_2 is the most important oxide and crystallizes in three different polymorphic structures: rutile (tetragonal; $P4_2/mnm$), anatase (tetragonal; $I4_1/amd$) and, less relevant in practice brookite (rhombohedral; $Pbca$). Rutile is the thermodynamically stable polymorph; however, anatase can be found frequently since the difference in lattice energy is only 0.5 %. Both anatase and rutile are built-up of an octahedral configuration, where one titanium ion is surrounded by six oxygen ions and the structural differences arise from the dissimilar connection of the octahedrons [162,163]. The different oxides can be easily distinguished by Raman spectroscopy. Furthermore, quantitative information can be gained from the band intensities, whereas the band position provides information about the stoichiometry [164-166]. Fig. 29 shows the Raman spectra of TiN and $\text{TiC}_{0.71}\text{N}_{0.29}$ coatings oxidized at ambient air for 2 hours. While TiN has transformed to a large extent into rutile, the $\text{TiC}_{0.71}\text{N}_{0.29}$ coating only yields the bands of anatase. The results suggest that carbon in $\text{TiC}_x\text{N}_{1-x}$ stabilizes the anatase structure. The unit cells of anatase and rutile are illustrated in Fig. 29a and b, respectively according to the predominating oxide.

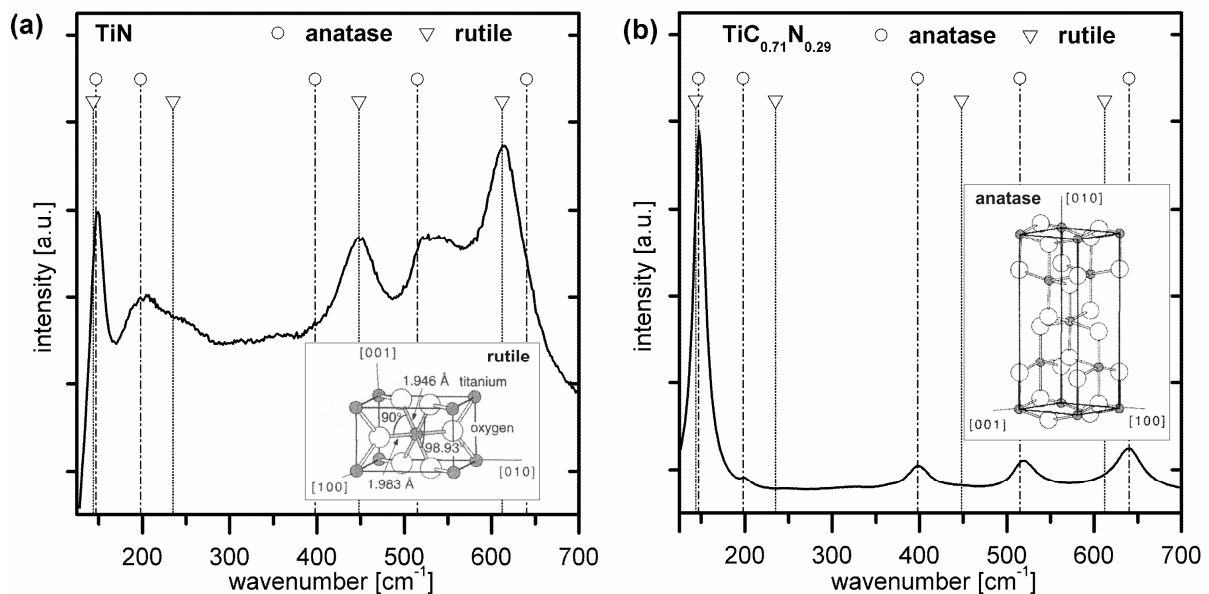


Fig. 29: Raman spectra of (a) TiN and (b) $\text{TiC}_{0.71}\text{N}_{0.29}$ coatings oxidized at 500°C for 2 h. The inserts illustrate the tetragonal unit cells of rutile and anatase [162].

Besides inorganic crystalline structures, Raman spectroscopy enables the determination of carbon and its detailed bonding structure, for instance. Carbon forms a variety of crystalline and disordered structures due to its ability to exist in three different hybridizations: sp^3 , sp^2 , and sp^1 . Diamond and graphite are well-known modifications with sp^3 and sp^2 configuration, respectively. But in addition, several amorphous carbon

(a-C) types with disordered graphitic structure exist of varying sp^2 and sp^3 fraction. The differences between these structures can be analyzed by Raman spectroscopy. Diamond has a single active mode at 1332 cm^{-1} , while the Raman mode of single crystal graphite is at 1580 cm^{-1} labeled as 'G' for 'graphite'. With decreasing crystal size of graphite, a second peak arises at around 1350 cm^{-1} which is referred to as 'D-peak' for 'disorder'. Frequently, the Raman spectra of a-C show additional peaks due to the disorder structure and the spectra can be deconvoluted into four separate peaks. The G-peak is split into G_1 ($1586 - 1610\text{ cm}^{-1}$) and G_2 ($1510 - 1570\text{ cm}^{-1}$). G_1 is assigned to the original G-peak from undisturbed graphite, whereas G_2 results from highly distorted graphite clusters. Similarly, the D-peak is separated into D_1 ($1340 - 1415\text{ cm}^{-1}$) and D_2 ($1150 - 1210\text{ cm}^{-1}$), where both peaks are caused by disorder induced effects. The intensity ratio of the D- and G-modes $I_D/I_G = (I_{D1}+I_{D2})/(I_{G1}+I_{G2})$ provides information about the degree of disorder and is proportional to the sp^2 fraction [167-169]. Raman spectra of amorphous carbon are shown in Fig. 30. The spectra were recorded from wear particles of $\text{TiC}_{0.14}\text{N}_{0.86}$ (Fig. 30a) and $\text{TiC}_{0.71}\text{N}_{0.29}$ (Fig. 30b) coatings worn against Al_2O_3 at room temperature (see Publication II). Low friction values down to 0.15 could be ascribed to the formation of a continuous layer of amorphous carbon. Moreover, the friction coefficient correlated with the amount of disorder, such as that low friction values were accompanied by high I_D/I_G ratios.

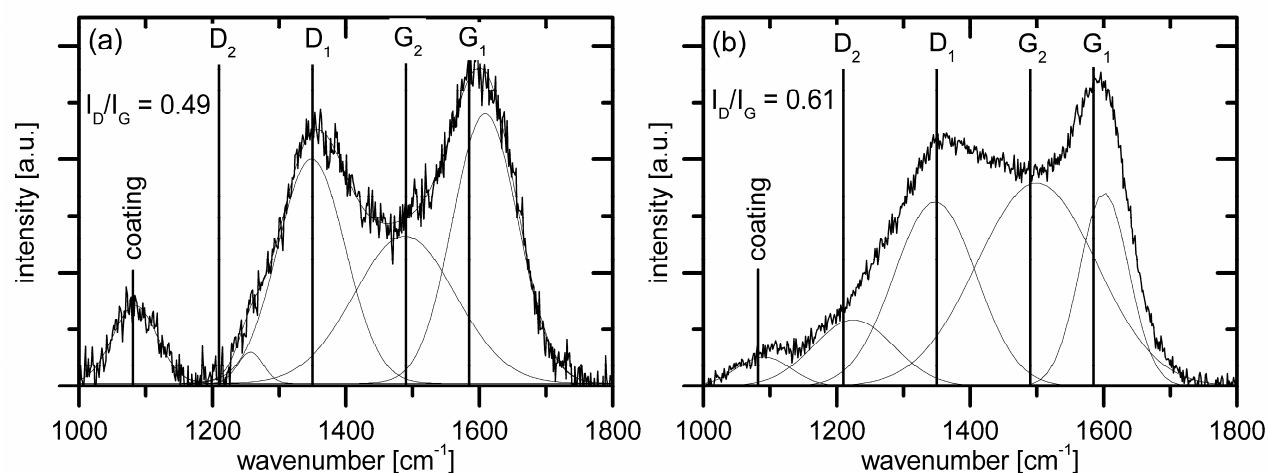


Fig. 30: Raman spectra from the wear track of (a) $\text{TiC}_{0.14}\text{N}_{0.86}$ and (b) $\text{TiC}_{0.71}\text{N}_{0.29}$ coatings. The peak deconvolution shown was used to derive the I_D/I_G ratios in Publication II.

Low friction values ($\mu = 0.26$) have been also observed in Ti-N-B coatings containing 35 at.% B (Publication III). Attempts to detect reaction layers, like $h\text{-BN}$ or H_3BO_3 by Raman spectroscopy were performed; however, no indication for the formation of these compounds could be found. The wear tracks were investigated by GIR-FTIR-spectroscopy to detect possibly formed reaction films.

5.2.3 GIR-FTIR Spectroscopy

IR spectroscopy measures, similar to Raman spectroscopy, the vibrational spectra of materials. It is also a non-destructive technique and provides information about the chemical bonding. However, the physical process behind are different and other vibrational modes can be excited. After the interaction of polychromatic infrared light with the sample, the intensity is measured as a function of the wavelength. The wavelengths at which absorption occur are characteristic; they represent the excitation of vibrations and are characteristic for the type of bond and the group of atoms involved in the vibration. Measured IR spectra typically show the absorbance as a function of the wavenumber. The designation Fourier transform infrared (FTIR) spectra denotes the type of spectrometer, where the measurement signal is subjected to a Fourier transform [158].

The sensitivity of IR spectroscopy depends highly on the chemical bond of interest. Generally, the sensitivity of FTIR is one order of magnitude higher compared to Raman spectroscopy, since the cross-section for Raman scattering is very small. Specimens non-transparent to IR radiation have to be measured in reflectance geometry, where the surface sensitivity can be enhanced using grazing incidence reflection Fourier transform infrared (GIR-FTIR) spectroscopy [158].

GIR-FTIR spectroscopy was used in Publication III to explain the observed low friction coefficient at 35 at.% B. The formation of a reaction layer of *h*-BN or H₃BO₃ was suspected to reduce the friction coefficient. Both compounds are IR-active and can be detected by FTIR spectroscopy [170,171]. No indication for either of these compounds was found.

6 Summary and Conclusions

Thermal CVD TiN coatings are well-established in cutting tool industry due to a balanced combination of hardness, oxidation resistance and adhesion. However, the diversity of cutting operations requires coatings of tailored properties, like materials of superior oxidation resistance or low friction coefficients, for instance. In this work, the coating properties of TiN were examined and, moreover, systematically altered by the addition of C, B, or Al to form either single-phase $\text{TiC}_x\text{N}_{1-x}$ ($0 \leq x \leq 1$) coatings, dual-phase coatings within the ternary system Ti–N–B, or metastable coatings in the Ti–Al–N system.

The coatings were deposited in an industrial thermal CVD unit and their properties were modified by changing the deposition temperature and the concentration of reactive precursors. Two different precursor systems were used depending on the added element. Besides TiN, $\text{TiC}_x\text{N}_{1-x}$ and Ti–N–B coatings were deposited from the system $\text{TiCl}_4\text{--N}_2\text{--H}_2\text{--Ar}$ by the addition of CH_4 and BCl_3 , respectively. Since the incorporation of Al into TiN is thermodynamically not feasible using this system together with AlCl_3 , the more reactive system $\text{TiCl}_4\text{--NH}_3\text{--Ar}$ was employed to produce Ti–Al–N coatings. The temperature was adjusted according to the reactivity of the precursor system to avoid gas phase nucleation and to enable homogeneous coatings. While 850 to 1050°C were used for TiN, $\text{TiC}_x\text{N}_{1-x}$ and Ti–N–B coatings, the temperature was set between 550 and 700°C for Ti–Al–N deposition. The influence of the process conditions on the structural, mechanical and tribological behavior of these coatings was examined.

The high impact of the deposition temperature on the final coating properties was shown for coatings of pure TiN. Highly textured films of (211) orientation form at low temperatures (850 – 900°C). This texture is also reflected by fine lenticular-like and pyramidal surface morphologies, respectively. With increasing temperature, the coating texture diminishes and more or less irregular faceted crystals develop. The coating hardness increases from 18 GPa for the (211) textured films to 20.5 GPa for those without preferred orientation. Nevertheless, the softer and textured coatings exhibit a wear resistance twice as good compared to the non-textured films under dry sliding conditions at room temperature. The fine-grained structure provides a higher toughness and, thus an enhanced wear resistance. The friction coefficient is high and, depending on the surface roughness between 0.9 and 1.1.

The carbon content in $\text{TiC}_x\text{N}_{1-x}$ coatings rises with the deposition temperature and the CH_4/N_2 ratio in the gas phase. The replacement of nitrogen by carbon atoms in the TiN lattice consequences an hardness increase from 20 to 33 GPa from TiN to $\text{TiC}_{0.71}\text{N}_{0.29}$. The high coating hardness provides excellent wear resistance at 25°C, whereas the

opposite behavior can be observed at elevated temperatures. Extensive oxidation, at 500°C and, especially at high carbon contents deteriorates the wear resistance. Between 500 and 600°C, a change in the oxidation kinetics occurs which reduces the oxidation process, and consequently the wear rate. The origin of this transition is an alteration in the oxide layer composition from mainly anatase at 500°C to rutile at 600°C. The results indicate that carbon stabilizes the anatase structure. Carbon addition to TiN beneficially influences the frictional behavior and reduces the friction coefficient down to 0.15 at 25°C due to the formation of a lubricating amorphous carbon film in the wear track. The presence of carbon decreases the friction coefficient also at higher temperatures.

Ti–N–B coatings were deposited with boron contents up to 35 at.%. The boron content in the films increases remarkably with decreasing temperature. The addition of boron to TiN causes the formation of a dual-phase structure of TiN/TiB₂ above 1 at.% B. The distinct columnar structure of TiN diminishes with increasing boron concentration and fine-grained coatings with smooth surfaces are obtained at the highest contents. Regarding the coating systems investigated within this work, the Ti–N–B coatings exhibit the highest hardness which increases with rising TiB₂ phase fraction up to 45 GPa at 35 at.%. The friction coefficient is in the range of 1.0 below 13 at.%, but decreases down to 0.26 at 35 at.% at 25°C. A lubrication mechanism caused by both moisture and oxygen is supposed to originate this low values, since the friction coefficients are considerable higher (0.6 – 1.0) at 500 and 600°C. The wear resistance exhibits a behavior similar to TiC_xN_{1-x}. While the wear resistance decreases at 500°C with rising B content, it improves at 600°C because the oxide scale changes from predominantly anatase to a dense layer of rutile.

The feasibility to deposit Ti–Al–N coatings in an industrial CVD unit has been successfully demonstrated. High deposition temperatures enhance the complete dissociation of AlCl₃ and raise the Al content with simultaneously decreasing incorporation of the impurities Cl and O. According to XRD analysis, single-phase coatings formed up to 19 at.% Al. However, the constitution of the coatings gives scope for presumptions, especially since the hardness decreases from 20 to 14 GPa and the lattice parameter increases. Despite the fact that this behavior is in contrary to the well-examined PVD coatings, the formation of metastable *fcc*-AlN at 20 at.% Al could result from the decomposition of supersaturated *fcc*-Ti_{1-x}Al_xN. The appearance of *fcc*-AlN enhances the hardness to about 20 GPa. Above 24 at.% Al, considerable amounts of *hcp*-AlN form that deteriorate the mechanical properties.

Although the deposition of TiN by thermal CVD is a mature technique, it has been shown that the mechanical, thermal and, ultimately the tribological properties can be modified over a wide range by the addition of different alloying elements. The properties can be adjusted from super-hard Ti–N–B coatings by a high-phase fraction of TiB₂ to low friction coatings of TiC_xN_{1-x}. It has been proven for the first time that the deposition of metastable Ti–Al–N coatings is feasible by thermal CVD on an industrial scale. The results provide a basis for further developments with regard to commercial *fcc*-Ti_{1-x}Al_xN coatings.

7 Symbols and Abbreviations

7.1 Symbols

Greek Letters

δ	boundary layer thickness
η	viscosity
θ	incident angle of the X-ray beam on the sample
μ	friction coefficient
μ_a	friction coefficient due to adhesion
μ_d	friction coefficient due to asperity deformation
μ_p	friction coefficient due to ploughing
ρ	mass density

Roman, Lower Case Letters

d	grain size
k	material constant in Hall-Petch relation
k_w	wear rate
n	number of considered peaks for the texture coefficient calculation
p	vapor pressure in the bulk gas
p_0	vapor pressure at the surface
s	sliding distance
v	gas flow velocity
v_w	wear volume per unit sliding distance
x	distance

Roman, Capitals Letters

A	pre-exponential factor
D	diffusivity
D_1	disorder induced Raman band of carbon
D_2	disorder induced Raman band of carbon
E	elastic modulus
E_a	activation energy
F_n	normal force
F_t	tangential force
HU_{pl}	universal plastic hardness
H	hardness
H_0	intrinsic hardness

G_1	Raman band of graphite
G_2	Raman band of highly distorted graphite clusters
I_D	sum of the disorder induced Raman signals of carbon
I_{D1}	intensity of Raman band D_1
I_{D2}	intensity of Raman band D_2
I_G	sum of the Raman signals of graphite
I_{G1}	intensity of Raman band G_1
I_{G2}	intensity of Raman band G_2
$I_{(hkl)}$	measured peak intensity of reflection (hkl)
$I_{0,(hkl)}$	peak intensity of reflection (hkl) of powder material according to JCPDS
J	flux through the boundary layer
K	equilibrium constant
K_c	fracture toughness
R	universal gas constant (8.314 J/molK)
R_d	deposition rate
T	absolute temperature
$TC_{(hkl)}$	texture coefficient of the planes of Miller indices (hkl)
T_{dep}	deposition temperature
T_m	melting temperature
T_s	substrate temperature
V	wear volume
ΔG_r^0	standard free energy change of reaction
ΔG_r	free energy of reaction
$\Pi a_i^{v_i}$	product of the activities of the species 'i'

7.2 Abbreviations

Lower Case Letters

a	amorphous
fcc	face-centered cubic
hcp	hexagonal close packed

Capital Letters

APCVD	atmospheric pressure chemical vapor deposition
CVD	chemical vapor deposition
GAXRD	glancing angle X-ray diffraction
GDOES	glow discharge optical emission spectroscopy
GIR-FTIR	grazing incidence reflection Fourier transform infrared
HTCVD	high temperature chemical vapor deposition

JCPDS	joint committee of powder diffraction standards
LOM	light optical microscopy
LPCVD	low pressure chemical vapor deposition
LTCVD	low temperature chemical vapor deposition
MOCVD	metal organic chemical vapor deposition
MTCVD	medium temperature chemical vapor deposition
PACVD	photo-assisted chemical vapor deposition
PECVD	plasma-enhanced chemical vapor deposition
PVD	physical vapor deposition
SEM	scanning electron microscopy
TACVD	thermally activated chemical vapor deposition
UHVCVD	ultrahigh vacuum chemical vapor deposition
XRD	X-ray diffraction

8 Literature

- 1 D.T. Quinto, *Int. J. Refract. Met. Hard Mat.* 14 (1996) 7.
- 2 C. Subramanian, K.N. Strafford, T.P. Wilks, L.P. Ward, *J. Mat. Processing Technol.* 56 (1996) 385.
- 3 W. Schedler: 'Hartmetall für den Praktiker', Plansee TIZIT GmbH, VDI, Düsseldorf, 1988, p. 213.
- 4 E.D. Hondros, in: 'Advanced Techniques for Surface Engineering' (ed. W. Gissler, H.A. Jehn), Kluwer Academic Publishers, Dordrecht, 1992, p. 1-4.
- 5 H. Damm, *Werkstatt und Betrieb*, 3 (2004) 10-22.
- 6 R.F. Bunshah: 'Handbook of Hard Coatings', Noyes Publications, Park Ridge, New Jersey, 2001.
- 7 S. Ruppi, *J. Phys. IV France* 11 (2001) Pr3-847.
- 8 W.-D. Münz, *J. Vac. Sci. Technol. A* 4 (1986) 2717.
- 9 S. Anderbouhr, E. Blanquet, V. Ghetta, C. Bernard, *Electroch. Soc. Proc. of the 14th Conf. EUROCVI XI* 25 (1997) 356.
- 10 K.L. Choy, *Progr. Mat. Sci.* 48 (2003) 57.
- 11 K.-H. Habig, *J. Vac. Sci. Technol. A* 4 (1986) 2832.
- 12 A.J. Fortini, R. La Ferla, R.H. Tuffias, R.B. Kaplan: in 'Processing and Fabrication of Advanced Materials for High Temperature Applications – II' (eds. V.A. Ravi, T.S. Srivatsan), The Minerals, Metals, & Materials Society, 1993, p. 387-403.
- 13 N. Ramanuja, R.A. Levy, S.N. Dharmadhikari, E. Ramos, C.W. Pearce, S.C. Menasian, P.C. Schamberger, C.C. Collins, *Mat. Lett.* 57 (2002) 261.
- 14 H.O. Pierson: 'Handbook of Chemical Vapor Deposition (CVD)', Noyes Publication, Park Ridge, New Jersey, 1992.
- 15 A. Love, S. Middleman, A.K. Hochberg, *J. Crystal Growth* 129 (1993) 119.
- 16 A. Larsson, S. Ruppi, *Thin Solid Films* 402 (2002) 203.
- 17 W. Schintlmeister, W. Wallgram, J. Kanz, K. Gigl, *Wear* 100 (1984) 153.
- 18 J.-O. Carlsson, *Thin Solid Films* 130 (1985) 261.
- 19 J.M. Blocher, Jr.: in 'Deposition Technologies for Films and Coatings' (ed. R.F. Bunshah), Noyes Publication, Park Ridge, New Jersey, 1982, p. 335-364.

- 20 M. Ohring: 'The Materials Science of Thin Films', Academic Press, San Diego, 1992.
- 21 H.E. Rebenne, D.G. Bhat, Surf. Coat. Technol. 63 (1994) 1.
- 22 N. Yoshikawa, Rec. Res. Devel. Mat. Sci. 3 (2002) 17.
- 23 V. Edlmayr: 'The Deposition of Metastable (Ti,Al)N Coatings by Thermal CVD', Diploma Thesis, Leoben, 2006.
- 24 Ö. Danielsson, E. Janzén, J. Crystal Growth 253 (2003) 26.
- 25 S.R. Kurtz, R.G. Gordon, Thin Solid Films 140 (1986) 277.
- 26 J.O. Carlsson, J. Vac. Sci. Technol. A 6 (1988) 1656.
- 27 M.J. Pilling, P.W. Seakins: 'Reaction Kinetics', Oxford University Press, Oxford, 1995.
- 28 J.P. Dekker, P.J. van der Put, H.J. Veringa, J. Schoonman, J. Electrochem. Soc. 141 (1994) 787.
- 29 R.I. Masel: 'Principles of Adsorption and Reaction on Solid Surfaces', John Wiley, New York, 1996.
- 30 D.M. Dobkin, M.K. Zuraw: 'Principles of Chemical Vapor Deposition', Kluwer Academic Publishers, Dordrecht, 2003.
- 31 N. Nakanishi, S. Mori, E. Kato, J. Electrochem. Soc. 137 (1990) 322.
- 32 M.S. You, N. Nakanishi, E. Kato, J. Electrochem. Soc. 138 (1991) 1394.
- 33 H.-E. Cheng, M.-J. Chiang, M.-H. Hon, J. Electrochem. Soc. 142 (1995) 1573.
- 34 P.B. Barna, M. Adamik, Thin Solid Films 317 (1998) 27.
- 35 P.B. Barna: Proc. 27th Int. Summer School: 'Diagnostics and Applications of Thin Films', Chlum u Třeboně, Czechoslovakia, 1991, p. 295-310.
- 36 I.Y. Konyashin, Chem. Vap. Dep. 2 (1996) 199.
- 37 W. Schintlmeister, O. Pacher, K. Pfaffinger, T. Raine, J. Electrochem. Soc. 123 (1976) 924.
- 38 I.Y. Konyashin, Thin Solid Films 249 (1994) 174.
- 39 H.-E. Cheng, M.-H. Hon, J. Appl. Phys. 70 (1996) 8047.
- 40 K.-T. Rie, A. Gebauer, J. Woehle, Surf. Coat. Technol. 60 (1993) 385.
- 41 B. A. Movchan, A. V. Demchisin, Phys. Metals Metallogr. 28 (1969) 83.
- 42 J. A. Thornton, J. Vac. Sci. Technol. 11 (1974) 666.
- 43 R. Messier, A.P. Giri, R.A. Roy, J. Vac. Sci. Technol. A 2 (1984) 500.

- 44 P.B. Barna, M. Adamik: 'Protective Coatings and Thin Films' (eds. Y. Pauleau, P.B. Barna), Kluwer Academic Publishers, Dordrecht, 1997, p. 279-297.
- 45 J.M. Blocher, Jr., J. Vac. Sci. Technol. 11 (1974) 680.
- 46 D.-J. Cheng, W.-P. Sun, M.-H. Hon, Thin Solid Films 146 (1987) 45.
- 47 H. Holleck, Metall 43 (1989) 614.
- 48 H. Holleck, J. Vac. Sci. Technol. A 4 (1986) 2661.
- 49 J.-E. Sundgren, H.T.G. Hentzell, J. Vac. Sci. Technol. A 4 (1986) 2259.
- 50 P.J. Burnett, D.S. Rickerby, Thin Solid Films 148 (1987) 51.
- 51 P.H. Mayrhofer, C. Mitterer, H. Clemens, Adv. Eng. Mat. 7 (2005) 1.
- 52 R.W. Cahn, P. Haasen, 'Physical Metallurgy', Elsevier, Amsterdam (1996).
- 53 P.H. Mayrhofer, C. Mitterer, L. Hultman, H. Clemens, Progr. Mat. Sci. 51 (2006) 1032.
- 54 S. Ruppi, Int. J. Refract. Met. Hard Mat. 23 (2005) 306.
- 55 M.H. Staia, E.S. Puchi, D.B. Lewis, J. Cawley, D. Morel, Surf. Coat. Technol. 86-87 (1996) 432.
- 56 S.C. Tjong, H. Chen, Mat. Sci. Eng. R 45 (2004) 1.
- 57 S. Ruppi, A. Larsson, J. Vac. Sci. Technol. A 21 2003 66.
- 58 M. Kathrein, W. Schintlmeister, W. Wallgram, U. Schleinkhofer, Surf. Coat. Technol. 163-164 (2003) 181.
- 59 B. Rother, H. Kappl, Surf. Coat. Technol. 96 (1997) 163.
- 60 H. Holzschuh, Thin Solid Films 469-470 (2004) 92.
- 61 P.B. Barna, M. Adamik, J. Lábár, L. Kövér, J. Tóth, A. Dévényi, R. Manaila, Surf. Coat. Technol. 125 (2000) 147.
- 62 D. Hochauer: 'Structure and Properties of Ti-N-B Coatings Deposited by Thermal CVD', Diploma Thesis, Leoben, 2006.
- 63 Z. Wokulski, Phys. Stat. Solidi 120 (1990) 175.
- 64 J.-E. Sundgren, B.O. Johansson, A. Rockett, S.A. Barnett, J.E. Greene, in: W.D. Sproul, J.A. Thornton, J.E. Greene, Physics and Chemistry of Protective Coatings, American Institute of Physics, Universal City, (1986) p. 95.
- 65 B.O. Johansson, J.-E. Sundgren, J.E. Greene, A. Rockett, S.A. Barnett, J. Vac. Sci. Technol. A 2 (1985) 303.

- 66 W.-J. Chou, G.-P. Yu, J.-H. Huang, *Surf. Coat. Technol.* 149 (2002) 7.
- 67 P. Patsalas, C. Chariditis, S. Logothetidis, *Surf. Coat. Technol.* 125 (2000) 335.
- 68 H.-E. Cheng, Y.-W. Wen, *Surf. Coat. Technol.* 179 (2004) 103.
- 69 D.G. Bhat, D.C. Shah, S.P. Boppana, C. Sung, in: T.S. Sudarshan, J.S. Braza (Eds.), *Surface Modification Techniques VI*, Metallurgical Society, Warrendale, PA, 1993, p. 671.
- 70 G.B. Harris, *Phil. Mag.* 43 (1952) 113.
- 71 M. Birkholz: 'Thin Film Analysis by X-Ray Scattering', WILEY-VCH, Weinheim, 2006
- 72 H. Holleck, *Surf. Coat. Technol.* 36 (1988) 151.
- 73 O. Knotek, W.-D. Münz, T. Leyendecker, *J. Vac. Sci. Technol. A* 5 (1987) 2173.
- 74 K.H. Kim, S.H. Lee, *Thin Solid Films* 283 (1996) 165.
- 75 S. PalDey, S.C. Deevi, *Mat. Sci. Eng. A* 342 (2003) 58.
- 76 P.H. Mayrhofer, A. Hörling, L. Karlsson, J. Sjöln, T. Larsson, L. Hultman, *Appl. Phys. Lett.* 83 (2003) 2049.
- 77 S. Ikeda, S. Gilles, B. Chenevier, *Thin Solid Films* 315 (1998) 257.
- 78 S. Anderbouhr, V. Ghetta, E. Blanquet, C. Chabrol, F. Schuster, C. Bernard, R. Madar, *Surf. Coat. Technol.* 115 (1999) 103.
- 79 I. Endler, M. Herrmann, M. Naupert, R. Pitonak, S. Ruppi, M. Schneider, H. van den Berg, H. Westphal, *Proc. Euro PM2006*, (2006), p. 219-224.
- 80 A. Mitsuo, S. Uchida, N. Nihira, M. Iwaki, *Surf. Coat. Technol.* 103-104 (1998) 98.
- 81 C. Mitterer, F. Holler, F. Üstel, D. Heim, *Surf. Coat. Technol.* 125 (2000) 233.
- 82 G.N. Komratov, *Powd. Metallurgy Met. Ceram.* 36 (1997) 510.
- 83 T. Maruyama, *Thermochim. Acta* 92 (1985) 827.
- 84 I. Suni, D. Sigurd, K.T. Ho, M.-A. Nicolet, *J. Electrochem. Soc.* 130 (1983) 1210.
- 85 I.G. Polyakoava, T. Hübert, *Surf. Coat. Technol.* 141 (2001) 55.
- 86 M. Wittmer, J. Noser, H. Melchior, *J. Appl. Phys.* 52 (1981) 6659.
- 87 S. Shimada, *J. Ceram. Soc. Jap.* 109 (2001) S33.
- 88 A. Bellucci, D. Gozzi, *Chem. Mat.* 15 (2003) 1217.
- 89 D. Gozzi, G. Cascino, S. Loreti, C. Minarini, S. Shimada, *J. Electrochem. Soc.* 148 (2001) J15.

- 90 V.A. Zhilyaev, V.D. Lyubimov, *Inorg. Mat.* 10 (1974) 47.
- 91 C. Héau, R.Y. Fillit, F. Vaux, F. Pascaretti, *Surf. Coat. Technol.* 120-121 (1999) 200.
- 92 R.F. Voitovich, É.A. Pugach, *Sov. Powder Metall. Met. Ceram.* 14 (1975) 132.
- 93 R.J. Irving, I.G. Worsley, *J. Less-Common Met.* 16 (1968) 103.
- 94 M. Zhou, Y. Makino, M. Nose, K. Nogi, *Thin Solid Films* 339 (1999) 203.
- 95 D. McIntyre, J.E. Greene, G. Håkansson, J.-E. Sundgren, W.-D. Münz, *J. Appl. Phys.* 67 (1990) 1542.
- 96 M. Diserens, J. Patscheider, F. Lévy, *Surf. Coat. Technol.* 120-121 (1999) 158.
- 97 J. Patscheider, T. Zehnder, M. Diserens, *Surf. Coat. Technol.* 146-147 (2001) 201.
- 98 T. Hirai, S. Hayashi, *J. Mat. Sci.* 17 (1982) 1320.
- 99 G. Llauro, R. Hillel, F. Sibieude, *Chem. Vap. Dep.* 4 (1998) 247.
- 100 T. Aizawa, T. Akhadejdamrong, A. Mitsuo, *Surf. Coat. Technol.*, 177-178 (2004) 573.
- 101 S.J. Bull, in: 'Advanced Techniques for Surface Engineering' (ed. W. Gissler, H.A. Jehn), Kluwer Academic Publishers, Dordrecht, 1992, p. 31-68.
- 102 S. Katayama, M. Hashimura, *Key Eng. Mat.* 138-140 (1998) 245.
- 103 J.A. Thornton, D.W. Hoffman, *Thin Solid Films* 171 (1989) 5.
- 104 D.M. Mattox: in 'Deposition Technologies for Films and Coatings' (ed. R.F. Bunshah), Noyes Publication, Park Ridge, New Jersey, 1982, p. 63-82.
- 105 B. Lux, R. Haubner, C. Wohlrab, *Surf. Coat. Technol.* 38 (1989) 267.
- 106 D.G. Bhat, T. Cho, P.F. Woerner, *J. Vac. Sci. Technol. A* 4 (1986) 2713.
- 107 N.K. Sharma, W.S. Williams, R.J. Gottschall, *Thin Solid Films* 45 (1977) 265.
- 108 W. Schintlmeister, W. Wallgram, K. Gigl, *High Temp. – High Press.* 18 (1986) 211.
- 109 K. Bartsch, *Proc. 11th Int. Symp. Boron, Borides and Related Comp.: 'A Thermodynamic and Experimental Study of the Transition Metal Boride Formation in the TiB₂ and B_xC Deposition on Hard Metals by CVD'*, (eds. R. Uno, I. Higashi), Tsukabe, Japan, 1993, p. 204-207.
- 110 G. Giunta, M. Fiorini, V. Vittori, G. Marchesano, *Surf. Coat. Technol.* 49 (1991) 174.
- 111 L.E. Toth, 'Transition Metal Carbides and Nitrides', Academic Press, New York, 1971.
- 112 J.-E. Sundgren, *Thin Solid Films* 128 (1985) 21.

- 113 M.J. Buiting, A.F. Otterloo, *J. Electrochem. Soc.* 139 (1992) 2580.
- 114 R.I. Hegde, R.W. Fiordalice, E.O. Travis, P.J. Tobin, *J. Vac. Sci. Technol. B* 11 (1993) 1287.
- 115 A. Agüero, D. Little, P. Lowden, *Mat. Res. Soc. Symp. Proc.* 163 (1990) 311.
- 116 C.-C. Jiang, T. Goto, T. Hirai, *J. Alloys Comp.* 190 (1993) 197.
- 117 R.M. Fix, R.G. Gordon, D.M. Hoffman, *Mat. Res. Soc. Symp. Proc.* 168 (1990) 357.
- 118 K. Ishihara, K. Yamazaki, H. Hamada, K. Kamisako, Y. Tarui, *Jpn. J. Appl. Phys.* 29 (1990) 357.
- 119 R. Bonetti, H. Wiprächtiger, E. Mohn, *Met. Powder Rep.* 45 (1990) 837.
- 120 W. Gissler, T.P. Mollart, R. Gilmore: in 'Protective Coatings and Thin Films' (eds. Y. Pauleau, P.B. Barna), Kluwer Academic Publishers, Dordrecht, 1997, p. 357-366.
- 121 W. Gissler, *Surf. Coat. Technol.* 68-69 (1994) 556.
- 122 H. Nowotny, F. Benesowsky, C. Brukl, O. Schob, *Mh. Chem.* 92 (1961) 403.
- 123 V.D. Chupov, S.S. Ordan'yan, L.V. Kozlovskii, *Inorg. Mat.* 17 (1981) 1195.
- 124 W. Schintlmeister, W. Wallgram, Patent, EP0306077 B1 (1988).
- 125 H. Holzschuh, Patent, EP1365045 (2003).
- 126 J.-L. Peytavy, A. Lebugle, G. Montel, *High Temp. High Press.* 10 (1978) 341.
- 127 J.-L. Peytavy, A. Lebugle, G. Montel, *Wear* 52 (1979) 89.
- 128 H. Holzschuh, in Proc. 16th Int. Plansee Seminar, Plansee, Reutte, 2005, Vol. 2, 801.
- 129 O. Knotek, M. Böhmer, T. Leyendecker, *J. Vac. Sci. Technol. A* 4 (1986) 2695.
- 130 P.H. Mayrhofer D. Music, J.M. Schneider, *Appl. Phys. Lett.* 88 (2006) 071922.
- 131 I. Endler, M. Herrmann, M. Naupert, R. Pitonak, S. Rupp, M. Schneider, H. van den Berg, H. Westphal, Proc. Euro PM2006 (2006) 219.
- 132 S. Gilles, N. Bourhilla, S. Ikeda, C. Bernard, R. Madar, *Surf. Coat. Technol.* 94-95 (1997) 285.
- 133 I.M. Hutchings: 'Tribology: Friction and Wear of Engineering Materials', Edward Arnold, London, 1992.
- 134 S. Hogmark, S. Jacobson, M. Larsson, *Wear* 246 (2000) 20.
- 135 E. Rabinowicz: 'Friction and Wear of Materials', John Wiley, New York, 1995.
- 136 K. Holmberg, H. Ronkainen, A. Matthews, *Ceram. Int.* 26 (2000) 787.

- 137 K. Holmberg, A. Matthews: 'Coatings Tribology, Properties, Techniques and Applications in Surface Engineering', Elsevier, Amsterdam, 1994.
- 138 N.P. Suh, H.-C. Sin, *Wear* 69 (1981) 91.
- 139 B. Bhushan: 'Principles and Applications of Tribology', John Wiley, New York, 1999.
- 140 S.E. Franklin, J. Beuger, *Surf. Coat. Technol.* 54-55 (1992) 459.
- 141 C. Donnet, A. Erdemir, *Surf. Coat. Technol.* 180-181 (2004) 76.
- 142 E. Badisch, C. Mitterer, P.H. Mayrhofer, G. Mori, R.J. Bakker, J. Brenner, H. Störi, *Thin Solid Films* 460 (2004) 125.
- 143 A. Erdemir, C. Donnet: in 'Modern Tribology Handbook, Vol. 2', (ed. B. Bhushan), CRC Press, Boca Raton, 2001, p.871-908
- 144 K.-H. zum Gahr: 'Microstructure and Wear of Materials', Elsevier, Amsterdam, 1987.
- 145 E. Santner, D. Klaffke, G. Meier zu Köcker, *Wear* 190 (1995) 204.
- 146 D. Klaffke, A. Skopp, I. Lenke, *Surf. Coat. Technol.* 74-75 (1995) 877.
- 147 J.G. Delly: in 'Encyclopedia of Materials Characterization: Surfaces, Interfaces, Thin Films', (eds. C.R. Brundle, C.A. Evans, Jr., S. Wilson), Butterworth-Heinemann, Boston, 1992, p. 60-69.
- 148 J.B. Bindell: in 'Encyclopedia of Materials Characterization: Surfaces, Interfaces, Thin Films', (eds. C.R. Brundle, C.A. Evans, Jr., S. Wilson), Butterworth-Heinemann, Boston, 1992, p. 70-84.
- 149 M.R. Winchester, R. Payling, *Spectrochim. Acta B* 59 (2004) 607.
- 150 B.D. Cullity, 'Elements of X-ray Diffraction', Addison-Wesley, Reading Massachusetts, 1978.
- 151 W. Gissler, J. Haupt: in 'Protective Coatings and Thin Films' (eds. Y. Pauleau, P.B. Barna), Kluwer Academic Publishers, Dordrecht, 1997, p. 313-333.
- 152 I.C. Noyan, J.B. Cohen, 'Residual Stress', Springer Verlag, New York, 1987.
- 153 ASTM, Designation G99–95a: 'Standard Test Method for Wear Testing with a Pin-on-Disk Apparatus'. ASTM, Philadelphia, PA, 1995, p. 336-390.
- 154 Veeco Metrology Group: 'WYKO Surface Profilers – Technical Reference Manual', Version 2.21, Arizona, 1999.
- 155 C. Heermant, D. Dengl, *Materialprüfung* 38 (1996) 374.
- 156 A.C. Fischer-Cripps, *Vacuum* 58 (2000) 569.

- 157 R.L. McCreery, 'Raman Spectroscopy for Chemical Analysis', Chemical Analysis Vol. 157 Wiley-Interscience, New York, 2000.
- 158 J.N. Cox: in 'Encyclopedia of Materials Characterization: Surfaces, Interfaces, Thin Films', (eds. C.R. Brundle, C.A. Evans, Jr., S. Wilson), Butterworth-Heinemann, Boston, 1992, p. 416-427.
- 159 C.V. Raman, K.S. Krishnan, Nature 121 (1928) 501.
- 160 W.B. White: in 'Encyclopedia of Materials Characterization: Surfaces, Interfaces, Thin Films', (eds. C.R. Brundle, C.A. Evans, Jr., S. Wilson), Butterworth-Heinemann, Boston, 1992, p. 428-441.
- 161 G.V. Samsonov, 'The Oxide Handbook', IFI/Plenum Press, New York, 1982.
- 162 U. Diebold, Surf. Sci. Rep. 48 (2003) 53.
- 163 R.J. Meyer, E.H. Erich Pietsch, 'Gmelins Handbuch der anorganischen Chemie – Titan', Vol. 41, Verlag Chemie, Weinheim, 1951.
- 164 U. Balachandran, N.G. Eror, J. Solid State Chem. 42 (1982) 276.
- 165 R.J. Capwell, F. Spagnolo, M.A. DeSesa, Appl. Spectrosc. 26 (1972) 537.
- 166 J.C. Parker, R.W. Siegel, Appl. Phys. Lett. 57 (1990) 943.
- 167 J. Robertson, Mat. Sci. Eng. R 37 (2002) 129.
- 168 B. Oral, R. Hauert, U. Müller, K.-H. Ernst, Diam. Rel. Mat. 4 (1995) 482.
- 169 T. Zehnder, P. Schwaller, F. Munnik, S. Mikhailov, J. Patscheider, J. Appl. Phys. 95 (2004) 4327.
- 170 A. Bartl, S. Bohr, R. Haubner, B. Lux, Int. J. Refract. Met. Hard Mat. 14 (1996) 145.
- 171 J.R. Durig, W.H. Green, A.L. Marston, J. Molec. Struct. 2 (1968) 19.

9 Publications

9.1 List of Included Publications

- [I] The effect of deposition temperature on microstructure and properties of thermal CVD TiN coatings, *J. Wagner, C. Mitterer, M. Penoy, C. Michotte, W. Wallgram, M. Kathrein*, International Journal of Refractory Metals and Hard Materials, 2007, submitted.
- [II] Structure and properties of CVD TiC_xN_{1-x} coatings, *J. Wagner, C. Mitterer, M. Penoy, C. Michotte, W. Wallgram, M. Kathrein*, Proceedings of the 16th International Plansee Seminar 2005, Vol. 2, p. 917-931.
- [III] The influence of boron content on the tribological performance of Ti–N–B coatings prepared by thermal CVD, *J. Wagner, D. Hochauer, C. Mitterer, M. Penoy, C. Michotte, W. Wallgram, M. Kathrein*, Surface and Coatings Technology 201 (2006) 4247-4252.
- [IV] Deposition of Ti–Al–N coatings by thermal CVD, *J. Wagner, V. Edlmayr, M. Penoy, C. Michotte, C. Mitterer, M. Kathrein*, Surface and Coatings Technology, 2007, submitted.

9.2 Supervised Diploma Theses

- [V] *D. Hochauer*: ‘Structure and properties of Ti–N–B coatings deposited by thermal CVD’, Leoben, 2006.
- [VI] *V. Edlmayr*: ‘The deposition of metastable (Ti,Al)N coatings by thermal CVD’, Leoben, 2006.

9.3 Contribution to the Included Publications

	Conception and Planning*	Experiments	Analysis and Interpretation	Manuscript Preparation*
Publication I	100	80	90	100
Publication II	100	80	90	100
Publication III	100	20	90	100
Publication IV	100	30	90	100

* Guidance by my supervisor not included.

Publication I

The effect of deposition temperature on microstructure and properties of thermal CVD TiN coatings

J. Wagner, C. Mitterer, M. Penoy, C. Michotte, W. Wallgram, M. Kathrein

**submitted to
International Journal of Refractory Metals and Hard Materials**

The effect of deposition temperature on microstructure and properties of thermal CVD TiN coatings

J. Wagner^a, C. Mitterer^b, M. Penoy^c, C. Michotte^c, W. Wallgram^d, M. Kathrein^d

^{a)} *Materials Center Leoben Forschung GmbH, Franz-Josef-Strasse 13, A-8700 Leoben, Austria*

^{b)} *Department of Physical Metallurgy and Materials Testing, University of Leoben, Franz-Josef-Strasse 18, A-8700 Leoben, Austria*

^{c)} *CERATIZIT Luxembourg S.à.r.l., L-8201 Mamer, Luxembourg*

^{d)} *CERATIZIT Austria GmbH, A-6600 Reutte, Austria*

Abstract

Coatings of TiN have been deposited by thermal CVD between 850 and 1050°C and characterized with respect to their microstructure as well as mechanical and tribological properties. X-ray diffraction (XRD) analysis yields the formation of textured films, particularly at low deposition temperatures. It is shown that the coating hardness changes with the texture, where highly (211) oriented films exhibit a lower hardness compared to non-textured coatings. The wear resistance has been determined by dry sliding experiments against Al₂O₃ balls at 25°C on both as-deposited and polished samples. Independent on the surface roughness, the smaller grain size of the textured films causes a higher toughness and results in a better wear resistance.

Keywords: TiN; CVD; Structure; Hardness; Tribology

1 Introduction

TiN coatings are applied for cutting tools since more than three decades and still are an integral constituent in modern tools. The successful application of TiN originates from its excellent mechanical properties and thermal stability that give well-adherent and wear resistant coatings. Additionally, the pleasant golden color of TiN enables an easier wear detection, but is also a marketing argument [1,2]. Different physical vapor deposition (PVD) and chemical vapor deposition (CVD) techniques are used to produce TiN coatings and have been extensively reviewed [3-5]. Especially, the deposition of TiN by thermal CVD on cemented carbide tools using the precursors TiCl₄, N₂ and H₂ is a well-established process. The coatings are characterized by an excellent adherence and a high hardness. Although the deposition of TiN by CVD is well-known, most investigations consider either the coating growth [6,7], mechanical properties [8,9], or their tribological behavior [10,11]. Nevertheless, only few consider the correlation between the deposition conditions, coating morphology and the resultant mechanical and tribological properties.

The objective of this study is to correlate the mechanical and tribological properties of thermal CVD TiN coatings with the deposition process, in particular with the most influencing parameter – the deposition temperature.

2 Experimental

The coatings have been produced by thermal CVD in an industrial deposition unit at atmospheric pressure [12]. The process was performed using the precursors TiCl_4 , N_2 , H_2 , and Ar. Variations of the deposition temperature T_{dep} have been performed between 850 and 1050°C at a constant gas composition. The deposition time was adjusted according to the growth rate to reach a coating thickness of $5 \pm 0.5 \mu\text{m}$. Polished cemented carbide cutting inserts (77 wt.% WC, 11 wt.% Co, 4 wt.% TiC, 8 wt.% (Ta,Nb)C) were used as substrates. The coating thickness was measured from polished cross-sections with light optical microscopy (LOM). The surface morphology was studied using a Cambridge Instruments Stereoscan 360 scanning electron microscope (SEM). X-ray diffraction (XRD) analysis was conducted in Bragg-Brentano geometry to assess the coating texture using a Siemens D500 diffractometer, while residual stress measurements were performed with a Panalytical X'Pert Pro employing the $\sin^2\psi$ -method. $\text{CuK}\alpha$ radiation was utilized in both measurements. A UMIS-II nanoindentation instrument [13] equipped with a Berkovich indenter was used for hardness measurements. Loads between 10 and 25 mN have been used to avoid influences from the substrate and crack formation in the coatings. The area function for the indenter was obtained on fused silica using an elastic modulus of 72.5 GPa as reference. To avoid influences from surface roughness, the samples have been polished metallographically, first with 1 μm diamond suspension and finally with colloidal silica suspension. The tribological behavior was examined by dry-sliding experiments using a CSM tribometer in a ball-on-disc arrangement. As-deposited as well as polished samples were tested using the same polishing procedure as for the hardness tests. The TiN coatings were worn against alumina ball counterparts ($\varnothing 6 \text{ mm}$) at 25°C in ambient air with a relative humidity of $27 \pm 3 \%$. The sliding speed, wear track radius, and normal load were kept constant at 10 cm/s, 5 mm, and 5 N, respectively. The sliding distance was 1000 m for the as-deposited coatings and 500 m for the polished. After ball-on-disc tests the worn volume was measured by white-light profilometry (Wyko NT 1000). Also the average surface roughness R_a was determined with the optical profilometer. The wear tracks were also examined by SEM using a Zeiss evo50.

3 Results and discussion

3.1 Growth rate

The deposition temperature is one of the main parameters influencing the growth rate as can be seen from the Arrhenius plot in Fig. 1. The growth rate increases from 0.9 to

5.1 $\mu\text{m/h}$ as T_{dep} rises from 850 to 1050°C. From the slope of the Arrhenius plot, the rate-limiting mechanism can be determined.

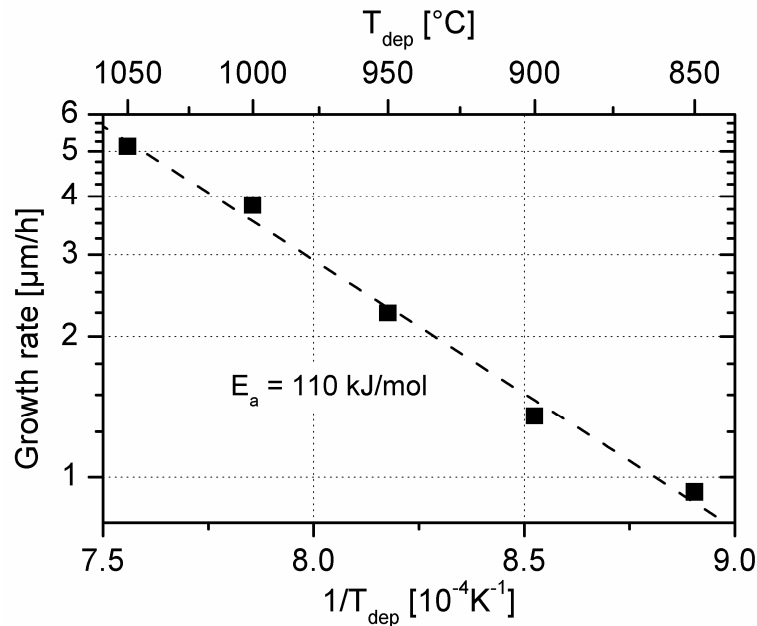


Fig. 1: Arrhenius plot for the growth rate of TiN.

The apparent activation energy E_a is a function of reactant concentration and temperature. In case of reactant depletion within the reactor, the reactant concentration and consequently the apparent activation energy will change. Higher temperatures enhance the depletion of reactants at a given position in the reactor, hence, the growth characteristic will change with temperature. Nevertheless, the apparent activation energy is useful to determine the rate controlling mechanism [3,6]. An apparent activation energy of 110 kJ/mol has been calculated which indicates, due to the high value, that the process is controlled by surface kinetics within the investigated temperature range [7].

3.2 Coating morphology and crystallographic structure

SEM micrographs of the TiN surfaces are shown in Fig. 2. Large star-shaped crystals intermixed with lenticular crystals appear at a deposition temperatures of 850°C (Fig. 2a). The star-shaped crystals are still present at 950°C (Fig. 2b), but the crystals in-between have changed to a fine pyramidal structure. Between 950 and 1000°C the morphology alters to coarse faceted structures as shown in Fig. 2c and d, respectively and exhibits irregular arranged plates at 1050°C (Fig. 2e). The different morphologies are also reflected in the average surface roughness R_a . The R_a values are given in Fig. 2 together with the SEM images.

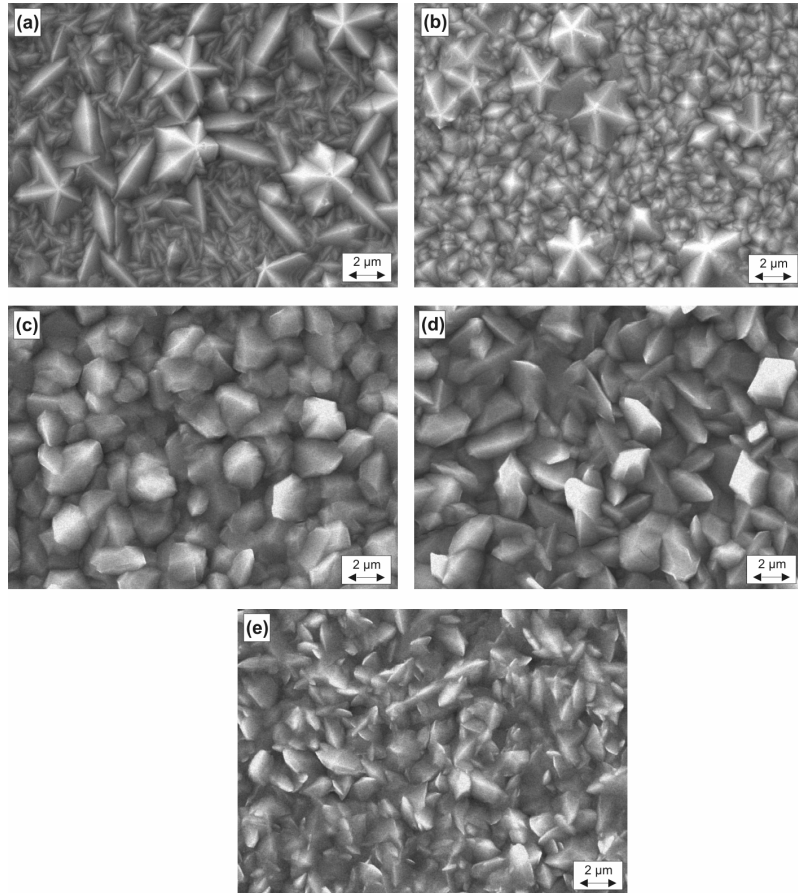


Fig. 2: Secondary SEM images from the surface and in brackets the corresponding average surface roughness R_a for deposition temperatures of (a) 850°C [47 nm], (b) 900°C [96 nm], (c) 950°C [284 nm], (d) 1000°C [289 nm], and (e) 1050°C [221 nm].

The crystalline structure of the coatings was examined by XRD analysis in Bragg-Brentano geometry, i.e. diffraction only occurs from planes parallel to the surface. Only reflection of TiN have been detected. Lattice parameters of 0.4241 nm close to the standard value of bulk TiN ($a_0 = 0.4240$ nm) have been determined with negligible differences between the coatings. From the diffraction patterns, the texture coefficient $TC_{(hkl)}$ for the planes (hkl) was calculated according to

$$TC_{(hkl)} = \frac{I_{(hkl)} / I_{0,(hkl)}}{1/n \sum I_{(hkl)} / I_{0,(hkl)}}$$

where $I_{(hkl)}$ is the measured peak intensity, $I_{0,(hkl)}$ is the standard intensity of powdered TiN from JCPDS file 38-1420, and n the number of considered reflections. Here, 7 reflections have been taken into account, and therefore, the highest value of $TC_{(hkl)}$ is 7 for a perfectly oriented material and 1 for a randomly orientated one [14]. The effect of the deposition temperature on the texture coefficients is shown in Fig. 3. The coatings deposited at 850 and 900°C exhibit a preferred (211) orientation with $TC_{(211)}$ values above 5. At 950°C the (110) and (211) orientations are slightly favored, whereas for $T_{dep} = 1000$ °C a (100) texture ($TC_{(100)} = 2.3$) can be observed. No preferred orientation can

be detected for the highest deposition temperature of 1050°C. The correlation between deposition temperature, texture coefficient and coating morphology corresponds well to results found in literature for CVD TiN coatings [2]. Lenticular and pyramidal structures (cf. Fig. 2a and b, respectively) show a preferred (211) orientation. (110) textured star-shaped crystals are favored at low deposition temperatures and their number decreases from 850 to 900°C. At 950°C, the (211) texture is less pronounced ($TC_{(211)} = 1.6$), while the (110) orientation is increased ($TC_{(110)} = 1.8$). A polyhedron surface morphology can be seen on this coatings (Fig. 2c). The (100) orientation is favored at 1000°C and the films exhibit faceted crystals (see Fig. 2d). No distinctive texture can be observed in the coating deposited at 1050°C. Also the surface morphology yields a irregular faceted structure. Generally, it can be noticed that the thermodynamically favorable crystal faces (i.e. of low surface energy), such as (100) and (111) become important with rising deposition temperature.

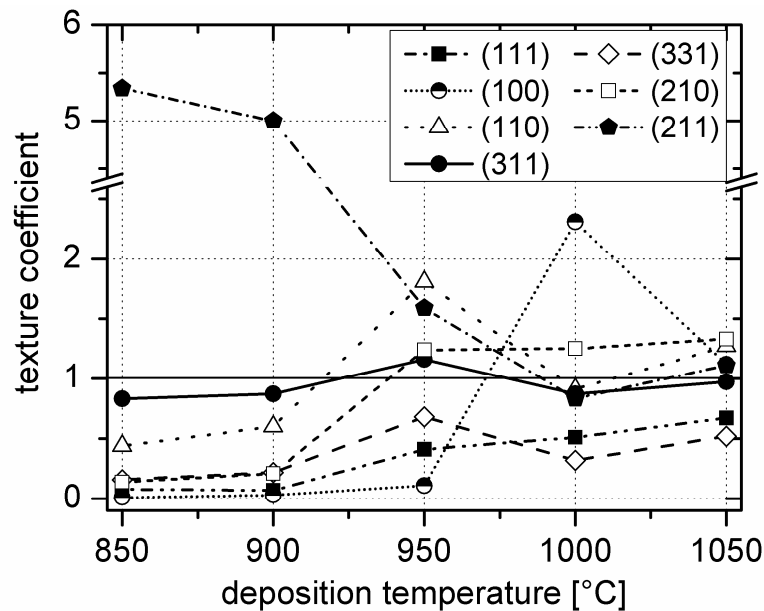


Fig. 3: Influence of deposition temperature on the texture coefficient.

The texture formation is the result of a competitive growth of different crystals, where only crystals with a high growth rate perpendicular to the surface will be left. During the nucleation stage different particles nucleate depending on the temperature. Low temperatures result in multiple twinned or laminated twinned particles, whereas twin free single crystals nucleate at high temperatures. After nuclei formation the crystal growth starts and is determined by the form of the crystals and the growth mechanisms, e.g. reentrant corners, screw dislocations, or stacking faults are preferential growth sites. Low temperatures and low adatom mobility, respectively result in the growth along these preferential sites. Multiple twinned nuclei at low temperatures result in the growth along five (111) twin planes in [110] direction and form star-shaped crystals, for instance. In contrary twin free nuclei and an enhanced surface mobility of adatoms at

high temperatures causes the crystal growth along the most thermodynamically favorable faces and polyhedral structures will develop. Furthermore, the adsorption of impurities, such as chlorine highly influences the surface energy of the growing faces [15,16].

3.3 Hardness

The effect of the deposition temperature on the hardness is exhibited in Fig. 4. Differences in hardness can be observed, where the hardness increases from 18 to 20.5 GPa with rising deposition temperature. The hardness of TiN is a complex issue and comprises the composition, defects, grain size, residual stresses, and texture of the material [4,17,18]. From the almost identical lattice parameters, no significant differences in composition can be expected. The thermal tensile stresses measured change from approximately 250 MPa for low deposition temperatures (850 – 950°C) to 400 – 450 MPa for the highest temperatures (1000 – 1050°C). It is common knowledge that high tensile stresses will lower the hardness [19].

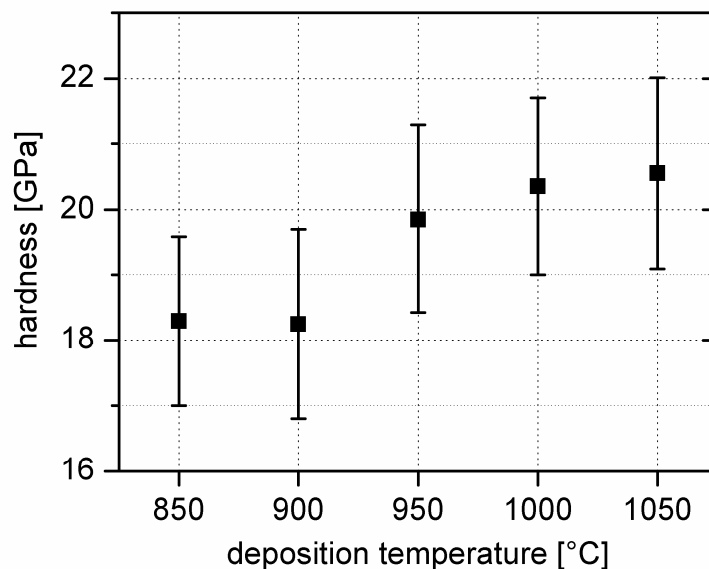


Fig. 4: The effect of deposition temperature on coating hardness.

The smallest surface structures can be observed for the coatings deposited at 850 and 900°C (see Fig. 2a and b). Moreover, as the surface morphology is related with the grain size, the smallest structure can be expected in these coatings as well as the highest hardness according to Hall-Petch relation. Nevertheless, the measurements exhibit lower hardness values compared to the coarse-structured coatings (cf. Fig. 2c and d). All the results give rise into the consideration that the differences in hardness originate from the observed texture. The hardness anisotropy of TiN is well-known, e.g. the hardness of CVD TiN whiskers shows a strong dependency on the coating/indenter orientation relationship [18]. Also, hardness measurements on magnetron sputtered single-crystal coatings have yielded different values of 23 GPa and 20 GPa for (111)

and (110) oriented films [20,21]. Most investigation have been executed on polycrystalline coatings grown by PVD [22-24] and CVD [8,9]. (111) and (100) oriented coatings are frequently found for PVD TiN films, but contradicting results have been observed regarding the hardness. All of these studies focus on low index planes and do not consider higher diffraction planes. To our knowledge, only one investigation concerns the influence of higher index planes on the hardness. Similar to the present study, the lowest hardness was measured for star-shaped (110) and lenticular-like (211) textured films, while mixed structures were accompanied by the highest hardness. The low hardness has been ascribed to a porous surface structure [9]. Here, the surface morphology of (211) textured films is compact and smooth compared to other coatings. Furthermore, all coatings have been polished to a roughness R_a of 15 – 20 nm. The results suggest that a (211) preferred orientation in TiN coatings causes a reduced hardness.

3.4 Tribological properties

Friction coefficients for all coatings varied between 0.9 – 1.1 for as-deposited and 0.8 – 1.0 for polished coatings, respectively. The wear rates obtained from ball-on-disc tests are illustrated in Fig. 5 for the as-deposited and polished samples. The influence of the surface state on the resultant wear rate is small except for the coating deposited at 850°C, where polishing resulted in less wear. According to the wear rates, the coatings can be divided into two groups: low wear rates for T_{dep} of 850 and 900°C and high wear rates between 950 and 1050°C. Moreover, SEM investigations of the wear tracks yielded a characteristic wear appearance of each group. For discussion, coatings deposited at 850 and 1000°C have been selected representatively and are shown in Fig. 6 and 7.

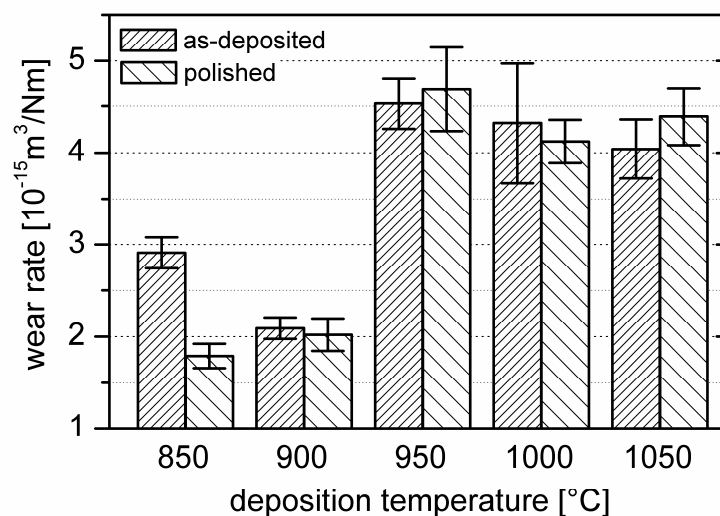


Fig. 5: Wear rate of TiN coatings deposited between 850 and 1050°C after ball-on-disc tests against Al_2O_3 counterparts.

For T_{dep} of 850°C, secondary SEM micrographs of the wear tracks after testing samples in the as-deposited and polished state are shown in Fig. 6a and b, respectively. In case of the as-deposited coating, the wear track exhibits deep grooves and scaly detachments of coating material. The damage pattern indicates that plastic deformation occurred to some extent via ploughing and wedge formation [25]. From the high coating thickness of 5 μm and the high substrate hardness, the formation of grooves from the plastic deformation of the substrate can be expected to be negligible. Although plastic deformation is very limited in hard ceramic materials, the penetration by small, sharp and hard particles enables plastic yielding of the coating. However, exceeding the plasticity limit of the material causes the formation of micro-cracks, where the intersection of these cracks results in material removal after repeated sliding contacts [26,27]. Backscatter SEM micrographs have shown the formation of cracks transversal to the sliding direction with a mean distance of approximately 15 μm in between. The abraded wedges preferentially stopped in front of these cracks. Besides cracks, the brittle nature of TiN can be observed by micro-chipping, i.e. by localized fracture of the columnar grains. The resultant surface relief enables to distinguish the individual grains (see Fig. 6a) [28]. Polishing of the sample prior to the ball-on-disc test improved the wear behavior of the coating (cf. Fig. 5). This alteration can also be observed on the wear track, which appears smoother without deep grooves and shows less and smaller wedges (see Fig. 6b). The difference could be also clearly noticed in profiler images from the wear tracks. For the unpolished specimen, fracture and crushing of the star-shaped and faceted crystals (cf. Fig. 2a) will result in a high amount of large wear debris causing the observed ploughing and wedge formation. Since polishing removes the coarse structures, the scoring decreased and therefore, the coating wear. The fracture of individual grains is the dominating wear mechanism. A similar wear behavior has been observed for TiN deposited at 900°C. Although the surface roughness is higher ($R_a = 96 \text{ nm}$) compared to the coating deposited at 850°C ($R_a = 47 \text{ nm}$), the number of coarse protruding structures is smaller and the surface appears more compact; hence, the influence of polishing is less distinctive.

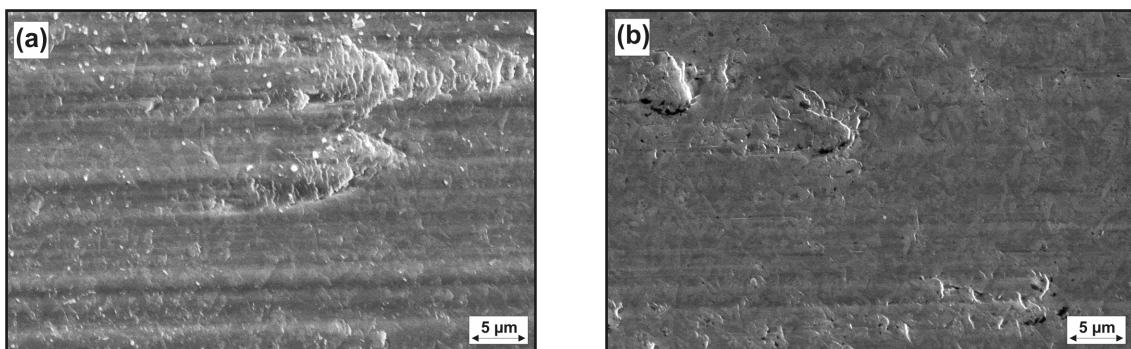


Fig. 6: Secondary SEM micrographs from the wear track of TiN deposited at 850°C tested in the (a) as-deposited and (b) polished state; sliding direction from left to right.

A different wear behavior can be seen for the coating deposited at 1000°C. For the specimen tested in the as-deposited state, only scattered grooves have been observed and the wear track appears smooth and polished. Because secondary SEM provided images of low contrast, the backscatter SEM micrograph is presented in Fig. 7a. The different TiN grains can be clearly distinguished, whereas only faint signs of grooves can be seen. Micro-chipping of the grains causes the polishing process as the wear proceeds and only localized plastic deformation occurs. Removal of the coarse surface asperities (see Fig. 2d) by polishing could not decrease the coating wear rate. Deep scars in the wear track disappeared almost entirely, but fracture of the columnar grains occurred more distinct compared to the unpolished specimen. Therefore, the roughness in the wear track increased as can be observed on the secondary SEM micrograph in Fig. 7b. The released fractured particles increase the number of debris in the wear track and intensify coating wear.

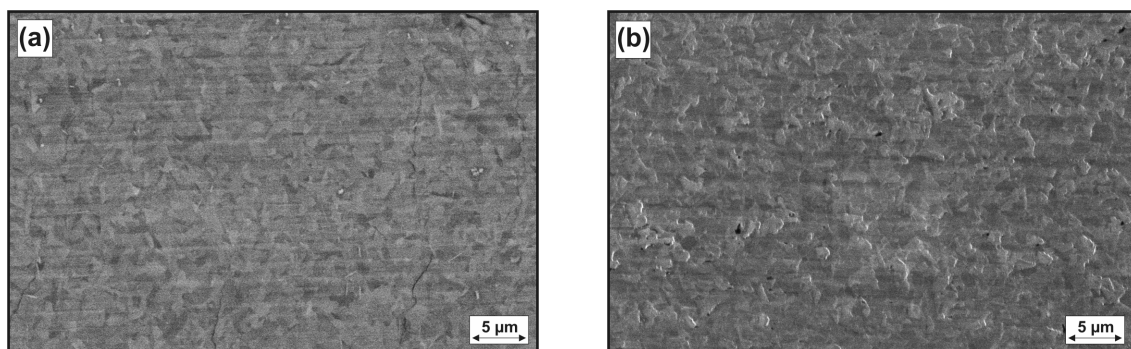


Fig. 7: SEM micrographs from the wear track inside: (a) as-deposited (backscatter SEM) and (b) polished (secondary SEM) surface state; sliding direction from left to right.

The above results exhibit that a transition in the wear mechanism occurs. While coatings deposited at high temperatures yield wear controlled by brittle fracture (micro-chipping), contribution of plastic deformation induced wear (ploughing and wedge formation) can be observed additionally at lower deposition temperatures. The higher ductility and toughness can be ascribed to the fine-grained structure of these coatings. The grain size influences both the yield strength σ_y and the fracture stress σ_f of the coating. According to the Hall-Petch relation, the yield strength of materials increases with $d^{-1/2}$. Also the corresponding fracture stress shows a similar behavior and tends to increase as a function of $d^{-1/2}$, such that brittle fracture occurs above a critical grain size. Below this limit, i.e. for $\sigma_y < \sigma_f$, plastic flow takes place, with increasing amount as the grain size decreases [29]. The improved ductility and fracture strength of these coatings more than compensate the slightly lower hardness and explain the low wear rates.

4 Conclusions

TiN coatings were deposited between 850 and 1050°C under surface kinetics controlled conditions. The coatings yield a highly preferred (211) orientation with fine-grained lenticular-like structures at 850°C and a pyramidal morphology at 900°C. This texture gradually diminishes at higher temperatures, while slightly (110) or (100) oriented films of faceted structure remain at 950 and 1000°C, respectively. Irregular faceted crystals without texture formed at 1050°C. The transition from highly (211) textured films to those without preferred orientation increases the coating hardness from 18 to 20.5 GPa. Nevertheless, (211) textured coatings exhibit the higher wear resistance in dry-sliding tests against Al₂O₃ independent on the surface roughness. The fine-grained structure of the textured coatings provides a high ductility and toughness causing a combination of brittle and ductile wear. Removal of surface asperities by preceding polishing reduced the scoring wear component and decreased the coating wear. In contrary, coatings deposited at high temperatures ($T_{dep} > 950^{\circ}\text{C}$) yielding larger crystals suffer predominantly from brittle fracture (micro-chipping). Polishing of the coatings could not improve the wear behavior. While deep grooves disappeared, fracture of the individual grains increased in return.

Acknowledgments

Financial support by the Austrian Kplus Competence Center Programme is gratefully acknowledged. The authors are grateful to K. Gigl for conducting the deposition processes and to G. Hawranek for the SEM investigations. Special thanks are due to J. Thurner for valuable discussions. Final thanks are due to DI M. Pfeiler and, particularly Dr. R. Daniel for the help in nanoindentation measurements.

References

- 1 Ruppel S. Advances in chemically vapour deposited wear resistant coatings. J Phys IV France 2001;11:847–59.
- 2 Prengel HG, Pfouts WR, Santhanam AT. State of the art in hard coatings for carbide cutting tools. Surf Coat Technol 1998;102:183–90.
- 3 Rebenne HE, Bhat DG. Review of CVD TiN coatings for wear-resistant applications: deposition processes, properties and performance. Surf Coat Technol 1994;63:1–13.
- 4 Sundgren J-E. Structure and properties of TiN coatings. Thin Solid Films 1985;128:21–44.
- 5 Fortuna SV, Sharkeev YP, Perry AJ, Matossian JN, Shulepov IA. Microstructural features of wear-resistant titanium nitride coatings deposited by different methods. Thin Solid Films 2000;377–378:512–17.

- 6 Dekker JP, Van der Put PJ, Veringa HJ, Schoonman J. A kinetic study of titanium nitride chemical vapor deposition using nitrogen, hydrogen, and titanium tetrachloride. *J Electrochem Soc* 1994;141:787–95.
- 7 Nakanishi N, Mori S, Kato E. Kinetics of chemical vapor deposition of titanium nitride. *J Electrochem Soc* 1990;137:322–28.
- 8 Shah DC, Bhat DG. Correlation between properties and performance of titanium nitride-coated cemented carbide cutting tools. In: Sudarshan TS, Bhat DG, Jeandin M, editors. *Surface modification techniques IV*, Warrendale: Metallurgical society; 1991, p. 79–95.
- 9 Cheng H-E, Wen Y-W. Correlation between process parameters, microstructure and hardness of titanium nitride films by chemical vapor deposition. *Surf Coat Technol* 2004;179:103–9.
- 10 Hintermann HE. Adhesion, friction and wear of thin hard coatings. *Wear* 1984;100:381–97.
- 11 Franklin SE, Beuger J. A comparison of the tribological behavior of several wear-resistant coatings. *Surf Coat Technol* 1992;54/55:459–65.
- 12 Schintlmeister W, Wallgram W, Kanz J, Gigl K. Cutting tool materials coated by chemical vapor deposition. *Wear* 1984;100:153–69.
- 13 Ultra-Micro Indentation System. CSIRO Division of Telecommunications and Industrial Physics. Bradfield Rd, West Lindfield, NSW Australia.
- 14 Birkholz M. *Thin film analysis by X-ray scattering*. Weinheim: Wiley-VCH; 2006.
- 15 Cheng H-E, Chiang M-J, Hon M-H. Growth characteristics and properties of TiN coating by chemical vapor deposition. *J Electrochem Soc* 1995;142:1573–78.
- 16 Cheng H-E, Hon M-H. Texture formation in titanium nitride films prepared by chemical vapor deposition. *J Appl Phys* 1996; 79:8047–53.
- 17 Sundgren J-E, Hentzell HTG. A review of the present state of art in hard coatings grown from the vapor phase. *J Vac Sci Technol A* 1986;4:2259–79.
- 18 Wokulski Z. Mechanical properties of TiN whiskers. *Phys Stat Solidi* 1990;120:175–84.
- 19 Oettel H, Bertram T, Weihnacht V, Wiedemann R, Von Zitzewitz S. Mechanical behaviour of TiN coatings. *Surf Coat Technol* 1997;97:785–89.

- 20 Sundgren J-E, Johansson BO, Rockett A, Barnett SA, Greene JE. TiN_x (0.6 < x < 1.2): atomic arrangements, electronic structure, and recent results on crystal growth and physical properties of epitaxial layers. In: Sproul WD, Thornton JA, Greene JE, editors. *Physics and chemistry of protective coatings*, Universal City: American Institute of Physics; 1986, p. 95–115.
- 21 Johansson BO, Sundgren J-E, Greene JE, Rockett A, Barnett SA. Growth and properties of single crystal TiN films deposited by reactive magnetron sputtering. *J Vac Sci Technol A* 1985;2:303–7.
- 22 Chou W-J, Yu G-P, Huang J-H. Mechanical properties of TiN thin film coatings on 304 stainless steel substrates. *Surf Coat Technol* 2002;149:7–13.
- 23 Patsalas P, Chariditis C, Logothetidis S. The effect of substrate temperature and biasing on the mechanical properties and structure of sputtered titanium nitride thin films. *Surf Coat Technol* 2000;125:335–40.
- 24 Mayrhofer PH, Kunc F, Musil J, Mitterer C. A comparative study on reactive and non-reactive unbalanced magnetron sputter deposition of TiN coatings. *Thin Solid Films* 2002;415:151–59.
- 25 Bhushan B. *Principles and applications of tribology*. New York: John Wiley & Sons; 1999.
- 26 Bull SJ, Rickerby DS. The abrasive wear resistance of sputter ion plated titanium nitride coatings. *Surf Coat Technol* 1988;36:743–54.
- 27 Wang Y, Hsu SM. Wear and wear transition mechanisms of ceramics. *Wear* 1996;195:112–22.
- 28 Rickerby DS, Burnett PJ. The wear and erosion resistance of hard PVD coatings. *Surf Coat Technol* 1987;33:191–211.
- 29 Hertzberg RW. *Deformation and fracture mechanics of engineering materials*. 4th ed. New York: John Wiley & Sons; 1996.

Publication II

Structure and Properties of CVD $\text{TiC}_x\text{N}_{1-x}$ Coatings

J. Wagner, C. Mitterer, M. Penoy, C. Michotte, W. Wallgram, M. Kathrein

Proceedings of the 16th International Plansee Seminar 2005

Structure and Properties of CVD $\text{TiC}_x\text{N}_{1-x}$ Coatings

J. Wagner*, C. Mitterer**, M. Penoy***, C. Michotte***, W. Wallgram****,
M. Kathrein****

* Materials Center Leoben Forschung Ges.m.b.H., Leoben, Austria

** Department of Physical Metallurgy and Materials Testing, University of Leoben, Austria

*** CERATIZIT Luxembourg S.à.r.l., Mamer, Luxembourg

**** CERATIZIT Austria Ges.m.b.H., Reutte, Austria

Summary

Titanium carbonitride ($\text{TiC}_x\text{N}_{1-x}$) coatings have been deposited by atmospheric pressure chemical vapor deposition (APCVD) from the system $\text{TiCl}_4\text{-CH}_4\text{-N}_2\text{-H}_2$. The influence of the deposition temperature and partial pressure of CH_4 and N_2 was characterized with respect to coating composition, microstructure, and microhardness. Special emphasis was laid on the investigation of the influence of coating composition on tribological properties. Dry sliding experiments between room temperature and 600°C were conducted in ambient air against alumina using a high-temperature ball-on-disc tribometer. The transfer layers after testing have been characterized by optical microscopy, optical profilometry, and Raman spectroscopy. Moreover, the degree of oxidation after high temperature testing was examined on fracture cross-sections using scanning electron microscopy. The carbon content x in $\text{TiC}_x\text{N}_{1-x}$ coatings increases with the deposition temperature as well as CH_4 partial pressure. The friction coefficient shows a high dependency on the carbon content both at room temperature as well as high temperatures. An increase of the carbon content at room temperature reduces the friction coefficient from 0.74 to a minimum of 0.15 for intermediate carbon concentrations and finally increases to 0.20 for carbon-rich coatings. In case of tribometer experiments at 500°C , the friction coefficient steadily decreases from 0.63 to 0.26 with increasing carbon contents. The low friction values can be explained by the in-situ formation of a lubricious carbon layer due to tribochemical reactions in the sliding contact zone.

Keywords: CVD, Titanium carbonitride, Hardness, Tribology, Friction, Oxidation, Raman spectroscopy

1 Introduction

Nowadays hard coatings deposited by thermal chemical vapor deposition (CVD) onto cemented carbide tools are complex multilayer composites of different coatings to accomplish the requirements of specific cutting applications. Especially, coatings on the basis of $\text{TiC}_x\text{N}_{1-x}$ ($0 \leq x \leq 1$) are standard components of multilayer structures due to beneficial properties like excellent adherence to cemented carbide, high hardness, and high toughness. The complete miscibility within the TiN-TiC quasibinary system

enables a gradual variation of the properties from the high toughness and good chemical stability of TiN to the high hardness and abrasion resistance of TiC [1,2].

The influence of deposition parameters such as temperature, gas composition, and total gas flow rate on structure of $\text{TiC}_x\text{N}_{1-x}$ coatings deposited in the $\text{TiCl}_4\text{-CH}_4\text{-N}_2\text{-H}_2$ system by thermal CVD have been extensively investigated (see for example ref. [3]), however, a comprehensive investigation on the influence of deposition parameters on microstructure, mechanical properties and, in particular, tribological properties is still missing. Thus, the aim of this work is the examination of the tribological behavior of $\text{TiC}_x\text{N}_{1-x}$ coatings evaluated by dry sliding experiments against alumina at temperatures from room temperature to 600°C. The results are discussed with respect to microstructure and coating composition as well as chemical and phase analysis in the wear track.

2 Experimental

$\text{TiC}_x\text{N}_{1-x}$ coatings were deposited in an atmospheric pressure CVD (APCVD) plant which has been described in detail in ref. [4] using TiCl_4 , H_2 , N_2 , CH_4 , and Ar as precursors. Coating composition and microstructure have been modified by varying both the CH_4 and N_2 partial pressure ($p_{\text{CH}_4}/(p_{\text{CH}_4}+p_{\text{N}_2})$ ratio) as well as the deposition temperature. The $p_{\text{CH}_4}/(p_{\text{CH}_4}+p_{\text{N}_2})$ ratio was altered between 0.27 and 0.64 while other gases and parameters like deposition temperature ($T_{\text{dep}} = 1000^\circ\text{C}$) and total gas flow were kept constant. Additionally, a temperature variation between 900 and 1050°C was performed for the particular $p_{\text{CH}_4}/(p_{\text{CH}_4}+p_{\text{N}_2})$ ratio of 0.46. The deposition time was adjusted to reach a final coating thickness of about 5 μm . The chemical composition and the dimension of the used cemented carbide substrates are listed in Table 1. A 0.5 μm TiN interlayer was deposited to minimize substrate influences on the investigated $\text{TiC}_x\text{N}_{1-x}$ coatings.

utilization	dimensions [mm]	chemical composition [wt.%]				
		Co	Cr ₃ C 2	TiC	(Ta,Nb)C	WC
hardness measurement	12×12×4	11	-	4	8	77
ball-on-disc tests	Ø 30×4	10	0.5	-	-	89.5

Table 1: Utilization, dimensions, and chemical composition of the substrates used in this study.

The tribological behavior was tested between 25 and 600°C in ambient air by dry sliding experiments using a CSM high-temperature ball-on-disc tribometer. The heating time was 2 h for all high-temperature tests. All experiments were performed using alumina balls with a diameter of 6 mm as counterparts and a normal load of 5 N. Details about

the test parameters are listed in Table 2. The relative humidity (r.h.) was 30(\pm 5) % for all tests with one exception (57 %).

temperature [°C]	number of laps	sliding distance [m]	radius [mm]	angular velocity [s ⁻¹]	linear velocity [m/s]
25	9549	300	5	2	0.10
	22736	1000	7	2	0.14
400	3183	100	5	2	0.10
500	3183	100	5	2	0.10
600	1592	50	5	2	0.10

Table 2: Testing parameters for ball-on-disc experiments.

All friction curves are illustrated in dependence on the number of laps¹⁾ and not the sliding distance, since different test radii were used. A 3D profiling system (Wyko NT1000) was used to investigate the wear tracks after ball-on-disc tests. Additionally, the wear track was investigated with light optical microscopy (LOM). Raman spectroscopy was performed to identify coating changes with a LabRam confocal-Raman spectrometer (Jobin-Yvon S.A.) equipped with an Nd-YAG laser (wavelength: 532.2 nm; power: 10 mW). The microhardness was evaluated with a computer-controlled microhardness tester (Fischerscope H100C) using a Vickers indenter and a continuously applied load of 30 mN. To minimize the influence of surface roughness on hardness measurement, the samples were polished with 1 μ m diamond paste before measurement. X-ray diffraction (XRD) analysis has been used to determine chemical composition of TiC_xN_{1-x} assuming complete miscibility within the TiN–TiC system. A Cambridge Instruments Stereoscan 360 scanning electron microscope (SEM) was used to characterize the coating morphology as well as to study fracture cross-sections of oxidized coatings. Additionally, the depth profiles of titanium, carbon, nitrogen, and oxygen were determined using a Jobin-Yvon Horiba JY10000RF glow discharge optical emission spectrometer (GDOES).

¹⁾ $number\ of\ laps = sliding\ distance / (2 \cdot \pi \cdot radius)$

3. Results and Discussion

3.1. Chemical Composition and Microstructure

The influence of deposition parameter on chemical composition of $\text{TiC}_x\text{N}_{1-x}$ coatings deposited on the ball-on-disc samples is shown in Fig. 1. The carbon content x increases with increasing CH_4 content in the deposition gas as illustrated in Fig. 1(a) for a constant deposition temperature T_{dep} of 1000°C . A higher carbon content can also be adjusted by increasing the deposition temperature as can be seen in Fig. 1(b) for a constant $p_{\text{CH}_4}/(p_{\text{CH}_4}+p_{\text{N}_2})$ ratio of 0.46, where the coating composition changes from $\text{TiC}_{0.14}\text{N}_{0.86}$ to $\text{TiC}_{0.71}\text{N}_{0.29}$ with an increase in deposition temperature from 900 to 1050°C . The rising carbon concentration in the coating results from the increasing reactivity of CH_4 [3].

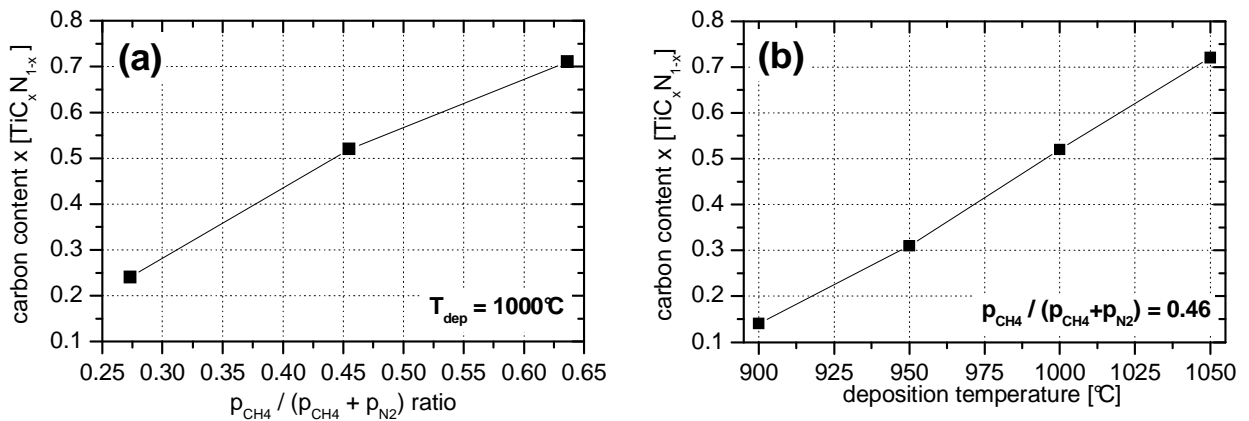


Fig. 1: Influence of (a) $p_{\text{CH}_4}/(p_{\text{CH}_4}+p_{\text{N}_2})$ ratio ($T_{\text{dep}} = 1000^\circ\text{C}$) and (b) deposition temperature ($p_{\text{CH}_4}/(p_{\text{CH}_4}+p_{\text{N}_2})=0.46$) on carbon content x in $\text{TiC}_x\text{N}_{1-x}$ coatings.

The surface structure of $\text{TiC}_x\text{N}_{1-x}$ coatings deposited at 1000°C with varying $p_{\text{CH}_4}/(p_{\text{CH}_4}+p_{\text{N}_2})$ ratios is shown in Fig. 2. The surface structure changes from smooth featureless to pyramidal structures for high $p_{\text{CH}_4}/(p_{\text{CH}_4}+p_{\text{N}_2})$ ratios and carbon contents in the coatings, respectively.

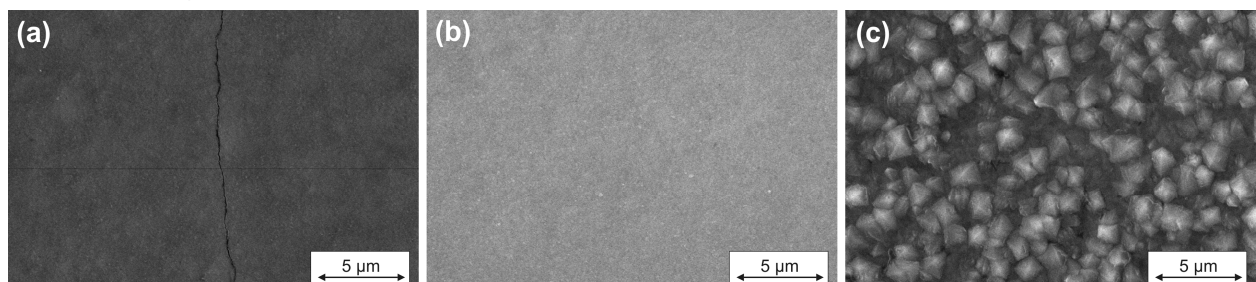


Fig. 2: SEM surface images of $\text{TiC}_x\text{N}_{1-x}$ coatings deposited at 1000°C and $p_{\text{CH}_4}/(p_{\text{CH}_4}+p_{\text{N}_2})$ ratios of (a) 0.27, (b) 0.46, and (c) 0.64.

The influence of deposition temperature on surface structure revealed similar structures for comparable carbon contents, i.e. smooth surfaces for intermediate carbon concentrations and pyramidal structures for high carbon containing coatings. In case of

low deposition temperatures and, consequently low carbon contents (cf. Fig. 1(b)), rough plate-like structures have been observed. The coarse structures at low temperatures are supposed to be the result of a low supersaturation. Since reactions between the precursors are thermally activated, higher deposition temperatures result in a higher supersaturation and, accordingly, in a higher nucleation density and a more fine-grained coating structure. In contrary, the mobility of the adsorbed species increases with increasing temperature and becomes the dominating structure-forming effect in case of high temperatures, thus resulting in coarse structures [5].

3.2 Mechanical Properties

The influence of deposition temperature and $p_{CH_4}/(p_{CH_4}+p_{N_2})$ ratio on coating microhardness is illustrated in Fig. 3 in dependence on the carbon content. Additionally, the microhardness of TiN is displayed. The hardness of TiC_xN_{1-x} coatings is expected to generally increase with the carbon content x since the amount of covalent bonding of the coating increases as nitrogen is replaced by carbon. In case of a constant deposition temperature of $1000^\circ C$, i.e. a variation of the $p_{CH_4}/(p_{CH_4}+p_{N_2})$ ratio, a linear behavior can be observed while the variation of the deposition temperature results in deviations from this behavior. Lower deposition temperatures resulted in higher hardness than expected from the linear behavior observed for $T_{dep} = 1000^\circ C$, whereas a lower hardness was found for the coating deposited at $1050^\circ C$. It is supposed that beside the intrinsic hardness of TiC_xN_{1-x} coatings, also the microstructure significantly influences their hardness. Grain size, porosity as well as the texture are known to highly affect the hardness of CVD coatings [6].

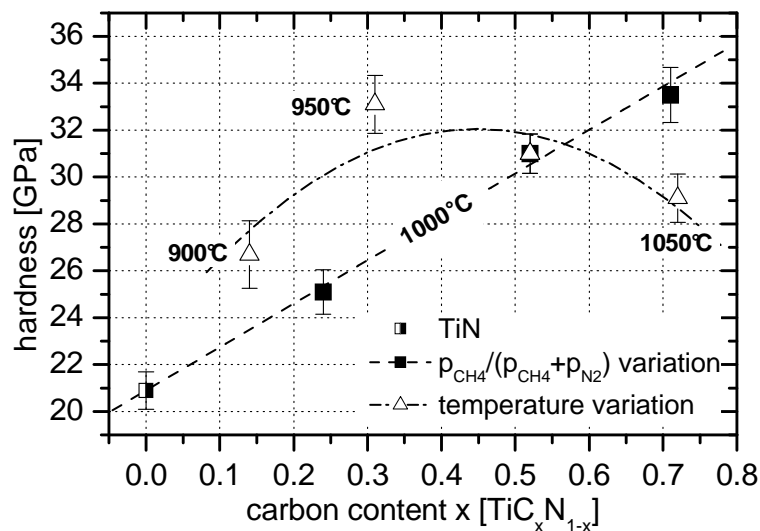


Fig. 3: Influence of the carbon content and deposition parameters on hardness of TiC_xN_{1-x} coatings.

3.3. Tribological Properties

3.3.1. Room Temperature

Fig. 4 shows the friction curves of $\text{TiC}_x\text{N}_{1-x}$ coatings with different carbon contents x as well as the corresponding 3D- and 2D-images of the wear tracks in dependence on the number of tested laps. The tribological behavior after 9549 laps is illustrated in Fig. 4(a)-(c). The high surface roughness and the resultant low reflectivity of light of coating $\text{Ti}_{0.14}\text{N}_{0.86}$ prevented an exact measurement of the wear volume with the optical profiler. Differences in the running-in period, final friction coefficient as well as depth of the wear tracks can be observed for the different x ratios, where the low carbon containing coating $\text{TiC}_{0.14}\text{N}_{0.86}$ yields the highest friction coefficient of about 0.74 at the end of the test.

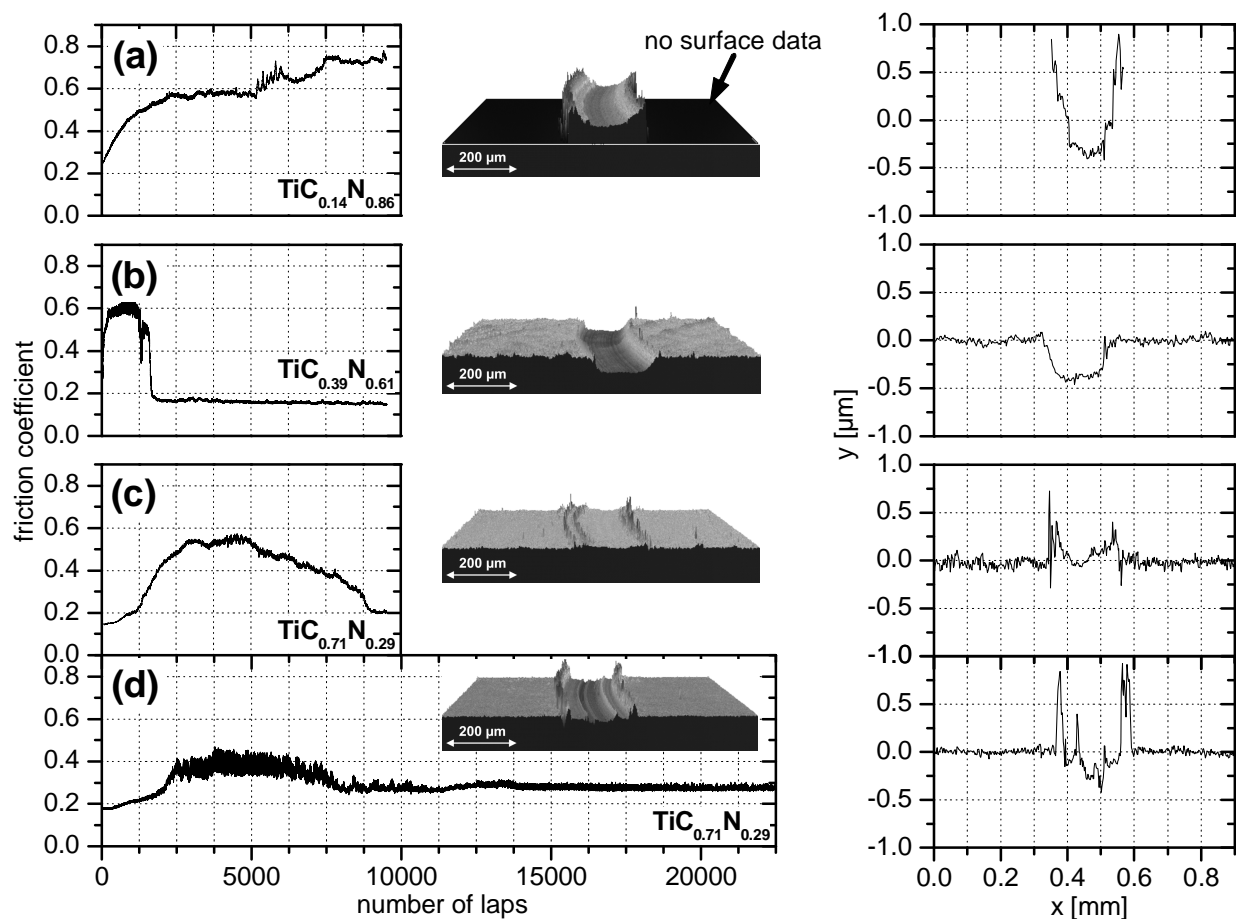


Fig. 4: Friction curves, 3D-, and 2D-images of the wear tracks: (a) $\text{TiC}_{0.14}\text{N}_{0.86}$, (b) $\text{TiC}_{0.39}\text{N}_{0.61}$, (c) $\text{TiC}_{0.71}\text{N}_{0.29}$ for 9549 laps, and (d) $\text{TiC}_{0.71}\text{N}_{0.29}$ for 22736 laps.

The steady-state friction coefficient is significantly lower for coatings with higher carbon concentrations. After a short running-in period, a constant friction coefficient of 0.15 can be observed for $\text{TiC}_{0.39}\text{N}_{0.61}$ (Fig. 4(b)). Coating $\text{TiC}_{0.71}\text{N}_{0.39}$ shows a slightly higher friction coefficient of 0.20 at the end of the test and a longer running-in stage (Fig. 4(c)). Considering the wear tracks in Fig. 4, the depth decreases with increasing carbon

content, where a wear track depth of 0.4 – 0.6 μm was estimated for the coating in Fig. 4(a). For the carbon-rich coating $\text{TiC}_{0.71}\text{N}_{0.29}$ essentially only a smoothing of the surface roughness can be observed after 9549 laps (see Fig. 4(c)), therefore, the specimen was also tested with 22736 laps (see Fig. 4(d)) to yield significant wear. The number of laps to reach the steady-state friction coefficient is similar to the test with 9549 laps, nevertheless, the resultant final friction coefficient of 0.27 is higher. Differences in relative humidity are assumed to be the reason for the different friction coefficients. The higher friction coefficient ($\mu = 0.27$) was measured for a lower relative humidity (r.h. = 25 %), while a high relative humidity of 55 % resulted in lower friction ($\mu = 0.20$). The same tendency also has been observed for $\text{TiC}_x\text{N}_{1-x}$ coatings deposited by PVD [7]. The decreasing coating wear with increasing carbon content can be related to the increasing coating hardness (cf. Fig. 3), where a higher hardness results in an elevated resistance against abrasive wear. The running-in behavior can be attributed to the initial surface roughness where smoother coatings reach faster the steady-state friction coefficient.

Raman spectroscopy was performed on the specimens shown in Fig. 4. In case of coating $\text{TiC}_{0.71}\text{N}_{0.29}$ the sample tested with 22736 laps was investigated in detail. Light optical micrographs and Raman spectra of both surface and wear track are shown Fig. 5. The Raman spectra are displayed separately for different wavenumber regions since the possibly formation of oxides generated during the wear process can be identified in the low Raman wavenumber range ($125\text{...}1000\text{ cm}^{-1}$), while bands of graphite and amorphous carbon can be detected at wavenumbers above 1000 cm^{-1} . The position of the bands of anatase and rutile, the metastable and stable polymorph of TiO_2 , respectively, are also displayed in the spectra [8]. Additionally, the four band positions of amorphous carbon, labeled as D_1 , D_2 , G_1 , and G_2 are shown, where D refers to “Disorder” due to finite size effects of amorphous carbon, and the G bands to “Graphite” representing the graphitic structure [9,10]. The spectra of the as-deposited coatings revealed no significant amount of amorphous carbon. The area investigated in the wear track is indicated by an arrow. The wear track of coating $\text{TiC}_{0.14}\text{N}_{0.86}$ shows high amounts of transfer material and Raman investigations of the transfer material reveal the formation of anatase and rutile as well as the formation of amorphous carbon (Fig. 5(a)). No oxidation products or amorphous carbon could be detected in the regions between the transfer material areas. In case of the higher carbon containing coating $\text{TiC}_{0.39}\text{N}_{0.61}$ a smooth polished wear track can be seen (Fig. 5(b)). Raman spectroscopy of the wear track revealed slight amounts of rutile and the formation of amorphous carbon.

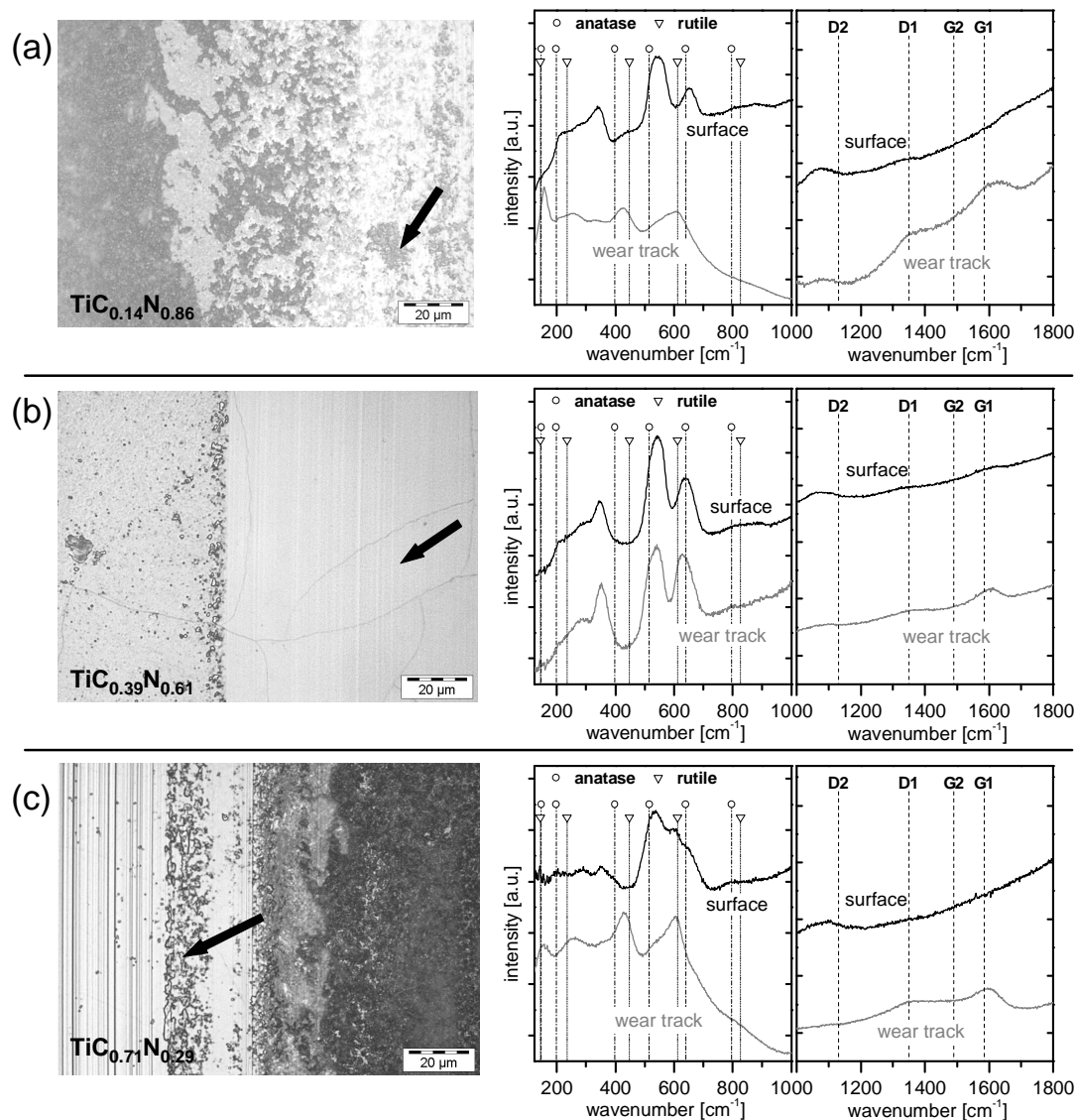


Fig. 5: LOM micrographs of the wear tracks and corresponding Raman spectra of the surface and the wear track: (a) $\text{TiC}_{0.14}\text{N}_{0.86}$ (9549 laps), (b) $\text{TiC}_{0.39}\text{N}_{0.61}$ (9549 laps), and (c) $\text{TiC}_{0.71}\text{N}_{0.39}$ (22736 laps).

The carbon-rich coating $\text{TiC}_{0.71}\text{N}_{0.29}$ exhibits a wear behavior in between the two described above. Raman investigations of wear debris show the formation of mainly rutile and amorphous carbon (Fig. 5(c)). However, no oxidation products could be detected aside from the wear debris. The ratio of the intensities of the amorphous carbon bands $(I_{D1}+I_{D2})/(I_{G1}+I_{G2}) = I_D/I_G$ can give information about the amount of disorder [11]. The analysis of the amorphous carbon bands observed for the wear tracks in Fig. 5 reveals that the I_D/I_G increases from 0.49 for coating $\text{TiC}_{0.14}\text{N}_{0.86}$ to 0.77 for $\text{TiC}_{0.39}\text{N}_{0.61}$, and decreases to 0.61 in case of the high-carbon containing coating.

Comparing the friction coefficients of Fig. 4 with the results of the Raman measurements, it can be assumed that the low friction coefficient of 0.15 is related to the presence of a continuous film of highly distorted amorphous carbon between coating and alumina counterpart which acts as lubricant. However, the formation of a continuous film is supposed to be dependent on two factors: the total amount of carbon

in the coating as well as the rate of tribo-oxidation. For low carbon containing coatings (i.e. $\text{TiC}_{0.14}\text{N}_{0.86}$) the carbon concentration is too low to form a continuous carbon layer and, consequently, carbon was only detected in the transfer material. In case of high carbon contents (i.e. $\text{TiC}_{0.71}\text{N}_{0.29}$) the high wear resistance and low tendency of tribo-oxidation prevents the formation of a continuous lubrication film of amorphous carbon. Moreover, the amount of disorder of the detected amorphous carbon reveals a correlation with the friction coefficient, thus explaining the lowest value obtained for the $\text{TiC}_{0.39}\text{N}_{0.61}$ coating.

3.3.2. High Temperature

The friction curves obtained in ball-on-disc tests at 500°C are shown in Fig. 6.

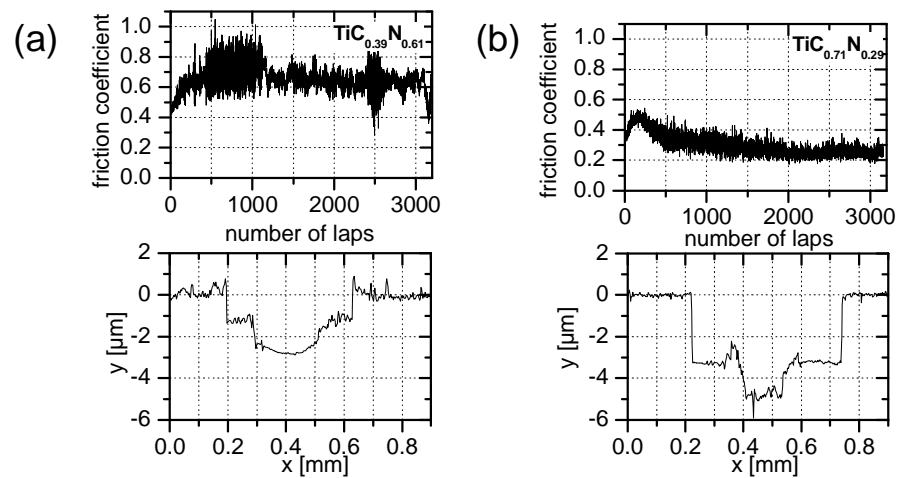


Fig. 6: Friction curves and 2D images of the wear tracks of ball-on-disc tests at 500°C and 3183 laps against alumina: (a) $\text{TiC}_{0.39}\text{N}_{0.61}$ and (b) $\text{TiC}_{0.71}\text{N}_{0.29}$.

A friction coefficient of 0.66 can be observed in Fig. 6(a) for coating $\text{TiC}_{0.39}\text{N}_{0.61}$ while the carbon-rich coating $\text{TiC}_{0.71}\text{N}_{0.29}$ yields a significant lower friction coefficient of 0.26 (Fig. 6(b)). The 2D optical images of the wear tracks reveal sharp steps in the wear tracks and, in contrary to the room temperature tests (see Fig. 4), the wear track depth increases with increasing carbon content. The corresponding Raman spectra measured in the center of the wear track are shown in Fig. 7. In case of coating $\text{TiC}_{0.39}\text{N}_{0.61}$ (Fig. 7(a)) yielding the highest friction coefficient, the spectrum mainly shows bands of the as-deposited coating (cf. Fig. 5) and bands of anatase with low intensity. Moreover, only small traces of amorphous carbon can be detected.

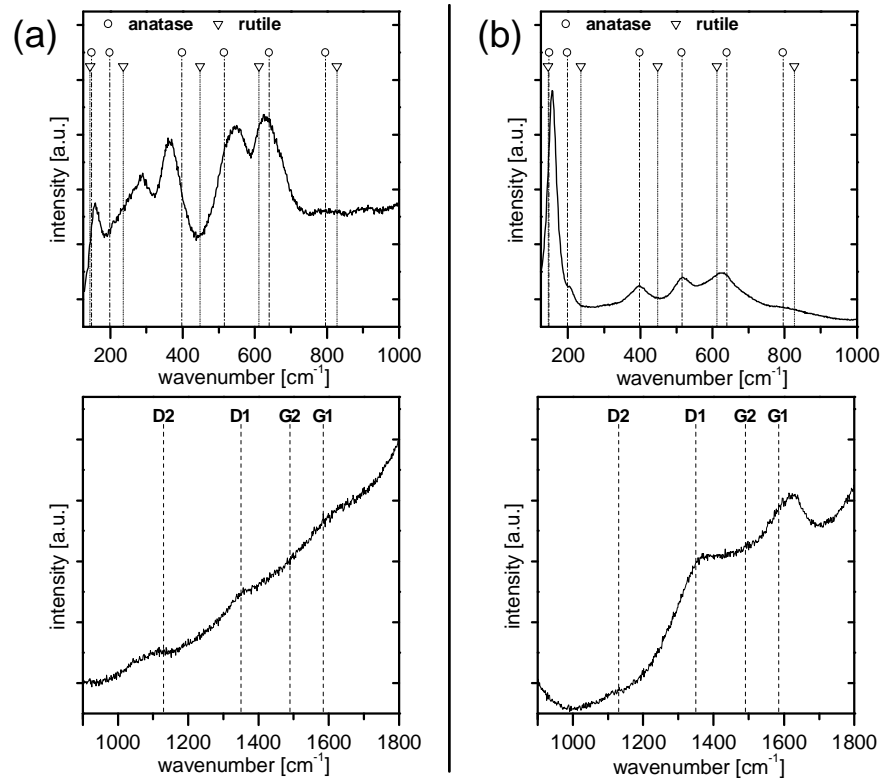


Fig. 7: Raman spectra of the wear tracks shown in Fig. 6: (a) $\text{TiC}_{0.39}\text{N}_{0.61}$ and (b) $\text{TiC}_{0.71}\text{N}_{0.29}$.

A different behavior can be seen in case of the high carbon and low friction coating $\text{TiC}_{0.71}\text{N}_{0.29}$ (see Fig. 7(b)). The spectrum yields bands of both anatase as well as rutile, and additionally, the bands of amorphous carbon can be observed with high intensity. The release of amorphous carbon during oxidation has also been observed for TiC [12]. It is assumed that the different friction coefficients of Fig. 6 are the result of differences in the oxidation behavior where the oxidation resistance generally decreases with increasing carbon content [13]. It is assumed that in case of the lower carbon content of $\text{TiC}_{0.39}\text{N}_{0.71}$ a slower oxidation takes place and most of the released carbon oxidizes to CO and CO_2 since no significant amounts of carbon were detected in the wear track. For the higher carbon content ($\text{TiC}_{0.71}\text{N}_{0.29}$), a more rapid oxidation process takes place and enough carbon is supposed to be available to form a lubricous film, although some carbon oxidation will occur as well. The influence of temperature was investigated in detail for specimen $\text{TiC}_{0.71}\text{N}_{0.29}$ yielding the lowest friction coefficient at 500°C. The coating was tested at 400 and 600°C and the results are shown in Fig. 8.

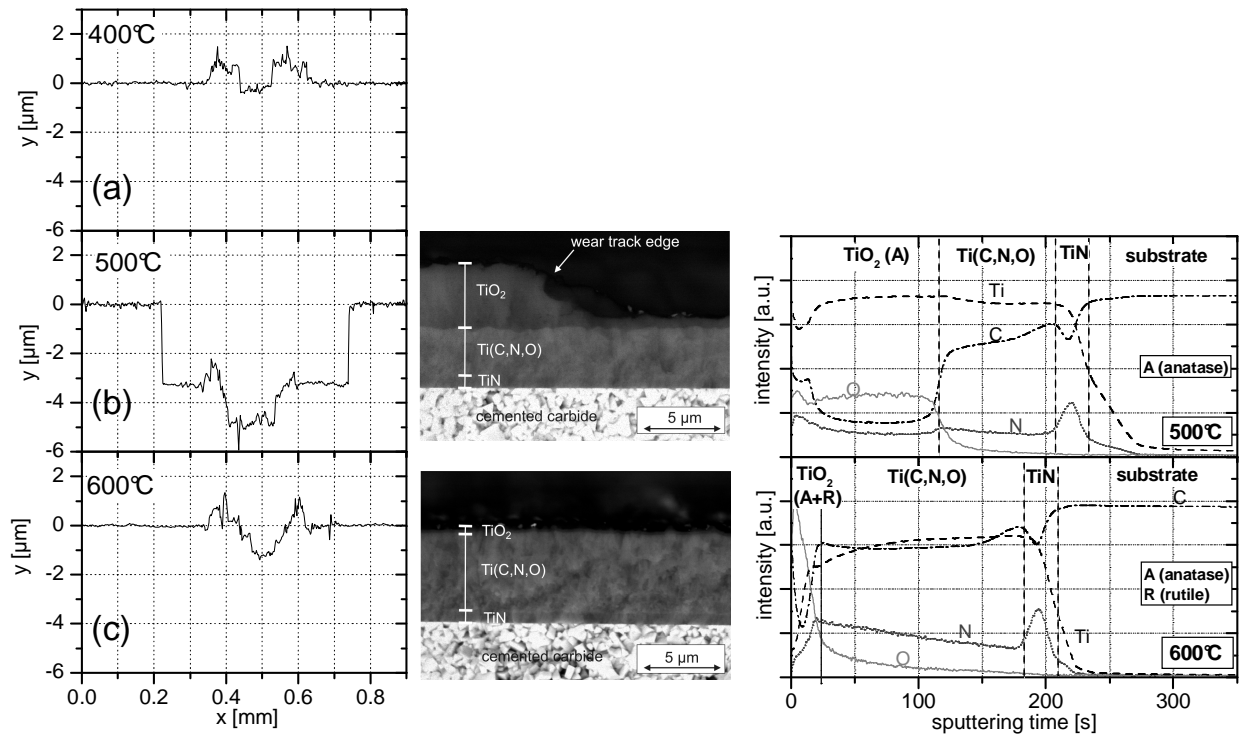


Fig. 8: 2D optical images, SEM fracture cross-sections, and GDOES depth profiles of coating $\text{TiC}_{0.71}\text{N}_{0.29}$ tested at (a) 400°C and 3160 laps, (b) 500°C and 3183 laps, (c) 600°C and 1592 laps.

The 2D images show a remarkable increase in coating wear as the testing temperature is increased from 400°C (Fig. 8(a)) to 500°C (Fig. 8(b)), whereas a significant decrease in coating wear can be observed for the sample tested at 600°C (Fig. 8(c)) which can not only be explained by the reduced number of laps. The backscattering detector image of the SEM fracture cross-section of the sample tested at 500°C in Fig. 8(b) shows the edge of the wear track also observed in the 2D optical profiler image. A distinctive interface can be seen within the coating. The corresponding GDOES measurements yield the formation of an oxide layer followed by a gradual decrease of the oxygen content. A completely different behavior can be seen in Fig. 8(c) where only a very thin oxide layer can be detected in both SEM fracture cross-section and GDOES measurements. Comparing the oxygen depth profile of both samples, a much higher concentration can be seen at the 600°C sample followed by a sharp drop, while a lower oxygen content and a less pronounced drop can be seen in the 500°C sample. Raman measurements of the samples oxidized at 500 and 600°C are shown in Fig. 9. In case of the sample oxidized at 500°C, only anatase can be detected while the formation of anatase and rutile can be observed for the coating oxidized at 600°C. It is supposed that for the coating oxidized at 600°C a more dense oxide layer forms retarding the progress in coating oxidation in comparison to the oxidation at 500°C, which is also evidenced by the sharp drop in the oxygen depth profile. The reason might be the different composition of the oxide layer. A similar change in oxidation kinetics and

concentration of anatase and rutile with temperature has also been reported for TiC [14].

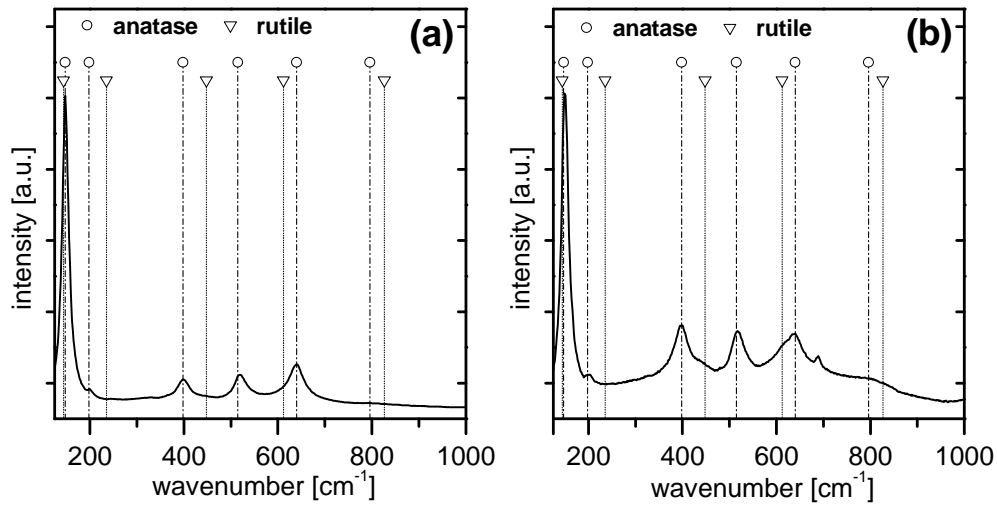


Fig. 9: Raman spectra of the coating surface of sample $\text{TiC}_{0.71}\text{N}_{0.29}$ oxidized at (a) 500°C and (b) 600°C.

The friction behavior for the carbon-rich coating $\text{TiC}_{0.71}\text{N}_{0.29}$ was almost the same at 400 and 500°C where friction coefficients of 0.26 and 0.27, respectively, were observed. The friction coefficient increased to 0.40 for a testing temperature of 600°C. Raman spectroscopy of the transfer material revealed highly oxidized coating material and amorphous carbon for the sample tested at 400°C. Also for 600°C free carbon was detected. However, it is supposed that a substantial oxidation process also takes place after finishing the ball-on-disc test and during cooling down to room temperature, both results in amorphous carbon formation.

4 Conclusions

The chemical composition and microstructure of APCVD coatings was adjusted by varying the deposition temperature between 900 and 1050°C and changing the partial pressures of CH_4 and N_2 . Both higher deposition temperature and partial pressures of CH_4 resulted in higher carbon concentrations in the coatings. The coatings were characterized with respect to the microhardness and their tribological properties in ambient air at room temperature and up to 600°C.

At room temperature the coating wear decreases with increasing carbon content which could be related to the increasing microhardness. The friction coefficient remarkably depends on the carbon concentration in the coating and drops from a value of $\mu = 0.74$ for low carbon containing coatings ($\text{TiC}_{0.14}\text{N}_{0.86}$) to a minimum of $\mu = 0.15$ for $\text{TiC}_{0.39}\text{N}_{0.61}$, while a further increase of the amount of carbon increased the friction coefficient to values between 0.20 and 0.27. The dependency on the carbon content in the coating could be attributed to the formation of highly disordered amorphous carbon which is supposed to act as lubricant. The carbon is released due to tribo-oxidative reactions in the wear track. The amount of carbon formed is considered to depend on

the carbon concentration in the coating as well as on the wear resistance because a certain amount of wear is expected to be necessary to release a sufficient amount of carbon. Moreover, the humidity also influences the carbon formation.

At 500°C a considerable amount of coating oxidation can be observed after the ball-on-disc tests. The extent of oxidation can be contributed to the decreasing oxidation resistance with increasing carbon content. The oxidation rate is lower for both 400°C and 600°C compared to 500°C. The peculiar behavior at 600°C is the result of a change in oxidation kinetics due to differences in the composition of the oxide layer and the formation of a more dense oxide layer. The friction coefficients decrease with increasing carbon concentration in the coatings due to the changing oxidation resistance, where the oxidation process releases amorphous carbon as in case of room temperature tests. Higher testing temperatures result in higher friction coefficients, and it is assumed that the carbon film oxidizes more rapidly with increasing temperature, thus, a lower amount of carbon is available to act as lubricant.

The present work gives a comprehensive overview about the relations between coating composition, microstructure, and microhardness and the influence on the tribological behavior of CVD deposited $\text{TiC}_x\text{N}_{1-x}$ coatings. The results provide as basis for a further development of CVD $\text{TiC}_x\text{N}_{1-x}$ coatings.

Acknowledgments

Financial support of this work by the Technologie Impulse Ges.m.b.H. in the frame of the K-plus competence centre program is highly acknowledged. The authors are very grateful to DI Kerstin Kutschej and Dr. Gerardo Fontalvo for valuable discussions.

References

- 1 W. Schintlmeister, O. Pacher, J. Kanz, K. Gigl, *Wear* 100 (1984) 153.
- 2 M. Kathrein, W. Schintlmeister, W. Wallgram, U. Schleinkofer, *Surf. Coat. Technol.* 163-164 (2003) 181.
- 3 Duen-Jen Cheng, Wen-Pin Sun, Min Hsiung Hon, *Thin Solid Films* 146 (1987) 45.
- 4 W. Schintlmeister, W. Wallgram, J. Kanz, *Thin Solid Films* 107 (1983) 117.
- 5 J. M. Blocher, jr., *J. Vac. Sci. Technol.* 11(4) (1974) 680.
- 6 Hsyi-En Cheng, Yao-Wei Wen, *Surf. Coat. Technol.* 179 (2004) 103.
- 7 R. Rodríguez, J.A. García, A. Medrano, M. Rico, R. Sánchez, R. Martínez, C. Labrugère, M. Lahaye, A. Guette, *Vacuum* 67 (2002) 559.
- 8 U. Balachandran, N.G. Eror, *J. Solid State Chem.* 42 (1982) 276.
- 9 B. Oral, R. Hauert, U. Müller, K.-H. Ernst, *Diamond Relat. Mat.* 4 (1995) 482.

-
- 10 T. Zehnder, P. Schwaller, F. Munnik, S. Mikhailov, J. Patscheider, J. Appl. Phys. 95(8) (2004) 4327.
 - 11 A. Cuesta, P. Dhamelinourt, J. Laureyns, A. Martínez-Alonso, J. M. D. Tascón, J. Mater. Chem. 8 (1998) 2875.
 - 12 S. Shimada, J. Ceram. Soc. Jap. 109(3) (2001) 33.
 - 13 A. Mitsuo, S. Uchida, N. Nihira, M. Iwaki, Surf. Coat. Technol. 103-104 (1998) 98.
 - 14 V.A. Zhilyaev, V.D. Lyubimov, Inorg. Mat. 10(1) (1974) 47.

Publication III

The influence of boron content on the tribological performance of Ti–N–B coatings prepared by thermal CVD

**J. Wagner, D. Hochauer, C. Mitterer, M. Penoy, C. Michotte,
W. Wallgram, M. Kathrein**

Surface & Coatings Technology 201 (2006) 4247–4252

The influence of boron content on the tribological performance of Ti–N–B coatings prepared by thermal CVD

J. Wagner^a, D. Hochauer^a, C. Mitterer^b, M. Penoy^c, C. Michotte^c,
W. Wallgram^d, M. Kathrein^d

^{a)} *Materials Center Leoben Forschung GmbH, Franz-Josef-Strasse 13, A-8700 Leoben, Austria*

^{b)} *Department of Physical Metallurgy and Materials Testing, University of Leoben,
Franz-Josef-Strasse 18, A-8700 Leoben, Austria*

^{c)} *CERATIZIT Luxembourg S.à.r.l., L-8201 Mamer, Luxembourg*

^{d)} *CERATIZIT Austria GmbH, A-6600 Reutte, Austria*

Abstract

In this work, Ti–N–B coatings have been deposited by thermal chemical vapor deposition (CVD). The effect of boron varying between 0 and 35.1 at.% on coating structure, mechanical and tribological properties was investigated. The coatings reveal a dual-phase structure of TiN and TiB₂ above 1 at.% B. The addition of boron causes grain refinement and changes the structure from columnar for TiN to fine-crystalline. Coating hardness increases continuously from 20 GPa for TiN to 45 GPa at 35.1 at.% B. Ball-on-disc tests against alumina were conducted at 25, 500 and 600°C. At 25°C the friction coefficients increase from 0.75 for TiN to about 1.0 for boron contents up to 13.1 at.%, while values down to 0.26 were measured at 35.1 at.% B. The friction coefficients at 500 and 600°C increase from 0.55 for TiN to 0.8 – 1.0 for the highest boron content. At 25°C the lowest wear rates were obtained for the highest boron contents, while the opposite behavior was found for 500 and 600°C. Extensive coating oxidation resulted in the highest wear rate at 500°C for 35.1 at.% B, but the wear resistance improved at 600°C. Raman spectroscopy of the oxide layer revealed the preferred formation of anatase at the expense of rutile for high boron concentrations.

Keywords: Chemical vapor deposition (CVD); Titanium boronitride; Structure; Friction; Wear; Raman

1 Introduction

The diversity of cutting operations entails different requirements on coatings to meet an optimum performance. Multi-phase structures allow the optimization of coatings with respect to specific cutting requirements [1,2]. The different phases within the ternary system Ti–B–N offer the possibility to deposit wear resistant films within a wide range of properties [3,4]. Many studies have been performed with this coating system synthesized by physical vapor deposition (PVD) [5,6] and plasma-assisted chemical vapor deposition (PACVD) [7-9]. Although the deposition of Ti–B–N coatings by thermal

CVD is well-established in cutting tool production [10,11], only little work has been published. The deposition of Ti–B–N coatings in a high-temperature CVD processes between 1050 and 1500°C has shown the formation of TiB₂ and/or cubic titanium boronitride phases [12,13]. However, such high temperatures are not applicable to cemented carbide cutting inserts because of degeneration of the WC/Co substrate and formation of a brittle CoWB phase [14]. The investigation of single- and multi-layer coatings deposited at lower temperatures (850 – 1050°C) has only revealed the formation of TiN and TiB₂ where the coating composition was varied from TiN to pure TiB₂ [15,16].

Requirements on hard coatings for cutting tools are, for example high hardness, chemical inertness and a dense fine-grained microstructure [1,17]. Boron is well-known for its grain refinement effect not only in metallurgical processes [18], but also in hard coatings [6]. Regarding hardness and oxidation resistance of Ti–B–N coatings, the formation of high amounts of TiB₂ would be favorable due to its superior properties compared to, e.g. TiN. However, at the same time TiB₂ shows a lower chemical stability in contact with steel compared to TiN [19]. For these reasons, Ti–B–N coatings deposited by thermal CVD with an utmost concentrations of 35.1 at.% B are investigated in this study. Special emphasize is laid on the influence of small contents below 3 at.% to study grain refinement and the first appearance of a dual-phase structure; therefore, we refer to our films as Ti–N–B.

2 Experimental

Coating deposition was performed in a commercial hot-wall CVD reactor [20] at atmospheric pressure using TiCl₄, BCl₃, N₂, H₂, and Ar. To study the influence of small boron contents on coating properties, the BCl₃ partial pressure $p(\text{BCl}_3)$ was varied between 0 and 191 Pa at a constant deposition temperature T_{dep} of 950°C. The influence of T_{dep} on film growth was examined between 850 and 1000°C for a medium $p(\text{BCl}_3)$ of 143 Pa. Ti–N–B coatings of 5 ± 1.5 µm thickness were obtained.

Two different cemented carbide grades were used as substrates. For hardness, glancing angle X-ray diffraction (GAXRD), and glow discharge optical emission spectroscopy (GDOES) measurements, polished cutting inserts (77 wt.% WC, 11 wt.% Co, 4 wt.% TiC, 8 wt.% (Ta,Nb)C) were utilized. Tribological tests were performed on polished discs (89.5 wt.% WC, 10 wt.% Co, 0.5 wt.% Cr₃C₂). To reduce coating/substrate interactions, a 0.5 µm TiN interlayer was deposited prior to the Ti–N–B films. The tribological behavior was tested by dry-sliding tests at 25, 500 and 600°C against alumina balls (Ø6 mm) using a CSM high-temperature ball-on-disc tribometer. The tests were performed in ambient air with a relative humidity of 35 ± 5 %. Normal load, sliding speed, and heating time for high-temperature experiments were constant at 5 N, 0.1 m/s and 2 h, respectively. The wear-track-radius/sliding-distance

combination and the corresponding number of cycles was not identical for all temperatures. At 25°C, a combination of 7 mm/700 m (15,915 cycles) was used for all specimens. Since no steady-state friction coefficient was obtained after 15915 cycles for the coating with the highest boron content, the sample was also tested with 47,730 cycles (5 mm/1500 m) and 106000 cycles (9 mm/6000 m). For 500 and 600°C, the pairing was 5 mm/500 m (15,915 cycles) for the coatings deposited within the T_{dep} variation, whereas coatings of the $p(BCl_3)$ series were tested more moderately with 5 mm/100 m (3183 cycles) due to a lower coating thickness.

A 3D profiling system (Wyko NT1000) was used to measure the wear volume after ball-on-disc testing. Additionally, the wear tracks were analyzed using grazing incidence reflection Fourier transform infrared (GIR-FTIR) spectroscopy (Bruker Hyperion 3000 FTIR microscope) with an incidence angle of 7°. The spectra were recorded within 4000 – 600 cm^{-1} . The coating composition was determined by GDOES (Jobin-Yvon Horiba JY10000RF). The crystallographic structure was assessed by GAXRD (incident angle: 3°) using Cu $K\alpha$ radiation and the residual stresses employing the $\sin^2\psi$ -method (Panalytical X'Pert Pro). The grain size was estimated from line-profile analysis using a Voigt function [21]. The microhardness HU_{pl} was evaluated on polished specimens with a computer-controlled microhardness tester (Fischerscope H100C) using a Vickers indenter (BK7 tip shape correction) [22]. Only load-independent values (typically between 40 and 80 mN) were considered. A Cambridge Instruments Stereoscan 360 scanning electron microscope (SEM) was used to study surface morphology, fracture cross-sections, and wear tracks. Raman spectroscopy was performed to identify coating changes using a Jobin-Yvon LabRam confocal-Raman spectrometer equipped with a Nd-YAG laser (wavelength: 532.2 nm; power: 10 mW).

3 Results and Discussion

Fig.1 shows the influence of $p(BCl_3)$ and T_{dep} on boron content and surface morphology of the coatings. The composition changes from pure TiN to 2.8 at.% B with increasing $p(BCl_3)$, whereas the impact of T_{dep} is more distinct resulting in an increase from 2.6 to 35.1 at.% B as T_{dep} decreases from 1000 to 850°C. According to the ternary Ti–B–N phase diagram, the compositions of all coatings are within the ternary phase field $TiB_2 + TiN + TiN_{1-x}$ close to the quasi-binary tie-line $TiN-TiB_2$ [3,23]. The SEM micrographs exhibit a change of the surface morphology from coarse faceted and compact for TiN to a coarse globular, and finally needle-like structure with increasing boron content. The considerable variation in composition with T_{dep} is also reflected in changes of the surface morphology shifting continuously from plate-like to smooth, fine-crystalline with decreasing T_{dep} .

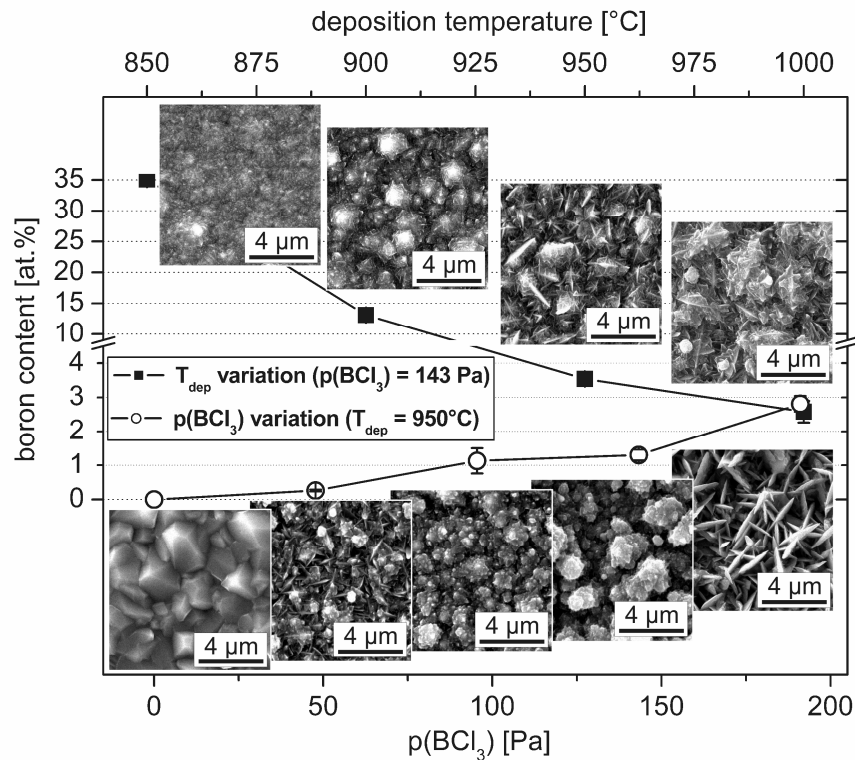


Fig. 1: Influence of deposition temperature T_{dep} and BCl_3 partial pressure $p(BCl_3)$ on the boron content in Ti-N-B coatings. The inserts show the corresponding SEM micrographs of the surface structure.

GAXRD patterns are shown in Fig. 2 for coatings of the $p(BCl_3)$ - and T_{dep} -variation series. The addition of 0.3 at.% B only results in a slight broadening of the TiN peaks. A small peak at $2\theta = 34.81^\circ$ indicates the formation of W_2CoB_2 at the interface due to boron diffusion into the substrate. This interfacial reaction could be also observed on etched polished cross-sections by light optical microscopy. Increasing the boron content to 1.1 at.% increases the broadening of the TiN peaks and, moreover, results in the formation of a new phase. The reflection at 34.59° can be attributed to the (100) reflection of hexagonal TiB_2 . Formation of TiB_2 and peak broadening continue for coatings deposited within the T_{dep} variation and for 35.1 at.% B, the GAXRD pattern is determined by broad overlapping peaks of TiN and TiB_2 . The broadening of XRD peaks is the result of smaller grains and/or higher lattice strains [24]. A change of the coating structure from columnar TiN to interrupted columns by the addition of small boron contents, and finally a fine-crystalline structure at the highest boron content could be observed at SEM fracture cross-sections confirming the XRD results. The TiB_2 peaks exhibit a shift to higher angles indicating a lower lattice constant. A similar behavior has been found for thermal CVD coatings, where a hexagonal structure close to TiB_2 but lower lattice parameter has been observed [12]. Tensile macro-stresses due to the thermal mismatch between coating and substrate may contribute partially to the observed peak shifts.

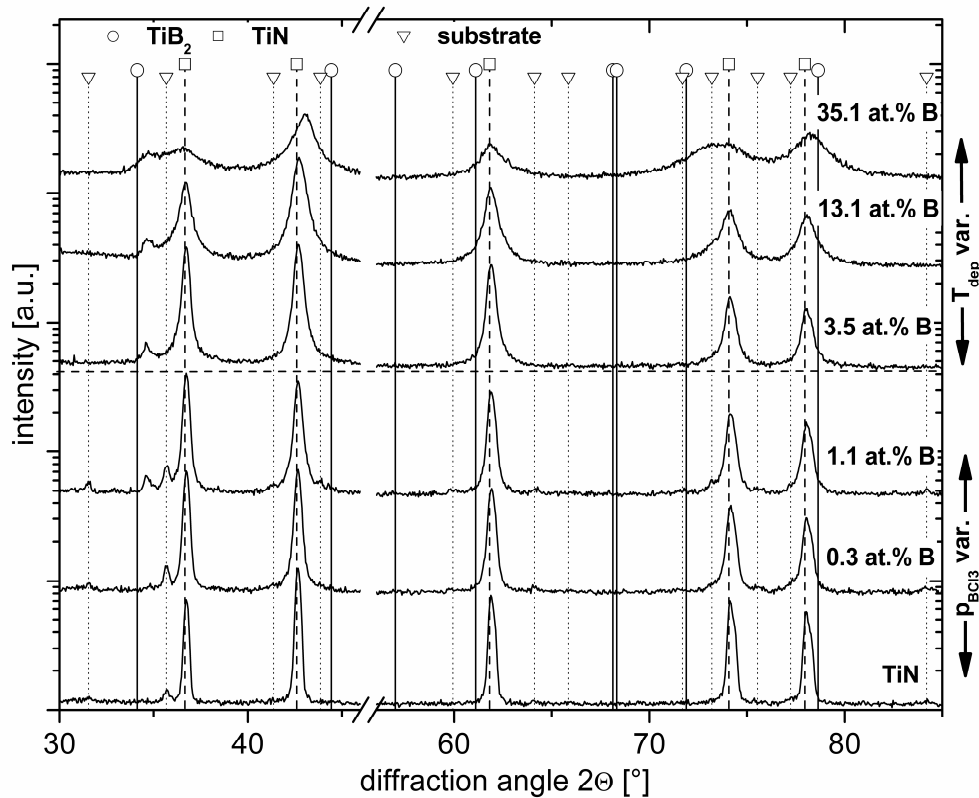


Fig. 2: GAXRD patterns of Ti–N–B coatings deposited within the $p(\text{BCl}_3)$ -variation (0 – 1.1 at.% B) and T_{dep} -variation (3.5 – 35.1 at.% B).

The coating hardness increases from 20 GPa for TiN to 27 GPa by the addition of only 0.3 at.% B. A further increase in boron results in a continuous hardness enhancement up to 45 GPa at 35.1 at.% B (see Fig. 3). The hardness increase can be attributed to the observed grain refinement as well as the increasing phase fraction of TiB_2 showing a higher hardness compared to TiN [2]. Differences between the two deposition series can be noticed at around 3 at.% B. The coating deposited at 950°C yields a higher hardness of 31 GPa compared to 26 GPa for the coating deposited at 1000°C. This difference in hardness is supposed to result from dissimilarities in grain size and residual stresses. The sample deposited at 950°C exhibits a smaller grain size (220 nm) and lower tensile stresses (420 MPa) compared to the sample deposited at 1000°C with larger grains (320 nm) and higher tensile stresses (520 MPa), where both a finer grain structure and lower tensile stresses favor a high hardness [25].

Fig. 4 shows the steady-state friction coefficient as a function of the boron content for the different testing temperatures. At 25°C, the friction coefficient increases from 0.75 for TiN to 1.0 – 1.1 by the addition of up to 3.5 at.% B. The higher friction coefficient can be related to the higher coating hardness (cf. Fig. 3). Moreover, the low boron containing coatings (< 3.5 at.% B) exhibit a high surface roughness often combined with a coarse, loosely-bonded surface structure (see Fig. 1). Thus, formation of coating wear debris during sliding is fostered and, hence, the friction coefficient increases. The

contribution of surface roughness and debris formation is also indicated by a higher scattering of the friction coefficient.

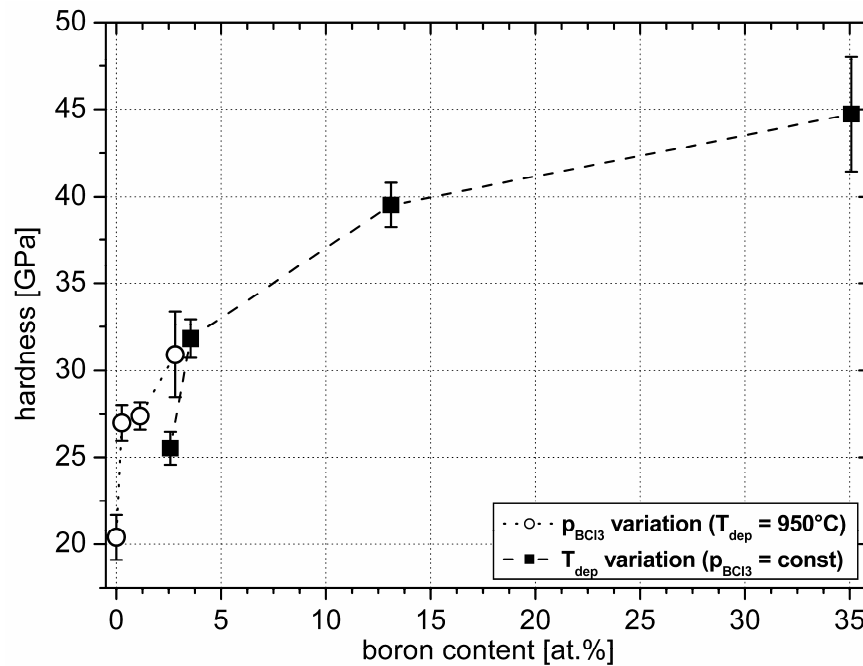


Fig. 3: Dependence of hardness of Ti–N–B coatings on the boron content.

For 13.1 at.% B, the surface roughness is lower and the friction coefficient decreases to 0.93. No steady-state friction coefficient could be obtained for 35.1 at.% B after 15,520 cycles, thus, the cycle number was increased to 47,730 and 106,000. Subsequent to an extensive running-in period of about 30,000 cycles, the tests revealed a friction coefficient of 0.47 and 0.26 after 47,730 and 106,000 cycles, respectively. The wear track yielding the lowest friction coefficient (0.26) was investigated by Raman- and GIR-FTIR spectroscopy for possible formation of a lubricating film. Within the system Ti–N–B, this film could be hexagonal-BN, but also the result of a tribo-chemical reaction in the contact zone, e.g. the formation of Magnéli phases Ti_nO_{2n-1} ($4 \leq n \leq 9$) or boric acid H_3BO_3 [26]. No indication for hexagonal-BN in the coating was found by GAXRD (cf. Fig. 2) nor by Raman- and GIR-FTIR spectroscopy in the wear track. Low friction values down to 0.2 have been reported for PACVD TiN [27] and TiBN [9] coatings caused by chlorine-induced formation of a lubricating rutile film. Within this study, no significant amounts of rutile were detected by Raman spectroscopy and less than 0.5 at.% Cl were measured. Moreover, no evidence for H_3BO_3 or B_2O_3 could be found by Raman- or GIR-FTIR-spectroscopy. The flash temperature in the contact zone appears to be too low for significant oxidation of TiB_2 and consecutive reaction of B_2O_3 with moisture to H_3BO_3 . The low friction values for 35.1 at.% B may originate from a lubrication mechanism where oxygen and moisture are involved, which gives rise to the formation of a very thin lubricating layer not detected by any of the employed methods.

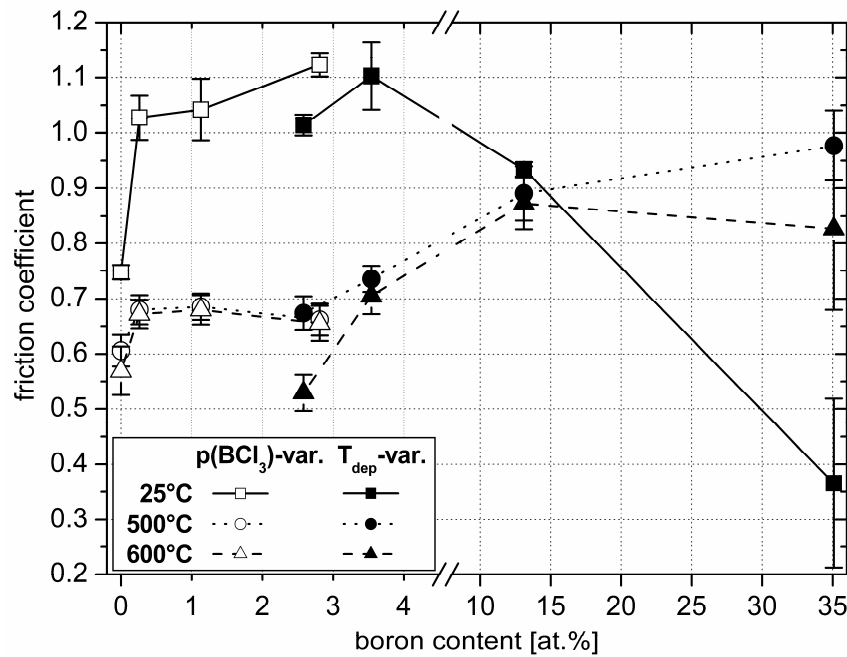


Fig. 4: Influence of the boron content on the friction coefficient at 25, 500, and 600°C.

The investigated Ti–N–B coatings show a comparable friction behavior at 500 and 600°C as can be seen in Fig. 4. The friction coefficient is lowest for TiN (0.55) and increases to 0.8 – 1.0 for the highest boron contents. The lower friction coefficient for the high-temperature tests can be attributed to coating oxidation, where a soft oxide layer acts as a lubricant. The rise in friction at 35.1 at.% B from values down to 0.26 at 25°C to friction coefficients above 0.8 at 500 and 600°C indicates the importance of moisture for the observed low friction values.

The influence of boron on the wear rate is shown in Fig. 5. High surface roughness of some coatings (cf. Fig. 1) combined with surface oxidation at high temperatures prevented the measurement of all wear rates by optical profilometry. The left section in Fig. 5 shows low boron containing coatings deposited within the $p(\text{BCl}_3)$ variation, while higher contents achieved at different temperatures are illustrated at the right side.

At 25°C, the wear rate increases from TiN by boron addition up to 3.5 at.%, whereas at higher concentrations the wear rate decreases significantly (see Fig. 5). Fig. 6 exhibits backscattered electron SEM images of the wear tracks of (a) TiN, (b) 0.3 at.% B, and (c) 35.1 at.% B. The inserts show a magnified view from the center of the wear track. The amount of oxidized material, i.e. the visible dark areas beside the wear track, increases from TiN (Fig. 6a) to 0.3 at.% B (Fig. 6b), and finally decreases for 35.1 at.% B (Fig. 6c) which corresponds with the observed wear rates. Also the wear tracks appear different revealing deep grooves for TiN that diminish with increasing boron content, whereas a crack network emerges. The wear rate changes are supposed to be the result of the influence of surface roughness, hardness, and toughness. TiN exhibits a rough, faceted but compact surface structure, whereas the coatings with low boron contents show

coarse, less adherent structures (cf. Fig. 1). Detachment of these loosely bonded coating particles increases the number of wear debris, intensifies coating wear, and therefore, increases the wear rate for low boron contents.

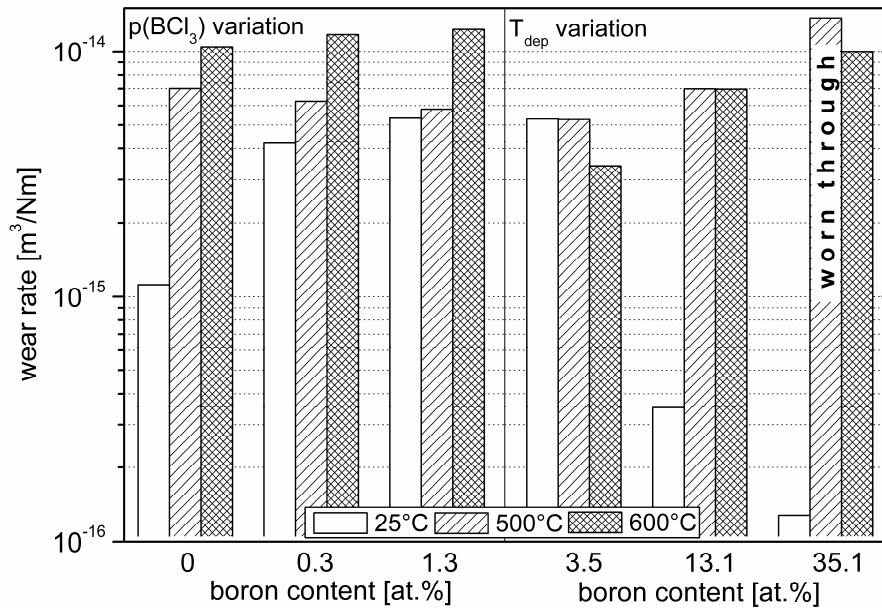


Fig. 5: Influence of the boron content on the wear rate of Ti-N-B coatings deposited within the $p(\text{BCl}_3)$ -variation (left) and the T_{dep} -variation (right) at testing temperatures of 25, 500, and 600°C.

Above 13.1 at.% B, smooth surfaces combined with the highest hardness and, thus, abrasion resistance [28], respectively, yield to the lowest wear rates. The changes in wear track appearance can be attributed to the coating hardness. The severe grooving for TiN results from the lower coating hardness and decreases as the hardness increases (cf. Fig. 3). Additionally, the width of the wear track enlarges with the coating hardness, since the wear of the counterpart increases, resulting in a flattening of the Al_2O_3 ball and, thus, a larger contact area. The observed crack networks indicate a decreasing fracture toughness, where the high density for 0.3 at.% B may result from the high friction coefficient causing high tensile stresses at the back edge of the contact during sliding which might contribute to an increased wear rate [28].

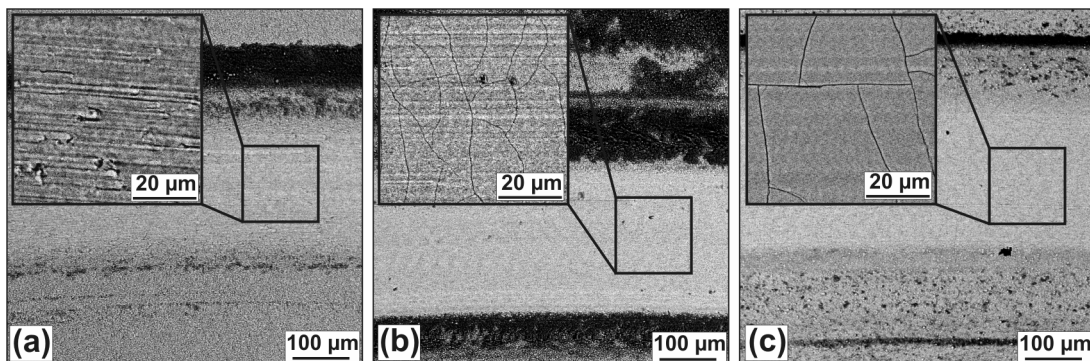


Fig. 6: SEM micrographs of the wear tracks of Ti-N-B coatings after ball-on-disc tests at 25°C containing (a) 0 at.%, (b) 0.3 at.% B, and (c) 35.1 at.% B.

At 500°C, the wear rate slightly decreases as the boron content rises up to 3.5 at.%. Higher concentrations result in the opposite trend with elevated wear rates causing even complete coating wear at 35.1 at.% B. Further increase of temperature to 600°C consequences higher wear rates compared to 500°C for low boron concentrations. Nevertheless, a completely opposite trend can be observed for high boron contents yielding comparable or even lower wear rates compared to 500°C. For instance, the sample with 35.1 at.% B which has been worn through at 500°C survived the test at 600°C.

The GDOES oxygen depth profiles of coatings with 0 at.% B (TiN), 13.1 at.% B, and 35.1 at.% B were measured after ball-on-disc tests at 500 and 600°C and are illustrated in Fig. 7. The depth profiles of TiN and 13.1 at.% B after 500°C are similar, whereas for 35.1 at.% B a significantly higher oxygen concentration at the surface can be observed. After 600°C tests, the profiles change and the amount of oxygen at the surface increases compared to 500°C, in particular for TiN but also for 13.1 at.% B. Conversely, the oxygen amount, still high, decreases for 35.1 at.% B as the temperature rises to 600°C. The oxidation resistance of TiB_2 is higher compared to TiN, and boron addition to TiN shifts the onset of oxidation to higher temperatures [29]. The reason for the observed opposite behavior might be the nature of the formed oxide layer. Raman spectroscopy was applied to examine the type of oxides, in particular, the formation of the metastable and stable polymorphs of TiO_2 anatase and rutile [30].

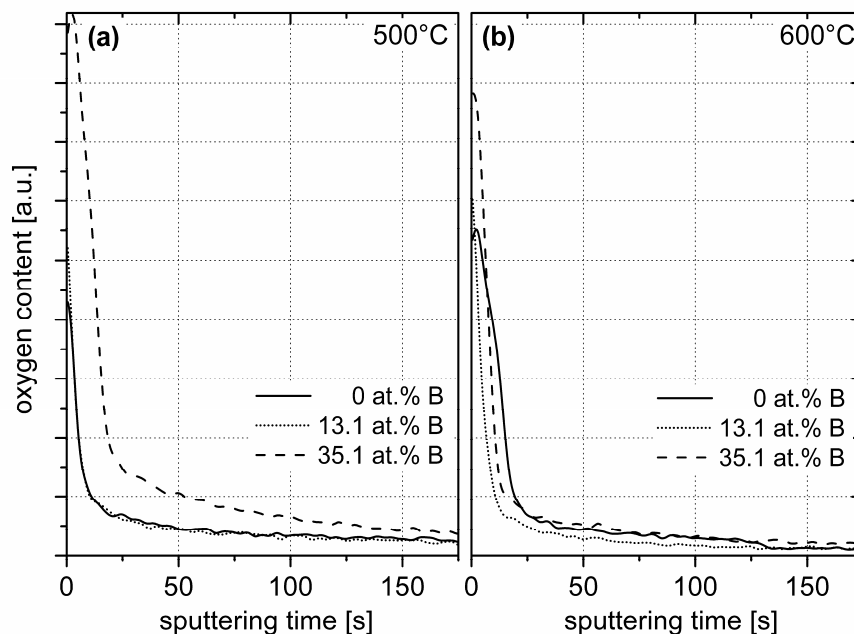


Fig. 7: GDOES oxygen depth profiles of Ti-N-B coatings with different boron contents after ball-on-disc tests at (a) 500°C and (b) 600°C.

The coatings oxidized at 500°C show a shift in composition from a mixture of anatase and rutile at 0 at.% B to an oxide layer of mainly anatase for 13.1 and 35.1 at.% B. An increase of temperature to 600°C favors the formation of stable rutile for all coatings,

especially, for TiN. The formation of rutile at the expense of anatase may reduce coating oxidation and a comparable change in oxidation has also been found for $\text{TiC}_x\text{N}_{1-x}$ coatings [31]. Although not detected by Raman spectroscopy, B_2O_3 formation may contribute to an enhanced oxidation resistance with increasing temperature. The onset of B_2O_3 formation during oxidation of TiB_2 has been reported to start at 600°C at the grain boundaries resulting in a densification of the structure and, thus, retarded oxidation progress [32]. A similar mechanism can be observed in yttrium doped coatings showing an enhanced oxidation resistance, where yttrium segregation to grain boundaries and subsequent YO_x formation inhibits cation out-diffusion and oxygen in-diffusion [33].

Considering the wear behavior at 500 and 600°C (Fig. 5) with regard to the observed results, the changes can be attributed to both the degree of coating oxidation and the type of formed oxides. Extensive oxidation deep into the coating for 35.1 at.% B is assumed to be the reason for the coating failure at 500°C . A mechanically stable oxide can protect the underlying coating during dry sliding [34]; however, rutile may show only a little protective effect. The large difference in molar volume between rutile ($18.8 \text{ cm}^3/\text{mol}$) and TiN ($11.4 \text{ cm}^3/\text{mol}$) cause the formation of compressive stresses within the oxide layer resulting in oxide spallation if the thickness reaches a critical value [35,36]. During sliding, the stresses in the oxide layer increase and promote destruction. The formation of anatase is assumed to lower the mechanical stability of the oxide layer due to an even higher molar volume ($20.9 \text{ cm}^3/\text{mol}$), and consequently higher compressive stresses in the oxide layer.

4 Conclusions

Ti–N–B coatings were deposited by thermal CVD and the composition was varied from TiN to boron contents up to 35.1 at.%. No phases beside TiN were detected at 0.3 at.% B, whereas the hexagonal TiB_2 phase was identified at 1.1 at.% B with its phase fraction increasing with boron concentration. Boron interrupts the columnar coating growth of TiN, which yields a fine-grained structure with smooth surface at the highest contents. Furthermore, small quantities of boron enhance the hardness substantially, due to both decreasing grain size and increasing amount of TiB_2 . The tribological behavior at 25°C is determined by the influence of boron on hardness and surface structure. High hardness and surface roughness cause high friction in the range of 1.0 up to 13.1 at.% B, while values down to 0.26 were measured for 35.1 at.% B. A lubrication mechanism based on moisture and oxygen is supposed to cause the low friction values, since no comparable values were obtained at higher temperatures. Except for the highest boron content, the friction coefficients are lower at 500 and 600°C due to coating oxidation. The wear rate at 25°C changes with coating hardness and surface roughness and the lowest wear rates were observed for the highest boron concentrations. The wear

behavior at elevated temperatures is different and determined by the oxidation behavior of the coatings. At 500°C, the lowest wear resistance was observed for the highest boron contents, but the wear performance of the high B containing coatings improved substantially at 600°C. While a temperature rise from 500 to 600°C promotes oxidation of TiN, a change in oxidation behavior provokes less oxidation for high boron containing coatings. At 500°C, the oxide composition changes from predominantly rutile for TiN to anatase-dominated as the boron content increases, whereas the oxide layers consist mainly of the thermodynamically stable rutile at 600°C. Additionally, higher temperatures may also favor denser oxide scales by formation of B₂O₃. The formation of rutile in favor of anatase may retard the oxidation process and increases the mechanical properties of the oxide layer resulting in reduced coating wear at elevated temperatures.

Acknowledgments

Financial support by the Austrian Kplus Competence Center Programme is gratefully acknowledged. The authors are grateful to K. Gigl for conducting the deposition processes and to J. Thurner for valuable discussions. We also would like to thank Dr. B. Chernev (Research Institute for Electron Microscopy, Graz) for Raman- and GIR-FTIR spectroscopy.

5 References

- 1 C. Subramanian, K.N. Strafford, T.P. Wilks, L.P. Ward, *J. Mater. Proc. Technol.* 56 (1996) 385.
- 2 H. Holleck, *J. Vac. Sci. Technol. A* 4 (1986) 2661.
- 3 H. Nowotny, F. Benesowsky, C. Brukl, O. Schob, *Mh. Chem.* 92 (1961) 403.
- 4 W. Gissler, *Surf. Coat. Technol.* 68-69 (1994) 556.
- 5 C. Mitterer, M. Rauter, P. Rödhammer, *Surf. Coat. Technol.* 41 (1990) 351.
- 6 B. Rother, H. Kappl, *Surf. Coat. Technol.* 96 (1997) 163.
- 7 C. Pfohl, A. Bulak, K.-T. Rie, *Surf. Coat. Technol.* 131 (2000) 141.
- 8 P.H. Mayrhofer, M. Stoiber, C. Mitterer, *Scripta Mat.* 53 (2005) 241.
- 9 M. Stoiber, C. Mitterer, T. Schoeberl, E. Badisch, G. Fontalvo, R. Kullmer, *J. Vac. Sci. Technol. B* 21 (2003) 1084.
- 10 W. Schintlmeister, W. Wallgram, Patent, EP0306077 B1 (1988).
- 11 H. Holzschuh, Patent, EP1365045 (2003).
- 12 J.-L. Peytavy, A. Lebugle, G. Montel, *High Temp. High Press.* 10 (1978) 341.
- 13 J.-L. Peytavy, A. Lebugle, G. Montel, *Wear* 52 (1979) 89.
- 14 H. Holzschuh, *Int. J. Refract. Met. Hard Mater.* 20 (2002) 143.

- 15 H. Holzschuh, *Thin Solid Films* 469-470 (2004) 92.
- 16 H. Holzschuh, *Proc. 16th Int. Plansee Seminar, Plansee, Reutte, 2005, Vol. 2, p. 801.*
- 17 D.T. Quinto, *Int. J. Refract. Met. Hard Mater.* 14 (1996) 7.
- 18 H. Gräfen (Ed.), 'Lexicon of Materials Technology', VDI Verlag, Düsseldorf, 1991, p. 109.
- 19 J. Vleugels and O. Van Der Biest, *Wear* 225-229 (1999) 285.
- 20 W. Schintlmeister, W. Wallgram, J. Kanz, K. Gigl, *Wear* 100 (1984) 153.
- 21 Th.H. De Keijser, J.I. Langford, E.J. Mittemeijer, A.B.P. Vogels, *J. Appl. Crystallogr.* 15 (1982) 308.
- 22 C. Heermant, D. Dengl, *Materialprüfung* 38 (1996) 374.
- 23 C. Rebholz, A. Leyland, P. Larour, C. Charitidis, S. Logothetidis, A. Matthews, *Surf. Coat. Technol.* 116-119 (1999) 648.
- 24 B.D. Cullity, 'Elements of X-ray Diffraction', Addison-Wesley, Reading Massachusetts, 1978.
- 25 R. Wiedemann, T. Schulz-Kroenert, H. Oettel, *Prakt. Metallogr.* 34 (1997) 498.
- 26 A. Erdemir in: 'Modern Tribology Handbook, Vol. 2', (ed. B. Bhushan), CRC Press, Boca Raton, 2001, p. 787.
- 27 E. Badisch, C. Mitterer, P.H. Mayrhofer, G. Mori, R.J. Bakker, J. Brenner, H. Störi, *Thin Solid Films* 460 (2004) 125.
- 28 K. Holmberg, A. Matthews: 'Coatings Tribology, Properties, Techniques and Applications in Surface Engineering', Elsevier, Amsterdam, 1994..
- 29 C. Mitterer, F. Holler, F. Üstel, D. Heim, *Surf. Coat. Technol.* 125 (2000) 233.
- 30 R.J. Capwell, F. Spagnolo, M.A. DeSesa, *Appl. Spectr.* 26 (1972) 537.
- 31 J. Wagner, C. Mitterer, M. Penoy, C. Michotte, W. Wallgram, M. Kathrein, in *Proc. 16th Int. Plansee Seminar, Plansee, Reutte, 2005, Vol. 2, 917.*
- 32 R.F. Voitovich, É.A. Pugach, *Sov. Powd. Metall. Met. Ceram.* 14 (1975) 132.
- 33 L.A. Donohue, I.J. Smith, W.-D. Münz, I. Petrov, J.E. Green, *Surf. Coat. Technol.* 94-95 (1997) 226.
- 34 K. Kutschej, P.H. Mayrhofer, M. Kathrein, P. Polcik, R. Tessedri, C. Mitterer, *Surf. Coat. Technol.* 200 (2005) 2358.
- 35 D. McIntyre, J.E. Greene, G. Håkansson, J.-E. Sundgren, W.-D. Münz, *J. Appl. Phys.* 67 (1990) 1542.
- 36 J. Desmaison, P. Lefort M. Billy, *Oxid. Met.* 13 (1979) 505.

Publication IV

Deposition of Ti–Al–N coatings by thermal CVD

J. Wagner, V. Edlmayr, M. Penoy, C. Michotte, C. Mitterer, M. Kathrein

**submitted to
Surface & Coatings Technology**

Deposition of Ti–Al–N coatings by thermal CVD

J. Wagner^a, V. Edlmayr^a, M. Penoy^b, C. Michotte^b, C. Mitterer^c, M. Kathrein^d

^{a)} Materials Center Leoben Forschung GmbH, Franz-Josef-Strasse 13, A-8700 Leoben, Austria

^{b)} CERATIZIT Luxembourg S.à.r.l., L-8201 Mamer, Luxembourg

^{c)} Department of Physical Metallurgy and Materials Testing, University of Leoben,
Franz-Josef-Strasse 18, A-8700 Leoben, Austria

^{d)} CERATIZIT Austria GmbH, A-6600 Reutte, Austria

Abstract

This study investigates the feasibility to deposit metastable $Ti_{1-x}Al_xN$ coatings by thermal chemical vapor deposition (CVD) from the $TiCl_4 - AlCl_3 - NH_3 - Ar$ system in an industrial CVD unit. The chemical composition and phase constitution was altered using different $AlCl_3$ contents and deposition temperatures. According to X-ray diffraction (XRD) analysis, single-phase face-centered cubic structures have been obtained up to 19 at.% Al in the coatings, where the incorporation of Al decreases grain size and hardness. In addition, face-centered cubic AlN has been detected between 20 and 24 at.% Al resulting in an enhanced hardness and extremely fine structures. High temperatures and Al contents produce coatings of poor mechanical properties consisting of TiN and hexagonal close-packed AlN.

Keywords: Ti–Al–N; CVD; Structure; Hardness; Aluminum nitride

1 Introduction

The deposition of $Ti_{1-x}Al_xN$ ($0 \leq x \leq 1$) coatings by plasma-assisted chemical vapor deposition (CVD) [1] and physical vapor deposition (PVD) [2] techniques is well-established in cutting tool industry. High coating hardness and oxidation resistance enable the application in severe machining processes like high-speed and dry cutting [3]. The excellent properties result from the substitution of Ti by Al atoms in the face-centered cubic (*fcc*) TiN lattice. The Al incorporation improves both mechanical properties and thermal stability of TiN coatings [4]. Although the mutual solubility of *fcc*-TiN and hexagonal close-packed (*hcp*) AlN is negligible in thermodynamic equilibrium, the non-equilibrium nature of plasma-assisted processes causes an extended solubility and the formation of metastable phases [15]. From the resulting supersaturated phases, *fcc*- $Ti_{1-x}Al_xN$ ($x < 0.6 - 0.7$) is ideal for cutting applications, while the presence of *hcp*- $Al_xTi_{1-x}N$ is widely accepted to deteriorate the performance [6].

The preparation of TiN coatings for wear resistant applications by thermal CVD is a conventional process since many years [7]. However, the incorporation of Al and

formation of $fcc\text{-Ti}_{1-x}\text{Al}_x\text{N}$ coatings without plasma assistance is challenging [8]. Single-phase $fcc\text{-Ti}_{1-x}\text{Al}_x\text{N}$ ($x < 0.57$) coatings have been obtained by thermal CVD using metal-organic precursors [9,10]. The disadvantages of metal-organic precursors are their high costs, and the low deposition temperatures may cause an insufficient adhesion. Most frequently used in cutting tool industry are the less expensive metal chlorides, e.g. TiCl_4 together with N_2 and H_2 is a customary precursor system for the deposition of TiN. However, the incorporation of Al into TiN using AlCl_3 , N_2 , and H_2 is thermodynamically not feasible. The utilization of NH_3 as nitrogen source and reducing agent instead of N_2 and H_2 enables the formation of both TiN and AlN within a comparable temperature range [8]. Most studies consider the deposition of either single-phase coatings of $fcc\text{-TiN}$ [11] and $hcp\text{-AlN}$ [12], respectively, or $fcc\text{-TiN}/hcp\text{-AlN}$ composites [13], but only few investigations report on $fcc\text{-Ti}_{1-x}\text{Al}_x\text{N}$ deposits. Metastable fcc coatings have been deposited using the metallic halides TiCl_3 and AlCl_3 from in-situ chlorination of TiAl-alloys together with NH_3 [14,15]. The chlorination process with Cl_2 at 800°C requires sophisticated equipment and chlorination of alloys bears the risk of preferred evaporation of a constituent. Recently, $fcc\text{-Ti}_{1-x}\text{Al}_x\text{N}$ ($x < 0.9$) coatings have been deposited from the metal halide precursors TiCl_4 and AlCl_3 together with NH_3 and H_2 in a laboratory scale unit [16].

Here, we explore the feasibility to deposit Ti–Al–N coatings by thermal CVD, in particular $fcc\text{-Ti}_{1-x}\text{Al}_x\text{N}$, using the conventional metal halide precursors TiCl_4 and AlCl_3 together with NH_3 in an industrial deposition plant. The Ti–Al–N coatings have been grown at different deposition temperatures and AlCl_3 contents in the gas phase. The coatings have been characterized with respect to composition, structure, morphology, and mechanical properties.

2 Experimental

The deposition experiments were performed in an industrial hot-wall CVD system at atmospheric pressure [17] using TiCl_4 , AlCl_3 , NH_3 , and Ar. AlCl_3 was generated by the reaction between HCl and Al chips, while liquid TiCl_4 was evaporated in an Ar carrier gas flow. At a substrate temperature of 550°C , the AlCl_3 partial pressures $p(\text{AlCl}_3)$ was varied between 0 and 246 Pa, while the other parameters were kept constant. The experiments between 600 and 700°C were performed with half the concentration of reactive gases (i.e., AlCl_3 , TiCl_4 , and NH_3) for an improved growth rate homogeneity. Thus, $p(\text{AlCl}_3)$ was altered between 0 and 123 Pa at 600°C . For the depositions at 650°C and 700°C , $p(\text{AlCl}_3)$ was set to 62 Pa.

Coating deposition was performed on cemented carbide substrates (77 wt.% WC, 11 wt.% Co, 4 wt.% TiC, 8 wt.% (Ta,Nb)C). The mean chemical composition of the coatings was measured from glow discharge optical emission spectroscopy (GDOES) depth-profiles (Jobin-Yvon Horiba JY10000RF). Glancing-angle X-ray diffraction

(GAXRD) analysis was applied to determine the crystallographic structure using Cu $K\alpha$ radiation at an incident angle of 2° (Panalytical X'Pert Pro). The coating structure was studied on fracture cross-sections by scanning electron microscopy (SEM) using a Zeiss evo50. Microhardness measurements were carried out on polished samples with a computer-controlled microhardness tester (Fischerscope H100C) using a Vickers indenter with BK7 tip shape correction [18].

3 Results

The influence of the AlCl_3 partial pressure $p(\text{AlCl}_3)$ on the coating composition is shown in Fig. 1a and b for deposition temperatures T_{dep} of 550 and 600°C, respectively. From 550 to 600°C, the concentration of reactive gases, i.e. AlCl_3 , TiCl_4 , and NH_3 was reduced to improve the growth rate uniformity, but the ratio between the gases was kept constant. At 550°C, the Al content increases with $p(\text{AlCl}_3)$ from TiN (i.e. without Al) up to 13 at.% Al. Associated with Al, the Cl concentration rises from 3 to 7 at.%. Besides Cl, relatively high O impurities have been observed in the coatings. The Al content increases at T_{dep} of 600°C more intensely with $p(\text{AlCl}_3)$ (see Fig. 1b), but less steadily compared to 550°C and the highest Al content can be observed at the lowest concentration of AlCl_3 . Regarding the impurities, the Cl concentration increases with $p(\text{AlCl}_3)$ up to 6 at.%, while the O incorporation decreases.

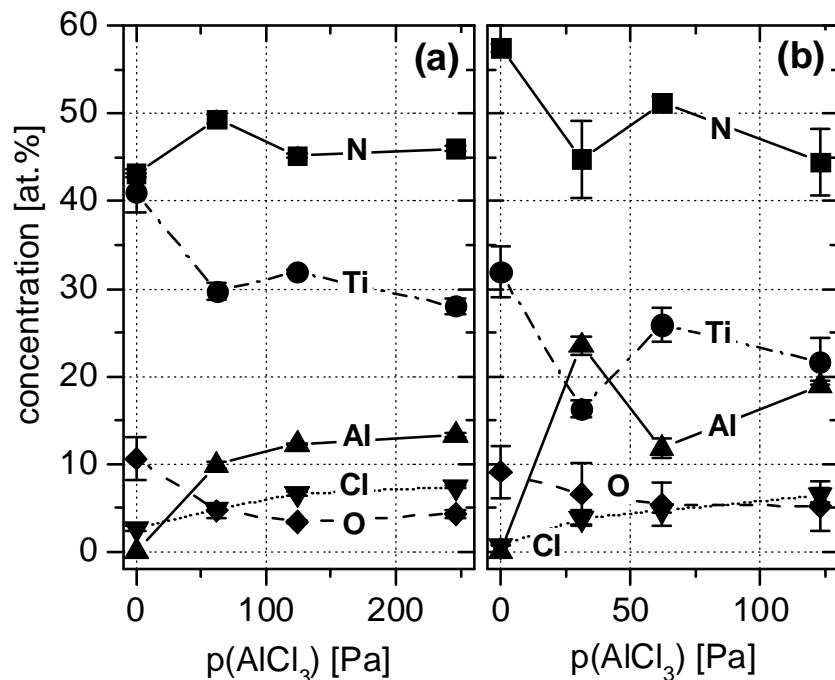


Fig. 1: Coating composition in dependence on the AlCl_3 partial pressure $p(\text{AlCl}_3)$ for deposition temperatures of (a) 550°C and (b) 600°C.

The temperature influence was examined between 600 and 700°C using a constant $p(\text{AlCl}_3)$ of 62 Pa. As T_{dep} rises from 600 to 650 and 700°C, the Al content increases

from 20 to 29 and finally 36 at.% Al. Simultaneously, the Cl and O concentration decreases from 7 to 3 at.% and 7 to 4 at.%, respectively.

GAXRD patterns of six representative Ti–Al–N coatings within the investigated range (0 – 36 at.% Al) are exhibited in Fig. 2. The TiN coating ($T_{dep} = 550^\circ\text{C}$) shows a preferred (100) orientation at $2\theta = 42.93^\circ$ and a considerably lower lattice parameter $a = 0.4210$ nm compared to stoichiometric bulk material ($a_0 = 0.4240$ nm). For 13 at.% Al ($T_{dep} = 550^\circ\text{C}$) and 19 at.% Al ($T_{dep} = 600^\circ\text{C}$), no additional phases can be detected and we refer to these coatings as $fcc\text{-Ti}_{1-x}\text{Al}_x\text{N}$. A slightly higher Al content of 20 at.% ($T_{dep} = 600^\circ\text{C}$) results in the formation of $fcc\text{-AlN}$ beside $fcc\text{-Ti}_{1-x}\text{Al}_x\text{N}$. Additionally, at 24 at.% Al the first signs of the $hcp\text{-AlN}$ phase can be observed. Higher deposition temperatures and Al contents, respectively, cause predominantly the formation of $hcp\text{-AlN}$ in favor of $fcc\text{-Ti}_{1-x}\text{Al}_x\text{N}$ and $fcc\text{-AlN}$ as can be seen for 36 at.% Al ($T_{dep} = 700^\circ\text{C}$) in Fig. 2. The (100) orientation of the fcc phase remains with increasing Al incorporation, where the peaks show substantial peak broadening. The peak position of the $fcc\text{-Ti}_{1-x}\text{Al}_x\text{N}$ phase approaches the standard value of TiN as the Al content increases.

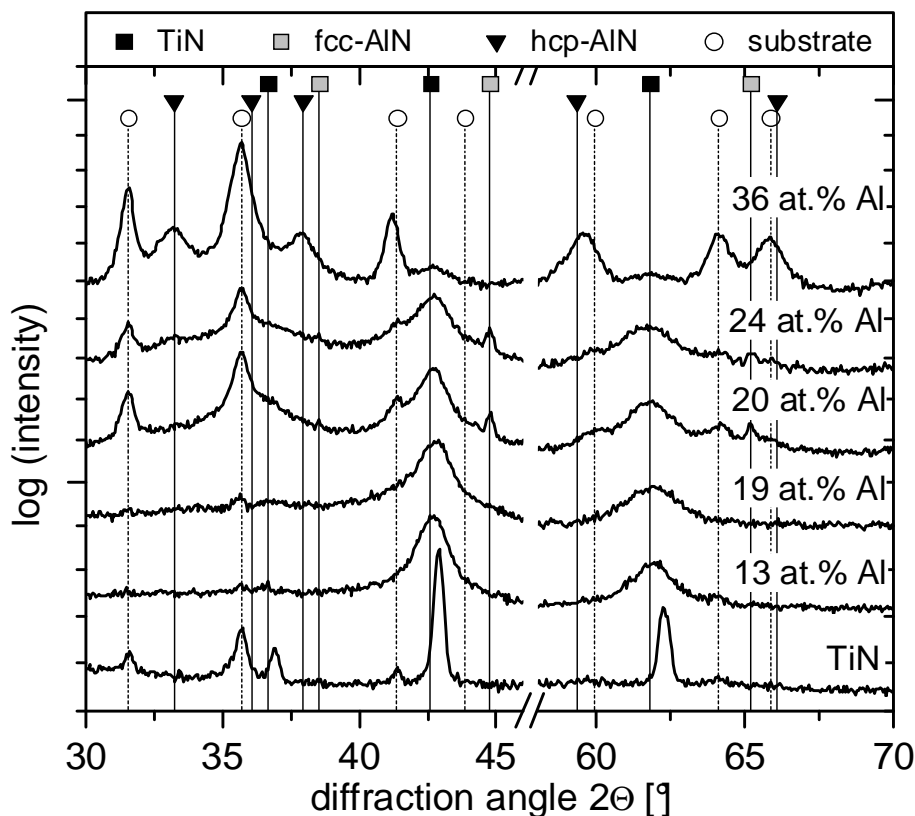


Fig. 2: GAXRD patterns of Ti–Al–N coatings with different Al contents on cemented carbide substrates.

SEM micrographs of fracture cross-sections are shown in Fig. 3 for different Al contents. The coating structure changes from columnar for Al contents of up to 13 at.% (Fig. 3a) to a dense, featureless glassy morphology for 24 at.% Al (Fig. 3b) and to granular, crumbly for 36 at.% Al (Fig. 3c).

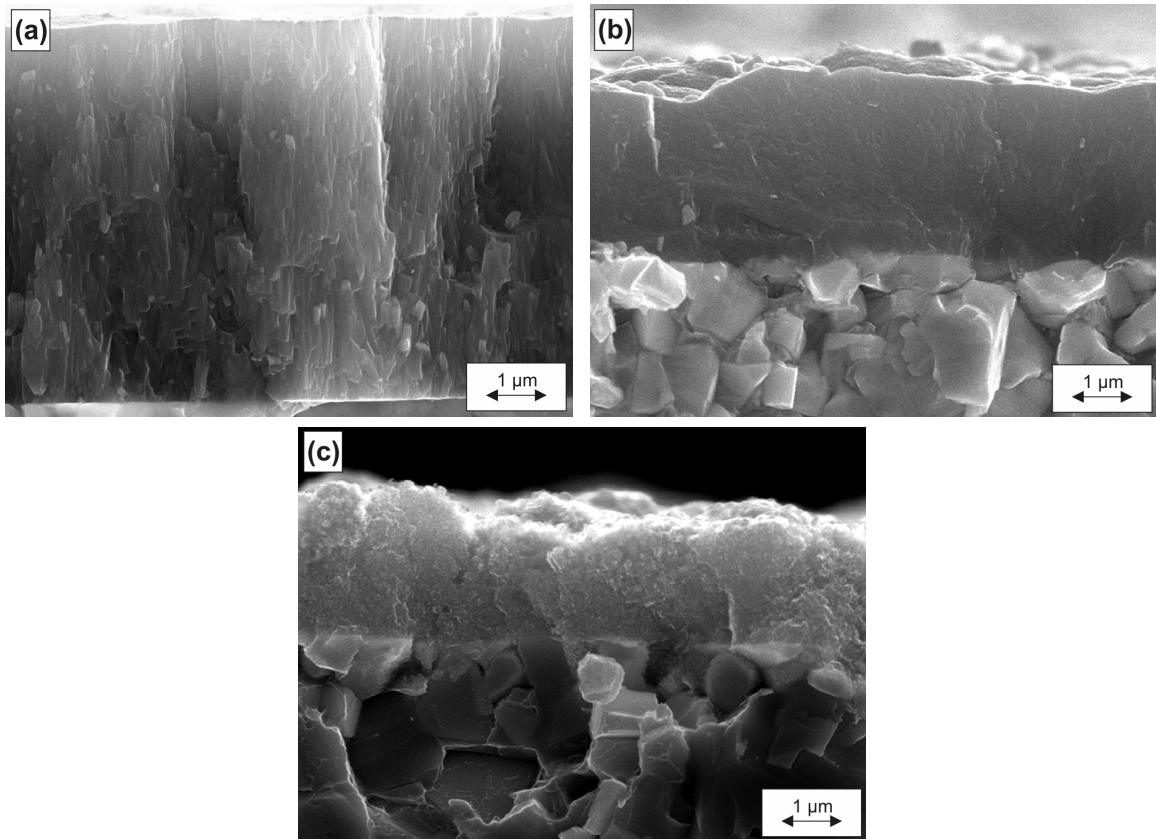


Fig. 3: SEM fracture cross-sections of Ti-Al-N coatings containing (a) 13 at.%, (b) 24 at.% and, (c) 36 at.% Al on cemented carbide substrates.

The hardness HU_{pl} was determined on polished samples to minimize roughness effects. The dependency on the Al content is shown in Fig. 4. The coatings are distinguished according to the phases detected by GAXRD.

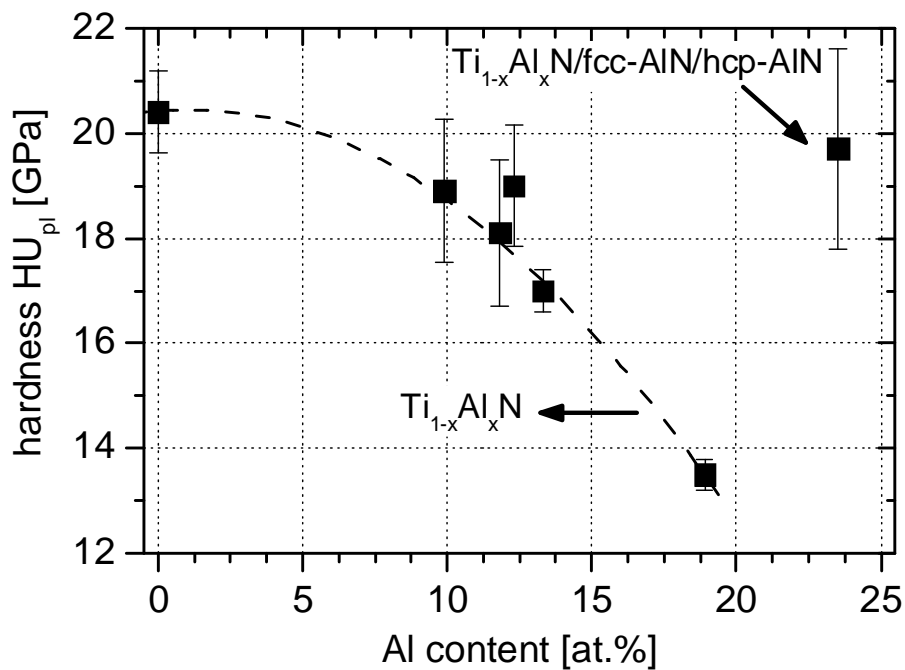


Fig. 4: Influence of Al content on coating hardness HU_{pl} .

HU_{pl} gradually decreases from 20 GPa for TiN to 13 GPa as the Al concentration increases to 19 at.% Al. A higher content of 24 at.% consequences an enhanced hardness of 20 GPa. Hardness values for higher Al concentrations could not be obtained since these coatings failed during the polishing process.

4 Discussion

The $AlCl_3$ partial pressure and, in particular, the deposition temperature have shown to remarkably influence the coating composition (Fig. 1), where both high temperatures and $p(AlCl_3)$ values raise the Al incorporation. The increasing Cl incorporation with $p(AlCl_3)$ indicates that the Cl results mainly from an incomplete dissociation of the more stable $AlCl_3$ and less from $TiCl_4$. Higher temperatures enhance the reactivity of $AlCl_3$ and consequence higher Al and lower Cl contents in the coatings [1,14]. The relatively high oxygen contents detected may originate from residual oxygen in the deposition system, the high affinity of high Cl-containing coatings to oxidation [19], and an oxygen enrichment at the surface (evidenced by GDOES depth-profiling) indicates oxidation at the end of the deposition process. A decreasing oxygen contamination with increasing Al content can be noticed suggesting the formation of a protective alumina layer.

GAXRD analysis indicates the formation of single-phase $fcc-Ti_{1-x}Al_xN$ coatings up to 19 at.% Al (cf. Fig. 2). The coatings exhibit a preferred (100) orientation frequently found for TiN coatings using $TiCl_4$ and NH_3 [20,21]. Columnar structures can be observed for low Al contents, whereas higher Al incorporation results in grain refinement till glassy or crumbly structures are obtained. The decreasing grain size can be also detected in an enhanced XRD peak broadening. In contrary to PVD and plasma-assisted CVD $fcc-Ti_{1-x}Al_xN$ coatings [1,22], the hardness of single-phase coatings continuously decreases with increasing Al content up to 19 at.% (see Fig. 4). The simultaneously increasing Cl content may lower the hardness of these coatings [1,23]. On the other hand, the low deposition temperatures of 600°C are assumed to promote formation of amorphous phases like $a-AlN$, which can not be excluded from XRD measurements [24]. Both Cl [23] and the formation of $a-AlN$ could contribute to the observed grain refinement. The incorporation of Al into the $fcc-TiN$ lattice can not be demonstrated from the dependency of the lattice parameter on the Al coating concentration. Generally, substitution of Ti by smaller Al atoms in the $fcc-TiN$ structure results in $fcc-Ti_{1-x}Al_xN$ and a gradual decrease of the lattice parameter with increasing Al fraction x [1,15,22]. Here, the opposite trend can be observed and the lattice parameter increases with the Al concentration. Several factors influence the lattice parameter and to elucidate an unambiguous correlation is difficult. The lattice parameter of TiN – ‘starting point’ for the following considerations – is already too low compared to the bulk value, see Fig. 2. From the low thermal expansion coefficient of cemented carbide, residual tensile stresses can be expected to arise in the coatings during cooling, which will

reduce the measured lattice parameter. The observed purple color and the low lattice parameter of the TiN coatings point towards a non-stoichiometric compound TiN_x ($0.5 \leq x \leq 1.16$), particularly an excess of N [25]. The vacancy structure of TiN_x is stable over a wide range and causes lower lattice parameters for both over- and under-stoichiometric coatings [26]. The measured excess of N relative to Ti (Fig. 1) indicates an over-stoichiometric TiN_x ($x > 1$) phase, which exhibits a Ti-vacancy defect structure. The partially unoccupied Ti sites cause shrinkage of the lattice. The low deposition temperatures seem to favor the formation of non-stoichiometric TiN_x . Especially, under-stoichiometric TiN_x has been found in many studies [20,21,27], whereas over-stoichiometric TiN_x has been rarely mentioned [14,28]. The relatively high Cl and O impurity contents and their counteracting behavior will also affect the lattice parameter. Interstitial incorporation of the larger Cl atoms instead of N will result in an expansion of the lattice [29], whereas a substitution by O will shrink the lattice [30]. For the *fcc*- $\text{Ti}_{1-x}\text{Al}_x\text{N}$ coatings grown in this work, it might be possible that the Al atoms take the position of the vacant Ti sites of the TiN_x lattice, and as a result, the lattice parameter increases with Al incorporation.

Between 20 and 24 at.% Al, further phases have been detected beside *fcc*- $\text{Ti}_{1-x}\text{Al}_x\text{N}$. The GAXRD patterns exhibit reflections at the position of *fcc*-AlN for 20 at.% Al. At 24 at.% Al, the first indication of *hcp*-AlN can be observed (see Fig. 2). In the following, these phases are denominated as *fcc*-AlN and *hcp*-AlN, respectively; although, Ti incorporation in these phases can not be excluded. The formation of these additional phases causes fine-grained structures and, compared to single-phase *fcc*- $\text{Ti}_{1-x}\text{Al}_x\text{N}$ coatings, a considerably enhanced coating hardness (see Fig. 4). The metastable *fcc*-AlN phase has been detected during the decomposition process of PVD *fcc*- $\text{Ti}_{1-x}\text{Al}_x\text{N}$ coatings, where the supersaturated solution undergoes spinodal decomposition into coherent *fcc*-TiN and *fcc*-AlN domains in a *fcc*- $\text{Ti}_{1-x}\text{Al}_x\text{N}$ matrix. The system achieves equilibrium by separation of excess atoms into different phases. Finally, the metastable phases *fcc*- $\text{Ti}_{1-x}\text{Al}_x\text{N}$ and *fcc*-AlN transform into the stable phases *fcc*-TiN and *hcp*-AlN as the temperature increases further. The indirect decomposition route involving *fcc*-AlN reduces the energy barrier for *hcp*-AlN nucleation [4,31]. Within this work, a similar process could be responsible for *fcc*-AlN formation. Excessive Al incorporation could destabilize the Ti-rich *fcc*- $\text{Ti}_{1-x}\text{Al}_x\text{N}$ and causes the precipitation of *fcc*-AlN during the deposition process. Surface-initiated spinodal decomposition of $\text{Ti}_{1-x}\text{Al}_x\text{N}$ has already been observed to take place during growth of PVD *fcc*- $\text{Ti}_{1-x}\text{Al}_x\text{N}$, to form a rod-like nanostructure of *fcc*-TiN and *fcc*-AlN domains with a period of 2 – 3 nm [32]. As a result, the Ti concentration in the *fcc*- $\text{Ti}_{1-x}\text{Al}_x\text{N}$ matrix increases, which implies a reduction of the free energy [31]. Phase separation in the opposite way has been noticed in thermal CVD *fcc*- $\text{Ti}_{1-x}\text{Al}_x\text{N}$ coatings studies by Endler et al. [16]. There, an increase of the deposition temperature resulted

in the additional formation of TiN besides high Al containing $fcc\text{-Ti}_{1-x}\text{Al}_x\text{N}$ ($x = 0.8 - 0.9$). It can be expected that the high Al content causes precipitation of TiN within the Al supersaturated matrix. The precipitates reduce the excess Ti concentration and, thus, the free energy of the $fcc\text{-Ti}_{1-x}\text{Al}_x\text{N}$ phase.

Al contents above 24 at.% and higher deposition temperatures, respectively, cause the formation of mainly $hcp\text{-AlN}$ at the expense of the fcc phases. It can be expected that the high temperatures favor the thermodynamically stable phases $hcp\text{-AlN}$ and $fcc\text{-TiN}$. Also, the XRD reflections of TiN approach the standard position with increasing temperature, see Fig. 2. The formation of $hcp\text{-AlN}$ is not advantageous for the coating properties, i.e. the coating structure coarsens as the hcp phase increases (cf. Figs. 3b and c) and the low hardness of $hcp\text{-AlN}$ deteriorates the mechanical performance (cf. Fig. 4).

5 Conclusions

Ti–Al–N coatings were deposited at temperatures between 550 and 700°C in an industrial thermal CVD system using the customary precursors TiCl_4 , AlCl_3 , and NH_3 . The Al content increased with the AlCl_3 concentration and especially the deposition temperature. High temperatures enhance the complete dissociation of the metal chlorides, in particular of AlCl_3 and raise the Al content in the coatings, while the incorporated Cl is reduced. The results obtained from XRD measurements give scope for presumptions about the coating constitution. Only one fcc phase has been detected up to 19 at.% Al. From the decreasing hardness and the rising lattice parameter with Al incorporation, formation of a single-phase supersaturated $fcc\text{-Ti}_{1-x}\text{Al}_x\text{N}$ structure can not be unambiguously concluded, particularly, since possible amorphous phases like $a\text{-AlN}$ are not gathered by XRD analysis. However, metastable $fcc\text{-AlN}$ has been detected at 20 at.% and the first evidences of stable $hcp\text{-AlN}$ at 24 at.% Al. The appearance of $fcc\text{-AlN}$ in the XRD patterns is an indication for $fcc\text{-Ti}_{1-x}\text{Al}_x\text{N}$ formation below 20 at.% Al and could result from the spinodal decomposition process of the supersaturated

$fcc\text{-Ti}_{1-x}\text{Al}_x\text{N}$. Al also changes the coating structure from columnar to very fine grained or even feature-less as the concentration increases. While in general coatings show hardness values decreasing with increasing Al (and Cl and O impurity) content, the coating with 24 at.% Al yielded a relatively high hardness of 20 GPa. High deposition temperatures and Al concentrations up to 36 at.%, respectively, initiate predominantly the formation of $hcp\text{-AlN}$ and TiN. The coatings yield a crumbly morphology and unfavorable mechanical properties.

This study reveals the feasibility to deposit Ti–Al–N coatings by thermal CVD in a commercial deposition unit. The results provide a suitable basis for further developments with regard to commercial Ti–Al–N coated cutting tools.

Acknowledgments

Financial support by the Austrian Kplus Competence Center Programme is gratefully acknowledged. The authors are grateful to K. Gigl for conducting the deposition processes and to G. Hawranek for the SEM investigations. Special thanks are due to Dr. P.H. Mayrhofer for valuable discussions.

References

- 1 K.H. Kim, S.J. Lee, *Thin Solid Films* 283 (1996) 165.
- 2 O. Knotek, W.-D. Münz, T. Leyendecker, *J. Vac. Sci. Technol. A* 5 (1987) 2173.
- 3 D. Münz, *J. Vac. Sci. Technol. A* 4 (1986) 2717.
- 4 P.H. Mayrhofer, A. Hörling, L. Karlsson, J. Sjöén, T. Larsson, C. Mitterer, L. Hultman, *Appl. Phys. Lett.* 83 (2003) 2049.
- 5 H. Holleck, *Surf. Coat. Technol.* 36 (1988) 151.
- 6 A. Hörling, L. Hultman, M. Odén, J. Sjöén, L. Karlsson, *Surf. Coat. Technol.* 191 (2005) 384.
- 7 H.E. Rebenne, D.G. Bhat, *Surf. Coat. Technol.* 63 (1994) 1.
- 8 N. Yoshikawa, *Recent Res. Devel. Mat. Sci.* 3 (2002) 17.
- 9 S. Gilles, N. Bourhila, S. Ikeda, C. Bernard, R. Madar, *Surf. Coat. Technol.* 94-95 (1997) 285.
- 10 S. Ikeda, S. Gilles, B. Chenevier, *Thin Solid Films* 315 (1998) 257.
- 11 S.R. Kurtz, R.G. Gordon, *Thin Solid Films* 140 (1986) 277.
- 12 H.J. Kim, Y. Egashira, H. Komiyama, *J. Chem. Vap. Dep.* 1 (1992) 20.
- 13 N. Yoshikawa, M. Aoki, A. Kikuchi, S. Taniguchi, *Int. J. Mater. Prod. Technol.* 16 (2001) 109.
- 14 S. Anderbouhr, E. Blanquet, V. Ghetta, C. Bernard, *Electroch. Soc. Proc. of the 14th Conf. EUROCVI XI* 25 (1997) 356.
- 15 S. Anderbouhr, V. Ghetta, E. Blanquet, C. Chabrol, F. Schuster, C. Bernard, R. Madar, *Surf. Coat. Technol.* 115 (1999) 103.
- 16 I. Endler, M. Herrmann, M. Naupert, R. Pitonak, S. Ruppi, M. Schneider, H. van den Berg, H. Westphal, *Proc. Euro PM2006* (2006) 219.
- 17 W. Schintlmeister, W. Wallgram, J. Kanz, K. Gigl, *Wear* 100 (1984) 153.
- 18 C. Heermant, D. Dengl, *Materialprüfung* 38 (1996) 374.
- 19 T. Aizawa, T. Akhadejdamrong, A. Mitsuo, *Surf. Coat. Technol.* 177-178 (2004) 573.
- 20 H.H. Huang, M.H. Hon, *Thin Solid Films* 416 (2002) 54.

- 21 N. Ramanuja, R.A. Levy, S.N. Dharmadhikari, E. Ramos, C.W. Pearce, S.C. Menasian, P.C. Schamberger, C.C. Collins, *Mater. Lett.* 57 (2002) 261.
- 22 S. PalDey, S.C. Deevi, *Mater. Sci. Eng. A342* (2003) 58.
- 23 K.-T. Rie, A. Gebauer, J. Woehle, *Surf. Coat. Technol.* 60 (1993) 385.
- 24 Y.J. Liu, H.J. Kim, Y. Egashira, H. Kimura, H. Komiyama, *J. Am. Ceram. Soc.* 79 (1996) 1335.
- 25 A. Kato, N. Tamari, *J. Cryst. Growth* 29 (1975) 55.
- 26 J.-E. Sundgren, *Thin Solid Films* 128 (1985) 21.
- 27 C.-C. Jiang, T. Goto, T. Hirai, *J. Alloys Comp.* 190 (1993) 197.
- 28 J.T. Hillman, D.W. Studiner, M.J. Rice Jr., C. Arena, *Microelectr. Eng.* 19 (1992) 375.
- 29 K.-T. Rie, A. Gebauer, J. Wöhle, *Surf. Coat. Technol.* 86-87 (1996) 498.
- 30 N. Martin, O. Banakh, A.M.E. Santo, S. Springer, R. Sanjinés, J. Takadoum, F. Lévy, *Appl. Surf. Sci.* 185 (2001) 123.
- 31 P.H. Mayrhofer, C. Mitterer, L. Hultman, H. Clemens, *Prog. Mat. Sci.* 51 (2006) 1032.
- 32 F. Adibi, I. Petrov, L. Hultman, U. Wahlström, T. Shimizu, D. McIntyre, J.E. Greene, J.-E. Sundgren, *J. Appl. Phys.* 69 (1991) 6437.